THE DESIGN AND SIMULATION OF A CHEMICAL LOOPING COMBUSTION SYSTEM

BY

Haixia Li

A Thesis Presented to the
DEANSHIP OF GRADUATE STUDIES

KING FAHD UNIVERSITY OF PETROLEUM & MINERALS

DHAHRAN, SAUDI ARABIA

In Partial Fulfillment of the
Requirements for the Degree of

MASTER OF SCIENCE

In

MECHANICAL ENGINEERING

April, 2017

KING FAHD UNIVERSITY OF PETROLEUM & MINERALS

DHAHRAN- 31261, SAUDI ARABIA

DEANSHIP OF GRADUATE STUDIES

This thesis, written by **Haixia Li** under the direction his thesis advisor and approved by his thesis committee, has been presented and accepted by the Dean of Graduate Studies, in partial fulfillment of the requirements for the degree of **MASTER OF SCIENCE IN MECHANICAL ENGINEERING**.

Dr. Zuhair Mattoug Gasem
Department Chairman

Dr. Salam A. Zummo
Dean of Graduate Studies

10/5/17
Date

R. B. Mansour
Dr. Ben-Mansour, Rached
(Advisor)

Med Habib
Dr. Habib, Mohamed A.
(Member)

Mozahar Hossain
Dr. Mohammead Mozahar
Hossain
(Member)

To my beloved family

ACKNOWLEDGMENTS

None of the results presented in this report would exist without the kind help from my respectful advisor Dr. Rached Ben-Mansour and my committee members Dr. Mohamed A. Habib and Dr. Mohammead Mozahar Hossain. I would like to give my sincere thanks to my advisor for taking me as one of his students and introduced this interesting topic to me as my master thesis project. It is the kind help, patience and encouragement from my advisor and committee members supported me to finish my work.

Meanwhile, countless help I received from my dear friends also supported me during all the processes. They helped me to overcome the obstacles from my academic study and my daily life. It is impossible to express my gratitude to them.

It is the scholarship provided by KFUPM that supports me to finish my study and research. I would like to express my gratitude to the communities and institutions of KFUPM. Not only academically but also spiritually, I was supported by many faculties and staffs in KFUPM.

Last but not least, I would like to thank my beloved family who always support me at any time.

TABLE OF CONTENTS

LIST OF TABLES

LIST OF FIGURES

LIST OF ABBREVIATIONS

GHG	greenhouse gas
CLC	chemical looping combustion
CCS	carbon capture and storage
FR	fuel reactor
AR	air reactor
OC	oxygen carrier
MFV	minimum fluidization velocity
SFV	superficial feeding velocity
SCM	shrinking core model
NNGM	nucleation and nuclei growth model
I.I.	initial inventory
BCs	boundary conditions
C_D	dragging function
$D_{i,mix}$	the coefficient of diffusion of the mixture
D_{turb}	turbulent diffusivity
e_{ss}	the restitution coefficient for particle collision
F_q	the external body force of q phase
F_{lift}	lift force
$F_{wl,q}$	wall lubrication force
F_{vm}	virtual mass force
F_{td}	turbulent dispersion force
g_0	radial distribution function

g	gravitational acceleration
K_{gs}	interphase momentum exchange coefficient
$\dot{m}_{pq}$	mass transfer from phase p to phase q
$\dot{m}_{qp}$	mass transfer from phase q to phase p
P	pressure
R_{pq}	interphase force between phases
S	source term
t_r	particulate relaxation time
v	velocity
v'	fluctuation velocity

Greek symbols

α	volume fraction
σ_a	absorption coefficient
σ_s	scattering coefficient
τ_q	stress-strain tensor of phase q
μ_q	the viscosity of phase q
λ_q	the bulk viscosity of phase q
μ_{col}	collisional shear viscosity
μ_{fr}	frictional viscosity
$\mu_{kinetic}$	kinetic viscosity
μ_t	turbulent viscosity
Θ_g	granular temperature
ρ	density

Subscripts

p, q	phases
g	gas phase
s	solid phase
λ	wave length

ABSTRACT

Full Name : Haixia Li
Thesis Title : The Design and Simulation of a Chemical Looping Combustion System
Major Field : Mechanical engineering
Date of Degree : April 2017

Global warming and climate change have now become worldwide major concerns. The temperature on the surface of our planet keeps increasing due to the enormous emission of greenhouse gases (GHG) by human activity. Climate system is now considered reaching its tipping point which may cause significant, catastrophic and irreversible damages to the entire ecosystem. Reduction of emission of greenhouse gases has become an important research subject and an international political issue. After its concept was put forward, chemical looping combustion (CLC) technology is studied worldwide by researchers due to its intrinsic characteristic of producing exhaust gases with high purity carbon dioxide (CO_2). Oxygen carrier (OC) particles are introduced as an intermediate material in CLC systems. Reduced form OC firstly reacts with oxygen in the air within air reactor (AR) and produces oxidized form OC. Oxidized form OC then is transported into fuel reactor (FR) and reacts with gaseous, liquid or solid forms fuel to produce reduced form OC. In such way, conventional combustion processes are split into two chemical reactions. CLC technology is considered as a promising technology in CO_2 separation with lower energy consumption since no nitrogen is fed into the fuel reactor.

The present work provides the mathematical modeling and implementation of numerical simulations of typical CLC systems (FR & AR) using the commercial CFD codes. Chemical reaction kinetics are validated against both experimental and numerical published data. Basic flow patterns and conversion performances of OC within FR and AR with different OC size, various gas distributors, different operating temperatures and different superficial feeding velocity are investigated. The effects of radiation on flow and conversion performances are also tested under different operating parameters.

Numerical results by the present study indicate that in both AR and FR coefficients between superficial feeding velocity of gas phase and minimum feeding velocity significantly determine the flow patterns. Gas distributors (regulators) on inlet change bubble distributions within reactors. Bubble distributions within FR are more uniform with Rec-Tri (rectangle-triangle) fuel feeding distributor on FR inlet. Radiative heat transfer has insignificant effects on flow patterns and temperature distributions on dense regions. However, temperature gradients and heat loos on sparse regions are higher with radiation heat transfer consider. As a fast bed, inventory of OC within air reactor tend to fluctuate around a fixed value after the initial stage. The conversion performances of fuel within FR and OC within AR are related to many parameters including material of OC, type of fuel, inventory of OC, superficial feeding velocity of the gas phase, operating temperature, distributors and radiative heat transfer, etc. The most significant parameters that affect conversion performances are OC material and operating temperature.

ملخص الرسالة

الاسم الكامل: لي هايشيا

عنوان الرسالة: تصميم ومحاكاة نظام حلقات الاحتراق الكيميائية

التخصص: هندسه ميكانيكيه (علوم حراريه)

تاريخ الدرجة العلمية: رجب ١٤٣٨

أصبحت ظاهرة الاحتباس الحراري وتغير المناخ الآن الشواغل الرئيسية في جميع أنحاء العالم. إن درجة الحرارة على سطح كوكبنا تتزايد بسبب الانبعاث الهائل لغازات الدفيئة (الغازات المسببه للاحتباس الحراري) بسبب النشاط البشري. ويعتبر النظام المناخي الآن نقطة تحول التي قد تسبب أضرارا كبيرة، كارثية ولا رجعة فيها للنظام البيئي بأكمله. وقد أصبح الحد من انبعاث الغازات الدفيئة موضوعا بحثيا هاما وقضية سياسية دولية. بعد طرح مفهومه، يدرس الباحثون تقنية الاحتراق الكيميائي (CLC) في جميع أنحاء العالم بسبب سماته الجوهرية لإنتاج غازات العادم ذات ثاني أكسيد الكربون (CO_2)عالي النقاء. يتم إدخال الجسيمات الناقله للأكسجين كمواد وسيطة في أنظمة الاحتراق الكيميائي. الشكل المخفض (OC) يتفاعل أولا مع الأوكسجين في الهواء داخل مفاعل الهواء وتنتج أوكسيديزد شكل (OC). الشكل المؤكسد (OC) يتم نقله إلى مفاعل الوقود (FR) ويتفاعل مع الحاله الغازية، السائله أو الصلبة للوقود لإنتاج الشكل المخفض من OC. وبهذه الطريقة، تنقسم عمليات الاحتراق التقليدية إلى تفاعلين كيميائيين. وتعتبر تكنولوجيا الاحتراق الكيميائي (CLC) تكنولوجيا واعدة في فصل ثاني أكسيد الكربون مع انخفاض استهلاك الطاقة حيث لا يتم تغذية النيتروجين في مفاعل الوقود.

العمل الحالي يوفر النمذجة الرياضية وتنفيذ المحاكاة العددية لأنظمة الاحتراق الكيميائي النموذجية (AR & FR) باستخدام ديناميكا السوائل الحسابيه CFD. يتم التحقق من حركية التفاعل الكيميائي في كل من البيانات (الآوراق البحثيه ذات الصله) المنشورة التجريبية والحسابيه. يتم فحص أنماط التدفق الأساسية وأداء تحويل ناقل الأكسجين داخل مفاعل الوقود و مفاعل الهواء مع أخذ أحجام مختلفه لناقل الآكسجين، مع أخذ موزعات الغاز المختلفة، عند درجات حرارة التشغيل المختلفة وسرعات التغذية السطحية المختلفة. كما يتم اختبار آثار الإشعاع على أداء التدفق والتحويل في إطار بارامترات تشغيل مختلفة.

النتائج العددية (الحسابيه) من خلال الدراسة الحالية تشير إلى أن كلا" من معاملات مفاعل الهواء ومفاعل الوقود بين سرعة التغذية السطحية من الطور الغازي والحد الأدنى من سرعة التغذية تحدد بشكل كبير أنماط التدفق. موزعات الغازتعتبر هي المنظمات المسئوله عن توزيع الفقاعات داخل المفاعلات. توزع الفقاعات داخل مفاعل الوقود هي أكثر اتساقا مع Rec-Tri (المستطيل - مثلث) من تغذية الوقود الموزع على مدخل مفاعل الوقود. انتقال الحرارة بالاشعاع له آثار ضئيلة على أنماط التدفق وتوزعات درجات الحرارة على المناطق الكثيفة. ومع ذلك، يلاحظ بان تدرجات درجة الحرارة والحرارة المفقوده على المناطق المتفرقه للمفاعلات هي أعلى من انتقال الحرارة بالإشعاع. وبصفتها سريعا ، يميل كل الاكسجين المنقول داخل مفاعل الهواء إلى التقلب حول قيمة ثابتة بعد المرحلة الأولية. يرتبط أداء تحويل الوقود داخل مفاعل الوقود والآكسجين المنقول داخل مفاعل الهواء بالعديد من البارامترات بما في ذلك مواد ناقل الآكسجين ونوع الوقود ومخزون ناقل الآكسجين وسرعة التغذية السطحية لمرحلة الغاز ودرجة حرارة التشغيل والموزعات واننقال الحرارة بالاشعاع، وما إلى ذلك. وأهم البارامترات التي تؤثر على أداء التحويل هي مواد ناقل الاكسجين (OC) ودرجة حرارة التشغيل.

CHAPTER 1

INTRODUCTION

Greenhouse gases (GHG) which include carbon dioxide (CO_2), water vapor (H_2O), methane (CH_4) etc. has been an important factor for the climate system. Via the well-known “greenhouse effect”, greenhouse gases act as a blanket on the atmosphere and keep the Earth warm. Without the greenhouse effect of GHG, the average temperature on the Earth surface will drop to -21℃ [1]. However, development of human society demands tremendous energy, which is mainly produced by the combustion of fossil fuel, resulting in enormous greenhouse gas emission into the atmosphere. According to the data from IPCC [2], the greenhouse gases (GHG) concentrations in the atmosphere are at unprecedented levels in the last 800,000 years. Since 1750, the concentrations of methane (CH_4) and nitrogen oxides (mainly N_2O) have grown by 150% and 20% respectively, while carbon dioxide (CO_2) has increased by 40%. CO_2 emission from fossil fuel combustion and industrial processes made the main contribution (about 78%) to the entire greenhouse gases emission increase during the period of 1970~2010. Between 2000 and 2010, total GHG emissions caused by human activities increased about 10 $GtCO_2$-eq every year and 47% of the increase is contributed by energy producing.

Meanwhile, IPCC [2] found out that the worldwide averaged temperature with land and ocean surfaces considered have increased by 0.85 °C between 1880 and 2012. Over the period from 1979 to 2012, the annual mean area of ice reduced at a rate of about 4% each decade in Arctic sea.

The growth of temperature within the ocean and atmosphere have diminished the glacier and snow amounts and risen the sea level. During the last two decades, mass-losing has been found in the worldwide glaciers and the Antarctic ice sheets. During the years between 1901 and 2010, the worldwide average sea level rose by 19cm while the recent (since the 19th century) sea level rising rate is larger than the average value over the last 2000 years. By studying the method introduced by Arrhenius and Calendar and comparing the results with the modern Earth System Models (ESMs), Thomas et al. [1] found out that the results from ESMs are robust and trustworthy. They concluded that the global climate will experience a significant warming in the twenty-first century causing by the emission of greenhouse gases.

Moreover, up to 40% of the CO_2 produced by human activities emitted to the atmosphere is absorbed by the sea water has acidified the ocean [3]. Calculations based on the results measured on the ocean surface and the understanding of ocean chemistry have shown that the CO_2 absorption by the ocean has decreased the pH on surface of seawater by 0.1, which corresponds to an increase of about 30% of the hydrogen ions in concentration because the value of pH is calculated by the logarithmic scale [4]. If no means are adopted to reduce the CO_2 emission by human activities, this value could rise up to 0.5 by the year of 2100 [5]. Because of the acidification, the dissolution of $CaCO_3$ in all water column is around 55% of the export production of $CaCO_3$ [6]. It indicates that it is harder for sea-born calcifying species to form biogenic $CaCO_3$, which will lead the food chains connected with the oceans to big problems [7].

Some researchers believe that our earth system has reached its tipping point where catastrophic climates will be more common if our society refuses to reduce our GHG emissions [8].

CHAPTER 2

LITERATURE REVIEW

2.1 Path to Reduction of Carbon Emission

Several technologists have been introduced to reduce the anthropogenic CO_2 emission to the atmosphere [9]: A) By increasing the energy conversion rate, transport and end-use efficiency, the fossil fuel consumption and CO_2 emission than can be reduced; B) By replacing the high carbon-intensive fossil fuels with lower carbon-intensive fuels like natural gas, reduction of CO_2 emission can also be achieved; C) Increasing the use of low-carbon energy like nuclear power and geothermal energy can be an alternative option to lower the carbon emission; D) By improving the capacity of natural and biological sinks like agricultural and forestry practices, large amount of CO_2 can be stored biologically; E) CO_2 capture and storage (CCS) technology is another potential approach to cut down the CO_2 density in the atmosphere.

2.2 Carbon Capture and Storage Technology

The scenes of carbon capture and storage (CCS) technology application mainly include power generation, oil refining, cement manufacture, iron and steel producing and other energy-intensive cases. To transport and store a large amount of CO_2 to the proper storage location, gaseous CO_2 need to be compressed to its dense phase to reduce its volume. Several concepts (or practicing method) have been introduced to store a large quantity of CO_2. The first way is to inject CO_2 into natural reservoirs or deep ocean. Injecting CO2 into gas and oil well, saline formations and deep coal seams have been put into practice because it is also a method to enhance the production. Other ways to storage CO_2 like using it as a crude material for chemical productions are also introduced.

There are three basic configurations for CO_2 capture and storage used in electricity generation plant, as indicated in Figure 1 below.

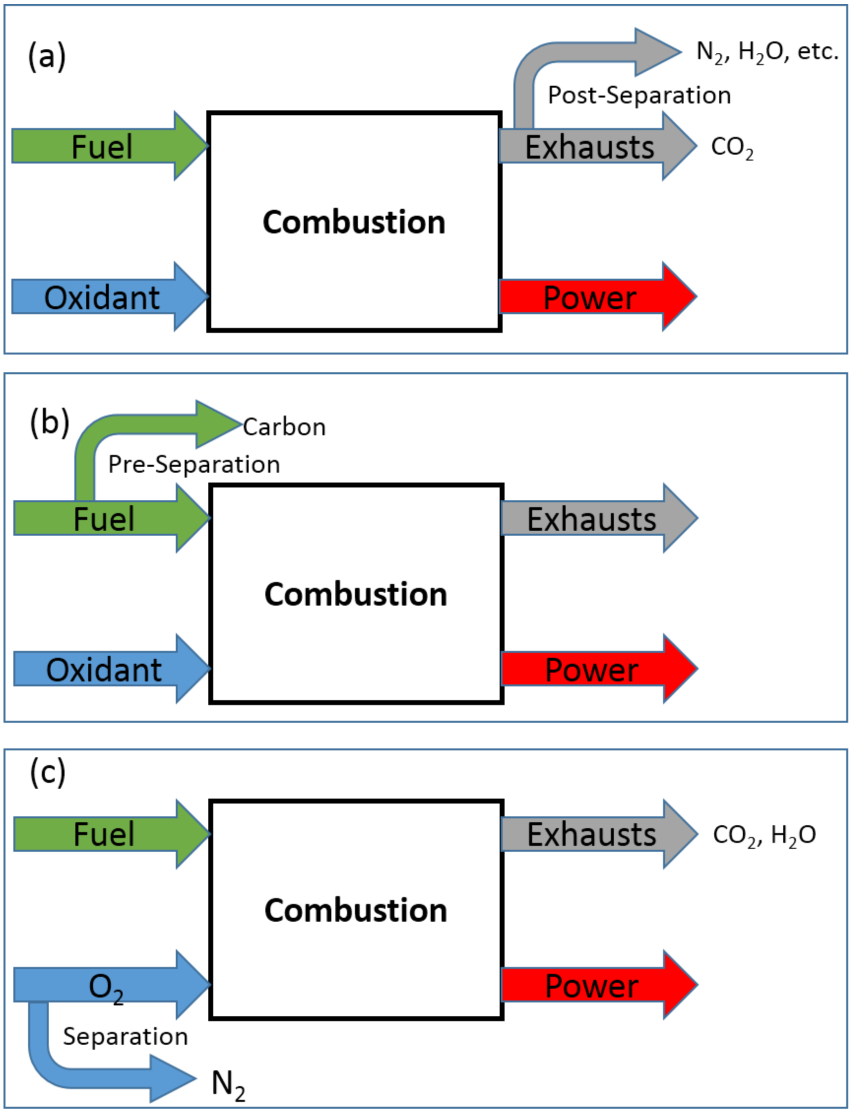

Figure 1 Basic configurations of CCS: (a) Post-Combustion separation, (b) Pre-Combustion separation and (c) Oxyfuel Combustion.

Figure 1a shows the schematic of a post-combustion carbon capture and store system. In the post-combustion system, fuel and air are fed into the combustion chamber and combust to generate heat, then the CO_2 gas will be separated from the exhaust gas with proper methods. Since the separation process is taken after the combustion process in this type of system, it is called “Post-Combustion” system. As shown in Figure 1b, the pre-combustion system de-carbonized the fuel before it is fed into the combustion chamber. Since no carbon element is contained in the fuel, CO_2 will not be produced after the combustion. The 3rd type layout Figure 1c showing is the oxy-fuel combustion. Oxygen is separated from the air before combustion, and then relative pure oxygen is fed into the furnace chamber to combust with fuel. With such relative pure oxidant using in the combustion process, only CO_2 gas and H_2O vapor are produced. After condensing water vapor, the CO_2 gas can be compressed, transported and stored finally.

However, most of the technical method for CSS have negative impacts on the overall efficiency or cost a large quantity of energy to split the CO_2 from the exhaust gases on the outlet [10], this will lead to a price increase of the energy.

2.3 Chemical Looping Combustion Technology

In order to reduce the irreversible entropy produced by the conventional combustion processes, H. Richter and K. Hnoche [11] proposed a new combustion method which uses metal oxides as the mediums between oxygen and fuel. Inspired by this idea, Chemical Looping Combustion (CLC) technology was proposed as a potential technology to achieve CSS with low energy requirement [12]. As a novel technique for CSS, Chemical Looping Combustion is a using the same principle as oxy-fuel combustion does. Rather than using huge quality of energy to separate the O_2 from the air before combustion directly, oxygen carrier solid (in granule form) is introduced. As indicated in Figure 2, in chemical looping combustion systems, the oxygen carrier particles are used to react and absorb O_2 from the air within the reactor called air reactor (AR) firstly, then these particles with elemental form oxygen are transported into another reactor called fuel reactor to react with fuel. Since no air is directly fed into fuel reactors, the main ingredients of the exhaust gas discharged from combustion chamber are CO_2 and H_2O vapor. CO_2 gas can be separated conveniently through the condensation of H_2O vapor into liquid form. The CLC technology has high potential to accomplish the carbon separation process with less overall efficiency reduction in energy since the high energy consumption CO_2 separation process is eliminated.

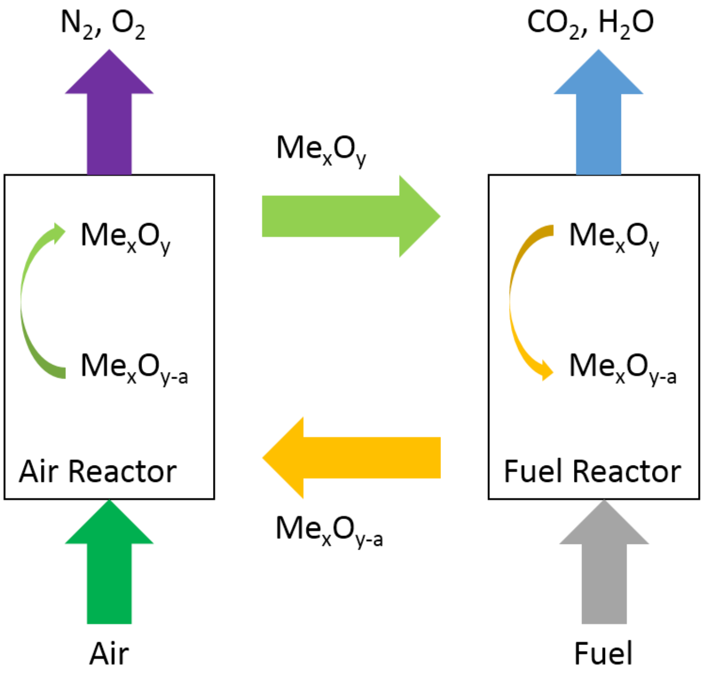

Figure 2 General schematic of the CLC system

In CLC systems, oxygen carrier could be selected from metal oxide or pure metal particles and is usually circulating between FR and AR in oxidized (Me_xO_y) and reduced (Me_xO_{y-a}) forms. Within air reactor, the oxidizing reaction occurs, as expressed in Eq. (2.1).

$$Me_xO_{y-1} + \frac{1}{2}O_2 = Me_xO_y \tag{2.1}$$

On the other hand, a reduction reaction occurs in the FR, as expressed in Eq.(2.2).

$$(2m+n)Me_xO_y + C_mH_{2n} = (2m+n)Me_xO_{y-1} + mCO_2 + nH_2O \qquad (2.2)$$

It is necessary to note that both the oxidizing reaction and reduction reaction could be exothermic reactions according to the fuel used and the material of oxygen carrier, while the oxidizing reaction could only be an exothermic reaction. However, the heat produced by the overall system is the summation of the heat released by each step and is the identical value of the traditional combustion, where fuel and air are directly fed into the furnace chamber and combust. Hence, the overall reaction in a complete CLC system can be considered as the same reaction in normal combustion, as expressed in Eq.(2.3).

$$C_mH_{2n} + \left(m + \frac{n}{2}\right)O_2 = mCO_2 + nH_2O \qquad (2.3)$$

The most widely used layout of CLC systems is the dual circulating fluidized bed (DCFB) system which normally consists of two fluidized bed reactors interconnected to each other, hence the oxidized form oxygen carrier reacting with fuel in FR and the reduced form oxygen carrier reacting with oxygen in the AR can be transported between these two reactors continuously. As indicated in Figure 3, the basic CLC system components include a fuel reactor, an air reactor, a cyclone, and several (usually two) loop-seals. The reduced form oxygen carrier particles coming from fuel reactor and air are fed into air reactor, then driven by the highly fluidized condition in AR, the OC particles react with oxygen and be oxidized to form oxidized form oxygen carrier particles. For the purpose to transport the oxidized form particles out of air reactor and feed them into fuel reactor, air reactors are designed to be high-speed fluidized beds within which the OC particles can be raised out from their top. In air reactor, the air is fed with a high speed and oxygen carrier particles are raised and transported out of air-reactor from the top side of the reactor. Then the oxygen carrier particles in oxidized form are split from the residual air within the cyclone and transported into fuel reactor. However, due to the pressure difference between cyclone and fuel reactor, an upper loop-seals are placed between them to balance the pressure difference and hence lower the leakage. After reacted with fuel within FR, the oxygen carrier particles in reduced form are carried into air reactor and complete the cycle in the dual circulation fluidized bed CLC system. The lower loop-seals are also applied between fuel reactors and air reactors for the same reason as upper loop-seals involved.

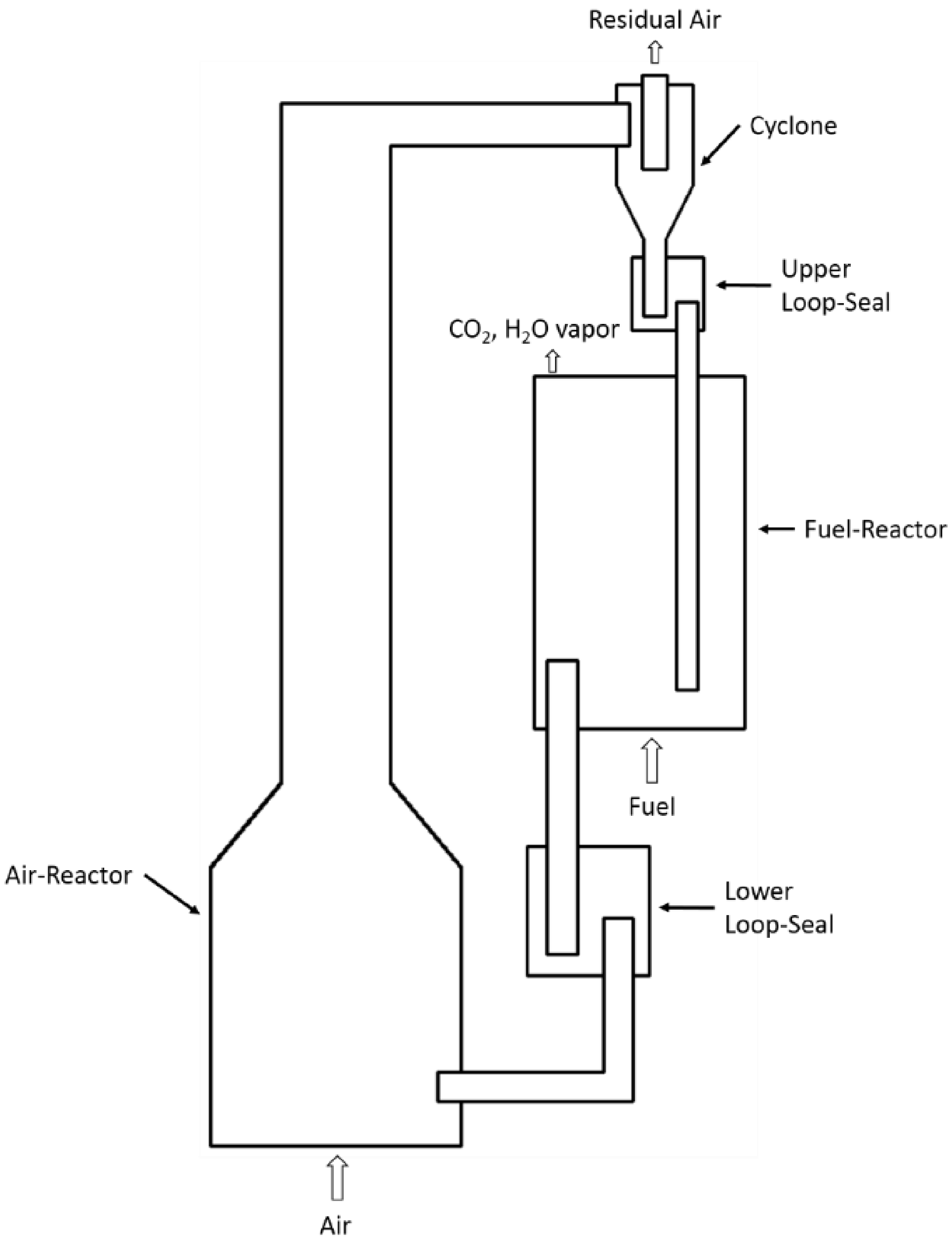

Figure 3 Dual circulating fluidized bed layout.

2.4 Academic Research on CLC

Recent studies of this potential technology have mainly focused on three areas: mathematical and numerical studies of reactors and complete CLC systems, experimental studies of CLC units, and the experimental studies of different materials used as oxygen carriers.

Computational Fluid Dynamics (CFD) is a rapidly developing method to facilitate the research on the fields of hydrodynamics, heat exchange, et al. CFD is widely used in the study of CLC systems within which the hydrodynamics, chemical reactions, and heat exchange are considered systematically.

Adánez et al. [13] performed a model mathematically for only the fuel reactor considering both the hydrodynamics and reaction kinetics behavior. Simulations with various operating conditions were conducted to enhance the chemical reaction performance of fuel reactor using $CuOSiO_2$ as oxygen carrier and CH_4 as fuel. Further, using the MFIX code, Jung et al. [14] conducted a multiphase CFD-based model for a fuel reactor. The fuel conversion rate (50%) was lower than the value in Adánez et al. [13]'s work.

Early in 2002, Kim and Sohn [15] have tested the chemical reaction behavior of $CaSO_4$ and H_2 and provided the relation between conversion rate of $CaSO_4$, reaction time, the partial pressure of H_2, and reaction temperature. Using the data from Kim [15] to define the reaction rate within the fuel reactor, Deng et al. [16] simulated a fuel reactor model using $CaSO_4$ as oxygen-carrier and H_2 as fuel. They found out that faster gas feeding velocity, lower fuel reactor bed temperature, and larger particle diameter lead to a lower conversion rate of fuel. Further, A. B. Harichandan and T. Shamim [17] used the same oxygen-carrier material and fuel type as Deng et al. did ($CaSO_4$ and H_2) to study the formation of the quasi-steady state in fuel-reactor. Continuous and detailed bubble formation, rise and burst were observed in their study. Moreover, they not only confirmed

Deng et al.'s prediction that nano-size oxygen-carrier contributes to fuel conversion rate, but also discuss the impact of reactor geometry on fuel conversion rate. The highest fuel conversion rate in A. B. Harichandan and T. Shamim's result is 63%, though it should be noted that this value can be affected by several parameters such as the geometry of fuel-reactor, initial solid volume fraction, and oxygen-carrier particle size.

A complete system with not only fuel reactor but also air reactor considered was studied. By separating the system into air reactor simulation and fuel reactor simulation, but connecting the two parts by using the exchange of solid mass, H. Kruggel-Emden et al. [18] studied different system configurations. They pointed out that the air reactor they used can supply enough oxygen carrier in oxidized form for the fuel reactor. Hence, the system did not release adequate heat. However, the computational time of the CLC simulation can be reduced dramatically by separating the CLC system into two calculation sections.

Zhang et al. [19] conducted a 3D simulation for a semi-industry circulating fluidized bed. The numerical results of solid volume fraction on cross sections, solid velocity, and pressure profiles were reasonably in the agreement with laboratory data.

Wang et al. [20] complemented the simulation of a more complicated dual circulating fluidized bed system and evaluated the results using a new drag model called cluster structure-dependent model. The predicted profile of gas components and temperature were in fine agreement with laboratory data.

Peng et al. [21] studied numerically the circulation rate of oxygen carrier in the models with only hydrodynamics considered using discrete element method and their results have reasonable agreements with experimental data. They found out that the fluctuation frequency and amplitude of oxygen carrier circulation rate mainly depend on the turbulent flow regime in the AR. Moreover, solid circulation rate is found to have a logarithmic relationship with the flow rate in air reactor and a linear relationship with a flow rate in fuel-reactor. James M. Parker [22] studied a full 3-D model of a complete CLC system using Barracuda VR software. The fluidization, circulation rate, efficiency of air reactor and fuel reactor, and the temperature profile were discussed in this paper. Back in 2003, Yang et al. [23] derived a drag model to calculate the momentum transfer coefficient between gas and solid phases based on energy minimization multi-scale (EMMS) approach. The behavior of solid-gas flow was simulated in an air reactor. Laboratory data is compared with simulation results calculated with different drag models by Guan et al. [24]. They concluded that good agreements can be gained between experimental data and predictions by using different drag models derived by Syamlal & O'Brien [25], Gidaspow [26], especially for the air reactors.

Mendiara et al. [27] studied a small CLC system (500 W_{th}) using the bauxite waste as oxygen carrier (mainly Fe-enriched sand fraction), and coal particles as feeding fuel. The effects of feeding rate of coal particles, gasifying gas composition, fuel reactor temperature, and the circulation rate of OC were discussed. Then concluded that in order to have high carbon capture ratio, higher temperatures would be needed. Using iron ore as oxygen carrier, bituminous coal and wood char as fuel, Linderholm et al. [28] estimated the efficiency of carbon capturing and the rate of fuel conversion in a 100W_{th} CLC system. The results turned out to be very impressive with the bituminous coal conversion rate of 87%, the wood char conversion rate of 93%, and the carbon capture efficiency of 94~98%. Rajendran et al. [29] evaluated the effects of the number of reduction cycles, the temperature of reaction, and type of fuel on the running performance of a 100kW$_{th}$ fluidized bed using Fe-bases material (95% is Fe_2O_3) as oxygen carrier and coal particles as fuel. They found out that the conversion rate was 91% for coal while was 57% for char. The highest CO_2 concentration (25%) was obtained at 1000°C, but the highest conversion rate (91%) was gained at 900°C. A recent study was conducted by Yang et al. [30] who investigated the chemical thermodynamics of an in-situ gasification CLC (IG-CLC) system using $CaSO_4$ as OC and coal as fuel. Both of their mathematical and experimental works showed that $CaSO_4$ is a remarkable OC for IG-CLC systems. Their results showed that reaction between solid-solid and solid-gas phases contribute to the major syngas production. Moreover, water vapor and carbon dioxide were found to be positive factors for syngas outcome. Besides coal, biomass was also tested as fuel by Ge et al. [31] in a 25kW$_{th}$ system. They found out that the syngas yield can be optimized at operating temperature of 750°C and 30 wt.% of NiO in OC. Meanwhile, CaO-decorated NiO/Al_2O_3 OC can also contribute to better quality of syngas.

Besides hydrodynamics and chemical kinetics, the radiative heat transfer of circulating fluidized beds was investigated by Bordbar et al. [32] and Singh et al. [33] numerically. However, according to our review of literature, the research on radiative heat transfer within reactors was hardly conducted, nor the effects of radiative heat transfer on flow pattern and fuel conversion performance were clearly declared, especially for CLC systems. Aiming at proving a mathematical model for the radiative heat transfer within reactors of CLC system and conducting a numerical research on it, this study pays most of the attention on the radiative heat transfer with FR and investigates the effects caused by it.

Table 1 List of literature review of CLC system study

Authors	Geometry	Methodology	Research outcomes
Richter et al., 1983, [11]		Mathematical	Proposed a new combustion method which uses metal oxides as the mediums between oxygen and fuel to reduce the irreversible entropy.
Yang et al. 2003, [23]	2D, air reactor	Mathematical & numerical	Proposed a drag model for calculating the interphase momentum transfer coefficient from energy minimization multi-scale (EMMS) approach.
Adánez et al., 2003, [13]	2D, fuel reactor	Numerical	Performed a model mathematically for only the fuel reactor considering both the hydrodynamics and reaction kinetics behavior. Simulations with various operating conditions were conducted to enhance the chemical reaction performance of fuel reactor employing $CuOSiO_2$ as oxygen carrier and CH4 as fuel.

Jung et al., 2008, [14]	2D, fuel reactor	Numerical	Using the MFIX code, Jung et al. set up a multiphase CFD-based model for a fuel reactor.
Kim et al., 2002, [15]	3D, TGA	Experimental	Tested the chemical reaction behavior of $CaSO_4$ and H_2 and provided the relation between conversion rate of $CaSO_4$, reaction time, the partial pressure of H_2, and reaction temperature.
Deng et al., 2009, [16]	2D, fuel reactor	Numerical	Using experimental data to define the reaction rate within the fuel reactor, they conducted a fuel reactor model using $CaSO_4$ as oxygen carrier and H_2 as fuel. They concluded that faster gas feeding velocity, lower fuel reactor bed temperature, and larger particle diameter leads to lower conversion rate of fuel.
Harichandan et al., 2014, [17]	2D, fuel reactor	Numerical	Using $CaSO_4$ as oxygen carrier and employing H_2 as fuel, studied the formation of the quasi-steady state in fuel-reactor. Discuss the impact of reactor geometry, diameter of particles on fuel conversion rate.

Kruggel-Emden et al., 2010, [18]	2D, fuel reactor, air reactor	Numerical	Studied different system configurations by separating the system into air reactor simulation and fuel reactor simulation, but connecting the two parts by using the exchange of solid mass.
Zhang et al., 2008, [19]	3D, fuel reactor, air reactor	Numerical	Conducted a 3D simulation for a semi-industry circulating fluidized bed. The numerical results of solid volume fraction on cross sections, solid velocity, and pressure profiles were in fine agreement with laboratory results.
Wang et al., 2014, [20]	2D, dual circulating fluidized bed	Numerical	Complemented the simulation of a more complicated dual circulating fluidized bed system and evaluated the results using a new drag model called cluster structure-dependent model. The predicted profile of gas components and temperature were in fine agreement with laboratory data.

Peng et al., 2015, [21]	3D, circulating fluidized bed	Numerical & experiment	Studied numerically the circulation rate of oxygen carrier in the models with only hydrodynamics considered using discrete element method. The results have reasonable agreements with experimental data.
James M. Parker, 2014 [22]	3D, fuel reactor, air reactor	Numerical	Studied a full 3D model of a CLC system contains an air reactor, a fuel reactor, a cyclone, a loop seal and an L-valve using Barracuda VR software. Discussed the fluidization, circulation rate, efficiency of air reactor and fuel reactor, and the temperature profile.
Guan et al., 2014, [24]	3D, fuel reactor, air reactor	Numerical	Conducted a numerical simulation using three types of drag models, then compared the numerical results calculated with different drag models to laboratory data.
Mendiara et al., 2013, [27]	3D, circulating fluidized bed	Experiment	Studied a small CLC system (500 Wth) using the bauxite waste as oxygen carrier (mainly Fe-enriched sand fraction), and coal particles as feeding fuel. The effects of feeding rate of coal particles, gasifying gas composition, fuel reactor temperature, and the circulation rate of

			OC were discussed. Then concluded that in order to have high carbon capture ratio, higher temperatures would be needed.
Linderholm et al., 2016, [28]	3D, circulating fluidized bed	Experiment	Estimated the efficiency of carbon capturing and the rate of fuel conversion in a 100Wth chemical looping combustion system using cheap oxygen carrier (i.e. iron core) and conventional fuel (bituminous coal and wood char).
Rajendran et al., 2016, [29]	3D fluidized bed	Experiment	Evaluated the effects of the number of reduction cycles, reaction temperature, and fuel type on the running performance of a 100kWth fluidized bed using coal particles as fuel and Fe-bases material (95% is Fe_2O_3) as oxygen carrier.
Yang et al., 2017, [30]	3D CLC system	Mathematical & experimental	Optimal conditions for syngas outcome were tested. Results showed that reaction between solid-solid and solid-gas phases contribute to the major syngas production. Moreover, water vapor and carbon dioxide were found to be positive factors for syngas outcome.

Ge et al., 2015, [31]	3D, circulating fluidized bed	Experimental	Biomass fuel was tested in a circulating fluidized bed with optimized conditions to enhance syngas output. CaO-decorated NiO/Al_2O_3 OC was tested to be a good material for syngas outcome.

Today, various types of materials were tested as the oxygen carrier particles for CLC systems. Several characteristics are required to ensure the good performance of a certain type of material used as oxygen carrier [12]: a) It should be stable at high temperature while cycling under oxidation and reduction reactions. b) It should be able to be fluidized. c) It should be resistant to agglomeration. d) It should have enough mechanical strength to resist to the friction stress between particles. And e) It should be environmental and friendly and economically acceptable.

The most studied metal oxide materials used as oxygen carrier are Iron (Fe) based metal oxide, Nickel(Ni) based metal oxide, Cobalt (Co) based metal oxide, Copper(Cu) based metal oxide, and Manganese(Mn) based metal oxide.

Fe-based oxygen carriers have their advantages in economy and environment considerations, making it an attractive material for CLC systems. However, Fe bases materials have lower oxygen transport capacity and are inefficient reactants in fuel reactors. Different forms of Fe oxide (Fe_3O_4, FeO, and Fe) can be found from Fe_2O_3 reduction reaction in fuel reactor. However, only the materials transformed between Fe_2O_3 form and Fe_3O_4 form are considered in industry CLC systems.

Benefiting from its good reactivity, Ni-based materials perform well as oxygen carriers, especially at high temperature. However, due to their inherent high reducibility, CO and H_2 can be produced within the fuel reactor. Besides, Ni-based materials are relatively expensive than other materials.

Similar to Ni-based materials, oxygen carriers using Co-based metal oxides have the economic and environmental disadvantages. However, Co based materials have widely tested because of its good oxygen transport capacity. Since Co_3O_4 is unstable above 900°C, only the transformations among CoO and Co are considered in CLC applications.

Oxygen carriers made from Cu-based materials were provided to have advanced properties of high oxygen transfer capacity and high reactivity. Pure CuO oxygen carrier has high reactivity even at low temperature, yet its oxidation reaction rate decreases with the larger number of cycles.

Mn-based oxides are low cost, environmental friendly oxygen carriers with higher oxygen transport capacity compared to Fe-based materials. Only the transformation between Mn_3O_4 and MnO is considered for CLC applications.

Varied materials (Al_2O_3, MgO, $MgAl_2O_4$, SiO_2, TiO_2, ZrO_2, etc.) are used as the support materials for pure metal oxide to enhance their mechanical strength, to improve the chemical reaction performance, and to minimize the percentage of toxic metals of oxygen carriers.

The oxygen transport capacity and another critical parameter to differ the performance of materials. The oxygen transport capability, R_o, is defined by Eq. (2.4).

$$R_o = \frac{m_o - m_r}{m_o} \tag{2.4}$$

Where, m_o is the mass of fully oxidized form oxygen carrier, and m_r the reduced form.

The oxygen transport capability of various commonly used oxygen carriers is shown in Figure 4.

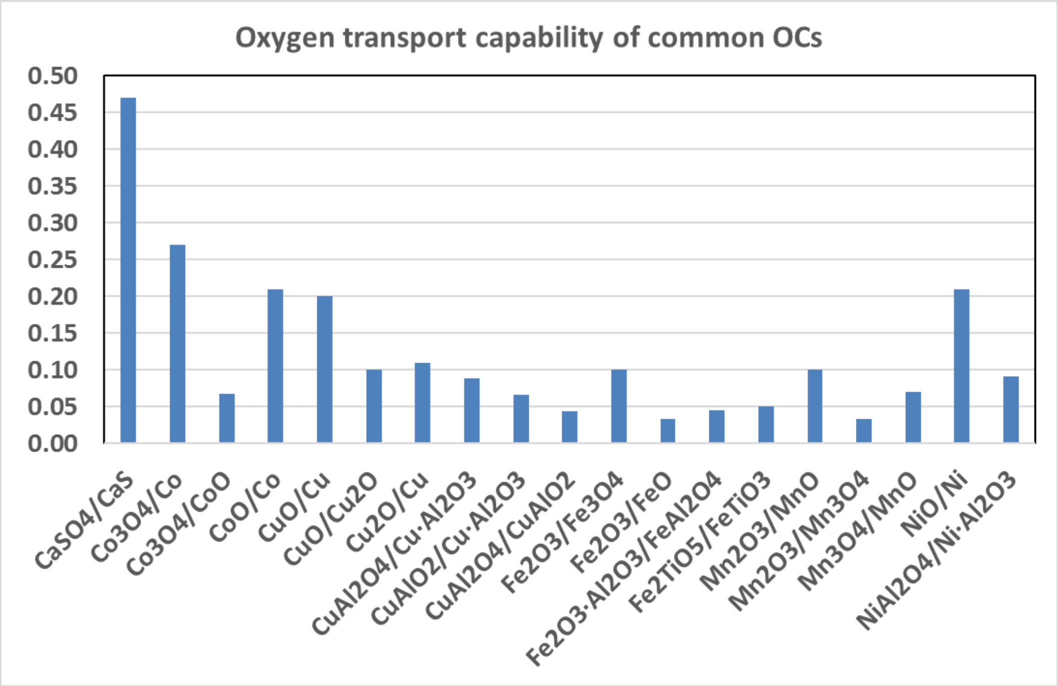

Figure 4 Oxygen transport capability of common OCs.

Table 2 List of literature review of OC study

	Oxygen Carrier Material	Reduction Agents	Experimental Facility
Nakano et al. [34]	Fe_2O_3	H_2	TGA
Go et al. [35], [36]	Fe_2O_3, Mn_3O_4, $MnCO_3$, ZnO	CH_4	TGA
Linderholm et al. [28]	Fe_2O_3 (74.8 wt.%)	Bituminous coal and wood char	Fluidized bed
Kang et al. [37]	Fe_2O_3 (20 wt.%)/ZrO_2	CH_4, CO, and H_2	TGA
Mendiara et al. [27]	Fe-enriched sand fraction (Fe-ESF)	Coal	Fluidized bed
Ishida et al. [38]	NiO	H_2	TGA
Erri et al. [39]	NiO	H_2	TGA
Zhou et al. [40]	NiO	H_2	TGA
Jiang et al. [41]	NiO (15.5 wt.%), Al_2O_3 (80.5 wt.%), $NiAl_2O_4$ (4.0 wt.%)	$C_3H_8O_3$	Fixed Bed
Roux et al. [42]	NiO (Pure), NiO (60 wt.%), Al_2O_3 (40 wt.%)	CH_4	TGA
Zafar et al. [43]	NiO, CuO, Fe_2O_3, $MgAl_2O_4$ (Support material), SiO_2 (Support material)	CH_4	TGA
Rubel et al. [44]	CoO	Syngas	TGA

Diego et al. [45]	CuO	CH_4, Syngas	Fluidized bed
Tian et al. [46]	CuO/bentonite,	CO, H_2	TGA
Siriwardane et al. [47]	CuO, Fe_2O_3, Co_3O_4, NiO, Mn_2O_3	Coal	TGA, Fixed bed
Mattisson et al. [48]	CuO, Co_3O_4, Mn_2O_3, NiO, Al_2O_3 (Support material)	CH_4	TGA
Adanez et al. [49]	Mn_3O_4	CH_4	TGA
Niu et al. [50]	CuO/Fe_2O_3	Sewage sludge	Fluidized bed
Zhang et al. [51]	$Fe_2O_3/CaSO_4$	Syngas	Fixed bed
Larring et al. [52]	Fe-Mn-based minerals	CH_4, H_2	TGA
Frick et al. [53]	CuO- Fe_2O_3, NiO- Mn_3O_4	CH_4, Syngas	Fluidized bed
Perreault et al. [54]	Mineral ores (ilmenite, pyrolusite)	CH_4	Fixed bed
Su et al. [55]	Hematite	CO	TGA
Mohammad M. Hossain et al. [56]	$Co–Ni/Al_2O_3$	CH_4	Fluidized bed

2.5 Design Criteria of CLC Systems

Criteria and method of designing CLC systems were proposed by Zafar et al. [57], [58]. A CLC system with good performance should a) have enough OC to fully convert fuel into CO_2 and H_2O vapor, and b) have enough OC circulation rate to maintain the temperature difference between two reactors within a reasonable range.

Assuming full conversion of fuel, according to Zafar et al., OC circulation rate can be obtained by transport capacity of OC and incremental conversion of OC in FR. Meanwhile, circulation rate of OC also depends on operational conditions and riser configuration. Moreover, the average of the cross-sectional area of riser should be limited within the range of 20~100 $kgm^{-2}s^{-1}$. According to Zafar et al. [57], the temperature difference between AR and FR is a linear function of incremental conversion of OC.

On the other hand, reactors should have enough solid inventory to meet the design capacity of CLC systems. Solid inventory of OC needs to be calculated by considering the reactivity between OC and fuel. Hence, the contact time between fuel and OC particles should larger than full conversion time. However, larger solid inventory increases power consumption by fans or compressors to feed gas into AR and FR. Thus, optimization of the solid inventory of OC is preferred.

2.6 Research objectives

The literature review shows that though hydrodynamics were rigorously studied, only uniform gases velocity profile was used to fed air and fuel into reactors. Besides, important parameters including particle size, superficial feeding velocity, operating temperature, etc. are not yet discussed in details. Meanwhile, heat transfer, especially radiation heat transfer within both the air reactor and fuel reactor are not widely studied.

The objectives of this research are to:

a) Formulate detailed mathematical models for both the air reactor and fuel reactor including hydrodynamics, heat transfer including a simple model for radiation, and chemical reactions.

b) Implement the mathematical model and perform simulations for a CLC system using a commercial software and necessary user define functions.

c) Investigate the effects of important parameters of CLC system including fluidization methods and particle diameter, etc. on fuel conversion rate.

CHAPTER 3

MATHEMATICAL MODELS

3.1 Governing Equation Sets and Assumption

Present work considers not only the hydrodynamics but also the heat transfer behavior (including the radiative heat transfer) and chemical reaction kinetics of CLC systems. A gas-solid multiphase granular model is applied to describe the behavior of the gas-solid mixture flow. The conservation equations of mass, momentum, and energy are solved for each phase with a single pressure for all phases. However, differs from the gas phase, the collision and fluctuation of the solid particles with solid phase should not be neglected, especially in the regions with dense solid particles. Meanwhile, the interactions between gas and solid phase also need to be specified. Hence, the kinetic theory of granular flow (KTGF) is introduced as a set of transport equations. Besides, the radiative heat transfer equation (RTE) which requires several radiative properties is also solved when the radiative heat transfer is considered. As an important aspect of CLC system, the chemical reaction kinetics between gas and solid phase determines the conversion performance and other parameters of the system. Hence, proper models should be applied to describe the chemical reactions with FR and AR respectively.

However, several assumptions are made in present study. a) The two phases in the reactor are gas and solid, H_2O is in the vapor phase. b) The oxygen-carrier granules are assumed to be spherical and uniform in size, inelastic, smooth and monodispersed spheres. c) Only the reactions described by Eq. (2.1) and (2.2) is considered. Other side reactions are neglected since they are significantly compressed.

3.2 Continuity Equations

The general continuity equation for phase q can be written as

$$\frac{\partial}{\partial t}\left(\alpha_q \rho_q\right) + \nabla \cdot \left(\alpha_q \rho_q v_q\right) = \sum_{p=1}^{n}\left(\dot{m}_{pq} - \dot{m}_{qp}\right) + S_q \tag{3.1}$$

Where, $\dot{m}_{pq}$ presents the mass transfer rate from p^{th} phase to q^{th} phase, and $\dot{m}_{qp}$ from q^{th} phase to p^{th} phase. It is clear that $\dot{m}_{pq} = -\dot{m}_{qp}$.

Since the heterogeneous chemical reaction between gas phase and solid phase is considered in this study, the mass transfer between solid and gas phases, $\dot{m}_{pq}$ and $\dot{m}_{qp}$ are not zero. S_q characterizes the source term of mass for phase q. S_q is set to zero in this study.

Hence, the continuity equation for gas phase becomes

$$\frac{\partial}{\partial t}\left(\alpha_g \rho_g\right) + \nabla \cdot \left(\alpha_g \rho_g v_g\right) = \dot{m}_{sg} \tag{3.2}$$

And, for solid phase is

$$\frac{\partial}{\partial t}(\alpha_s\rho_s) + \nabla \cdot (\alpha_s\rho_s v_s) = \dot{m}_{gs} \tag{3.3}$$

Where, $\dot{m}_{sg} = -\dot{m}_{gs}$, is the rate of mass transfer between solid and gas phases.

3.3 Conservation Equations of Momentum

The general conservation equation of momentum for phase q is

$$\begin{aligned}
\frac{\partial}{\partial t}\left(\alpha_q\rho_q v_q\right) + \nabla \cdot \left(\alpha_q\rho_q v_q v_q\right) \\
&= -\alpha_q \nabla \mathrm{P} + \nabla\tau_q + \alpha_q\rho_q \mathrm{g} \\
&+ \sum_{p=1}^{n}\left(R_{pq} + \dot{m}_{pq}v_p - \dot{m}_{qp}v_q\right) \\
&+ \left(F_q + F_{lift,q} + F_{wl,q} + F_{vm,q} + F_{td,q}\right)
\end{aligned} \tag{3.4}$$

Here, F_q , $F_{lift,q}$, $F_{wl,q}$, $F_{vm,q}$ and $F_{td,q}$ are the external body force, lift force, wall lubrication force, virtual mass force and turbulent dispersion force for phase q respectively. Since gravity has been considered in the $\alpha_q\rho_q \mathrm{g}$ term, and no external body force in other forms exist, F_q is set to zero. Due to fact that the size of solid particles is very small and the volume fraction of solid is high, $F_{lift,q}$ is not included. Because the density of solid phase is much larger than gas phase and the velocity difference is not very large, $F_{vm,q}$ is set to zero. Besides, $F_{td,q}$ is the turbulent dispersion force. It can be represented as

$$F_{td,q} = -F_{td,p} = -f_{td,limitting}K_{pq}v_{dr} \tag{3.5}$$

Where, v_{dr} is the drift velocity and $f_{td,limitting}$ is a factor that can be used to impose a limiting function on the turbulent dispersion force. According to Lopez de Bertodano [59], $F_{td,q}$ can be expressed as

$$F_{td,q} = -F_{td,p} = C_{TD}\rho_q k_q \nabla \alpha_p \tag{3.6}$$

However, compared to other forces, $F_{td,q}$ is not significant. Hence, $F_{td,q}$ is not considered in this case. $F_{wl,q}$ is not considered and set to zero as well.

The stress-strain tensor of q^{th} phase in momentum equation can be written as

$$\tau_q = \alpha_q \mu_q \left(\nabla v_q + \nabla v_q^T\right) + \alpha_q \left(\lambda_q - \frac{2}{3}\mu_q\right) \nabla v_q I \tag{3.7}$$

Where, μ_q and λ_q are the shear and bulk viscosity of phase q respectively. However, for gas phase, $\lambda_g = 0$. I is the unit tensor, and g $= 9.81\, m/s^2$ is the gravitational acceleration.

Meanwhile, R_{pq} is the rate of interphase momentum exchange from phases p to phase q. It is also clear that $R_{pq} = -R_{qp}$. R_{pq} can be determined by

$$R_{pq} = K_{pq}\left(v_p - v_q\right) \tag{3.8}$$

Evidentially, $R_{pq} = -R_{qp}$.

Where, K_{pq} is the coefficient of interphase momentum exchange. R_{pq} can be influenced by friction, pressure, cohesion etc. For fluid-solid multiphase, several models are available to calculate K_{pq}, for instance, Syamlal-O'Brien model [60], Wen and Yu model [61], Gidaspow model [62] etc.

Hence, the conservation equation of momentum for gas phase and solid phase can be expressed as

$$\frac{\partial}{\partial t}\left(\alpha_g \rho_g v_g\right) + \nabla \cdot \left(\alpha_g \rho_g v_g v_g\right) = -\alpha_g \nabla \mathrm{P} + \nabla \tau_g + \alpha_g \rho_g \mathrm{g} + R_{sg} + \dot{m}_{sg} v_s - \dot{m}_{gs} v_g \tag{3.9}$$

$$\frac{\partial}{\partial t}(\alpha_s \rho_s v_s) + \nabla \cdot (\alpha_s \rho_s v_s v_s) = -\alpha_s \nabla \mathrm{P} - \nabla P_s + \nabla \tau_s + \alpha_s \rho_s \mathrm{g} + R_{gs} + \dot{m}_{gs} v_g - \dot{m}_{sg} v_s \tag{3.10}$$

It is worth noting that differs from the conservation equation of momentum for gas phase, the impact of granular pressure ∇P_s is considered in the solid phase.

3.4 Conservation Equations of Energy

The conservation equation of energy for gas phase in gas-solid multiphase flow is

$$\frac{\partial}{\partial t}\left(\alpha_g \rho_g h_g\right) + \nabla \cdot \left(\alpha_g \rho_g v_g h_g\right) = \nabla\left(\lambda_g \nabla T_g\right) + Q_{gs} + S_g \tag{3.11}$$

And, for solid phase is

$$\frac{\partial}{\partial t}(\alpha_s \rho_s h_s) + \nabla \cdot (\alpha_s \rho_s v_s h_s) = \nabla(\lambda_s \nabla T_s) + Q_{sg} + S_s \tag{3.12}$$

Where, h is the specific enthalpy, λ is the thermal conductivity, Q is heat exchange between the two phases, $Q_{gs} = -Q_{sg}$.

Q can be expressed as

$$Q_{gs} = h_{gs}(T_s - T_g) = -Q_{sg} \tag{3.13}$$

Where, h_{gs} is the coefficient of interphase heat transfer, which is a function of the Nu_s of the solid phase. According to Gunn [63],

$$h_{gs} = \frac{6k_g \alpha_s \alpha_g Nu_s}{{d_p}^2} \tag{3.14}$$

$$\begin{aligned} Nu_s = {} & (7 - 10\alpha_g + 5\alpha_g^2)(1 + 0.7Re_s^{0.2}Pr^{1/3}) \\ & + (1.33 - 2.4\alpha_g + 1.2\alpha_g^2)Re_s^{0.7}Pr^{1/3} \end{aligned} \tag{3.15}$$

Here, d_p is the diameter of particles, k_g is the thermal conductivity of gas phase fluid. Re_s and Pr are the Reynolds number of solid phase and Prandtl number of gas phase, respectively.

3.5 Radiative Hear Transfer Model

With OC particles and participating gases within FR and AR, thermal incident radiation can be absorbed and scattered while OC particles and participating gases can also emit thermal radiation.

The energy absorbed by OC particles and participating gases from the incident radiation as it passes through a path dS is

$$dI_{\lambda,a} = -\sigma_{\lambda,a} * I_\lambda dS \tag{3.16}$$

Where, I_λ is the incident radiation, S is the path length.

Similarly, the energy scattered by OC particles and participating gases from the incident radiation can be calculated by

$$dI_{\lambda,s} = -\sigma_{\lambda,s} * I_\lambda dS \tag{3.17}$$

Based on the thermal equilibrium, the energy emitted by local material is

$$dI_{\lambda,e} = \sigma_{\lambda,s} * I_{\lambda,b} dS \tag{3.18}$$

Here, $I_{\lambda,b}$ is the spectral blackbody intensity.

Besides the local thermal emission, the increase in intensity in direction (θ) contributed by in-scattering from direction (θ_i) over a path length dS can be obtained by

$$dI_{\lambda,is}(\theta, S) = \sigma_{\lambda,s} * I_\lambda(\theta_i, S) * dS * \frac{\Theta_\lambda(\theta_0)}{2} \tag{3.19}$$

Here, θ_0 is the angle between the incident and scattered beam, Θ_λ is the phase function which represents the possibility of the in-scattering from this direction and has the property of

$$\int_{-1}^{1} \Theta_\lambda(\theta_0) d\cos\theta_0 = 2 \tag{3.20}$$

Hence, the total amount increase of the intensity in direction (θ, ϕ) because of in-scattering from all direction can be expressed to be

$$dI_{\lambda,is}(\theta,S) = \sigma_{\lambda,s}\frac{dS}{2}\int_{-1}^{1} I_\lambda(\theta_i)\Theta_\lambda(\theta_i \to \theta)\, d\cos\theta_i \tag{3.21}$$

The arrow indicates from the incident to the scattered direction.

Taking $\mu = \cos\theta_i$, the equation of radiative transfer for radiation in direction θ becomes

$$\frac{\partial I_\lambda}{\partial S} = \sigma_{\lambda,a} I_{\lambda,b} - (\sigma_{\lambda,a} + \sigma_{\lambda,s}) I_\lambda + \frac{\sigma_{\lambda,s}}{2}\int_{-1}^{1} I_\lambda(\theta_i)\Theta_\lambda(\mu_i \to \mu)\, d\mu_i \tag{3.22}$$

To include the divergence of the total radiative heat flux as a source term in energy equation mentioned above, we must integrate the radiative transfer equation over all directions and all spectrum, i.e.,

$$\nabla \cdot q_r = \int_0^\infty \oint \nabla \cdot S I_\lambda d\Omega d\lambda \tag{3.23}$$

The absorption coefficient is the summation of the absorption coefficient of solid phase and gas phase.

$$\sigma_{\lambda,a} = (\sigma_{\lambda,a})_s + (\sigma_{\lambda,a})_g \tag{3.24}$$

In the region with dense solid, the impacts of gas absorption effects can be neglected if $\sigma_{\lambda,a,g}$ is much smaller than $\sigma_{\lambda,a,s}$. However, the effect of gas phase on radiation in those zones where solid is very diluted should not be neglected.

Three approaches have been developed to calculate the radiative properties of solid particles depending on the size of particles according to Kaviany [64]. The size parameter is defined to present the relative size of solid particles comparing to wavelength.

$$\alpha_R = \pi D_p / \lambda \tag{3.25}$$

The effective spectral absorption coefficient for uniformly distributed mono-size absorber can be expressed as, according to Kaviany [64],

$$\left(\sigma_{\lambda,a}\right)_s = N_a A_{\lambda,a} \tag{3.26}$$

Where, N_a is the number of the absorber per unit volume, $A_{\lambda,a}$ is the spectral absorption cross section.

$$N_a = \frac{3}{4\pi} \frac{\alpha_s}{R_p^3} \tag{3.27}$$

Here, α_s is the volume fraction of solid phase, R_p is the radius of solid particles.

$$A_{\lambda,a} = \eta_{\lambda,a} \pi R_p^2 \tag{3.28}$$

Here, $\eta_{\lambda,a}$ is the spectral absorption efficiency.

Similarly, the scattering coefficient is calculated as

$$\sigma_{\lambda,s} = \left(\sigma_{\lambda,s}\right)_s + \left(\sigma_{\lambda,s}\right)_g \tag{3.29}$$

And

$$\left(\sigma_{\lambda,s}\right)_s = N_s A_{\lambda,s} \tag{3.30}$$

In present study, $N_s = N_a$, and the spectral scattering cross section is

$$A_{\lambda,s} = \eta_{\lambda,s} \pi R_p^2 \tag{3.31}$$

Here, $\eta_{\lambda,s}$ is the spectral scattering efficiency.

For large ($\alpha_R > 20$) spheres, the spectral absorption efficiency is given by Seigel and Howell [65],

$$\eta_{\lambda,a} = 1 - \rho_\lambda \tag{3.32}$$

And

$$\eta_{\lambda,s} = \rho_\lambda \tag{3.33}$$

Since only CO2 and H2 exist in gas phase, the radiative properties of gas phase can be obtained by applying the weighted-sum-of-gray-gases model (WSGGM) [66]. According to WSGGM, the total emissivity over a path length S can be described as

$$\varepsilon = \sum_{i=0}^{I} a_{\varepsilon,i}(T)(1 - e^{-\kappa_i pS}) \tag{3.34}$$

Here, κ_i is the absorption coefficient, while $a_{\varepsilon,i}(T)$ is the factor of emissivity weighting for i^{th} gray gas, and can be approximated as

$$a_{\varepsilon,i}(T) = \sum_{j=1}^{J} b_{\varepsilon,i,j} T^{j-1} \tag{3.35}$$

κ_i and $b_{\varepsilon,i,j}$ can be obtained by laboratory data [67]–[69].

To account for windows in the spectrum between spectral regions of high absorption, the first absorption coefficient $\kappa_0 = 0$, and the first weighting factor is gained from

$$a_{\varepsilon,0}(T) = 1 - \sum_{i=1}^{I} a_{\varepsilon,i}(T) \tag{3.36}$$

The absorption coefficient needs to be rescaled if the total static gas pressure is not equal to 1 atm.

$$\kappa_i \rightarrow \kappa_i p^m \tag{3.37}$$

Here, m is a non-dimensional value, can be obtained from [70].

For the cases have thick optical path and small difference between gas temperature and wall temperature, we can assume that

$$(\sigma_a)_g = \varepsilon \tag{3.38}$$

The effects of scattering caused by gas on radiative heat transfer are neglected in present study.

3.6 Kinetic Theory of Granular Flow

To solve the conservation equations of momentum for solid phase, the granular shear viscosity μ_s, granular pressure P_s, and bulk viscosity λ_s of solid phase need to be specified.

Due to the collision of granules inside the fluidized bed, a random granular motion occurs and is described by Kinetic theory of granular flow [71]

$$\begin{aligned}\frac{\partial}{\partial t}(\alpha_s\rho_s\Theta_s) + \nabla\cdot(\alpha_s\rho_s\Theta_s v_s) \\ = -\frac{2}{3}(P_s + \alpha_s\tau_s)\colon\nabla v_s + \nabla\cdot(k_s\nabla\Theta_s) - \gamma - 3K_{gs}\Theta_s\end{aligned} \tag{3.39}$$

Here, P_s is the solid pressure and Θ_s is the granular temperature which is defined as

$$\Theta_s = \frac{1}{3}\langle v_s' v_s' \rangle \tag{3.40}$$

Where, v_s' is the fluctuating velocity of solid particles.

The solid pressure P_s is also a function of Θ_s. According to Lun et al. [72], P_s can be expressed as

$$P_s = \alpha_s \rho_s \Theta_s + 2(1 + e_{ss})\alpha_s^2 g_0 \rho_s \Theta_s \tag{3.41}$$

Where, e_{ss} is the coefficient of restitution for particle collisions, usually take $e_{ss} = 0.9$. g_0 is the radial distribution function which is defined as bellow for one solids phase [73].

$$g_0 = \left[1 - \left(\frac{\alpha_s}{\alpha_{s,max}}\right)^{1/3}\right]^{-1} \tag{3.42}$$

Here, $\alpha_{s,max}$ is the packing limit for granules.

k_s is the diffusion coefficient for granular energy. According to Lun et al.[72], k_s and can be written as

$$\begin{aligned} k_s = \frac{15\rho_s d_s \alpha_s \sqrt{\Theta_s \pi}}{4(41 - 33\eta)} \Bigg[1 \\ + \left(\frac{12}{5}\eta(4\eta - 3) + \frac{16}{15\pi}\alpha_s g_0 \eta(41 - 33\eta)\right)\Bigg] \\ + \frac{25\rho_s d_s \alpha_s \sqrt{\Theta_s \pi}}{16 g_0 \eta(41 - 33\eta)}\left[1 + \frac{12}{5}\eta^2(4\eta - 3)\alpha_s g_0\right] \end{aligned} \tag{3.43}$$

With $\eta = 0.5(1 + e_{ss})$.

Due to the collisions between particles, the energy of the particles dissipates with the rate of γ which is represented by Lun et al. [72].

$$\gamma = \frac{12(1 - e_{ss}^2)g_0}{d_s\sqrt{\pi}} \rho_s \alpha_s^2 \Theta_s^{3/2} \tag{3.44}$$

As mentioned above, K_{gs} is the interphase exchange coefficient which represents the intensity of drag force between gas and solid phase. It can be defined by

$$K_{gs} = \frac{\rho_s \alpha_s f}{t_r} \tag{3.45}$$

Where, t_r is the particulate relaxation time and defined as

$$t_r = \frac{\rho_s d_s^2}{18\mu_g} \tag{3.46}$$

And f is defined differently by different models. However, all definitions of f include a drag function C_D.

According to the Gidaspow et al. [62], the interphase exchange coefficient in a solid-gas multiphase flow can be defined for different α_g range.

When $\alpha_g > 0.8$,

$$K_{gs} = \frac{3}{4} C_D \frac{\alpha_s \alpha_g \rho_g |v_s - v_g|}{d_s} \alpha_g^{-2.65} \tag{3.47}$$

Where,

$$C_D = \frac{24}{\alpha_g Re_s}\left[1 + 0.15\left(\alpha_g Re_s\right)^{0.687}\right] \tag{3.48}$$

$$Re_s = \frac{\rho_g d_s \left|v_s - v_g\right|}{\mu_g} \tag{3.49}$$

When $\alpha_g < 0.8$,

$$K_{gs} = 150\frac{\alpha_s\left(1 - \alpha_g\right)\mu_g}{\alpha_g d_s^2} + 1.75\frac{\rho_g \alpha_s \left|v_s - v_g\right|}{d_s} \tag{3.50}$$

The shear stress tensor of solid particles is contributed by the effects of friction (modeled by Schaeffer [74]), and the effects of collisions and particle motion (modeled by Ding and Gidaspow [26]).

$$\mu_s = \mu_{s,fr} + \mu_{s,col} + \mu_{s,kin} \tag{3.51}$$

With

$$\mu_{s,fr} = \frac{P_s sin\xi}{2\sqrt{I_{2D}}} \tag{3.52}$$

$$\mu_{s,col} = \frac{10\rho_s d_s\sqrt{\Theta_s \pi}}{96\alpha_s g_0(1 + e_{ss})}\left[1 + \frac{5}{4}\alpha_s g_0(1 + e_{ss})\right]^2 \tag{3.53}$$

$$\mu_{s,kin} = \frac{5}{4}\alpha_s g_0 \rho_s d_p(1 + e_{ss})\sqrt{\frac{\Theta_s}{\pi}} \tag{3.54}$$

Here, ξ is the internal friction angle, and usually $\xi = 30°$. I_{2D} is the second invariant of the deviatoric stress tensor.

The solid phase bulk viscosity λ_s is given by Lun et al. [72]

$$\lambda_s = \frac{4}{3}\alpha_s g_0 \rho_s d_p (1 + e_{ss}) \sqrt{\frac{\Theta_s}{\pi}} \tag{3.55}$$

3.7 Species Transport Equations

The transport equation for mass fraction of i in phase j $Y_{j,i}$ is given as

$$\frac{\partial}{\partial t}\left(\alpha_j \rho_j Y_{j,i}\right) + \nabla \cdot \left(\alpha_j \rho_j v_j Y_{j,i}\right) = -\nabla \cdot \left(\alpha_j J_{j,i}\right) + r_i \tag{3.56}$$

Where, $J_{j,i}$ is the diffusion flux of species i in in phase j. The mass diffusion coefficients are used to calculate the diffusion flux in turbulent flow using modified Fick's law.

$$J_{j,i} = -\left(\rho D_{i,m} + \frac{\mu_t}{Sc_t}\right) \nabla Y_{j,i} \tag{3.57}$$

Here $D_{i,m}$ is the diffusion coefficient of the mixture.

And r_i is the rate of product of species i by chemical reaction.

3.8 Kinetic Models for Chemical Reactions

The shrinking core model (SCM) is one of the widely-used models to describe the heterogeneous chemical reactions, which are the chemical reactions between solid particles and gas phase in the field of coal gasification, medicine production, food production, CLC, and so on.

Five steps are considered in SCM. Step 1, the gaseous reactant diffuses through the gas film from the bulk gas phase to the surface of solid particle. Step 2, the gaseous reactant diffuses through the porous ash layer and reaches the surface unreacted core of solid particles. The porous ash layer is the layer formed by the product of solid particles. Step 3, the gaseous reactant reacts with the unreacted core on the surface of solid particle. During this step, gaseous reactant and the unreacted core of solid particle are consumed while gaseous product and porous ash medium are produced. Step 4, the gaseous product diffuses through the porous layer of solid particle and reaches the surface of solid particle. Step 5, the gaseous product further diffuses through the film layer of gas phase. The five steps of SCM are presented in Figure 5.

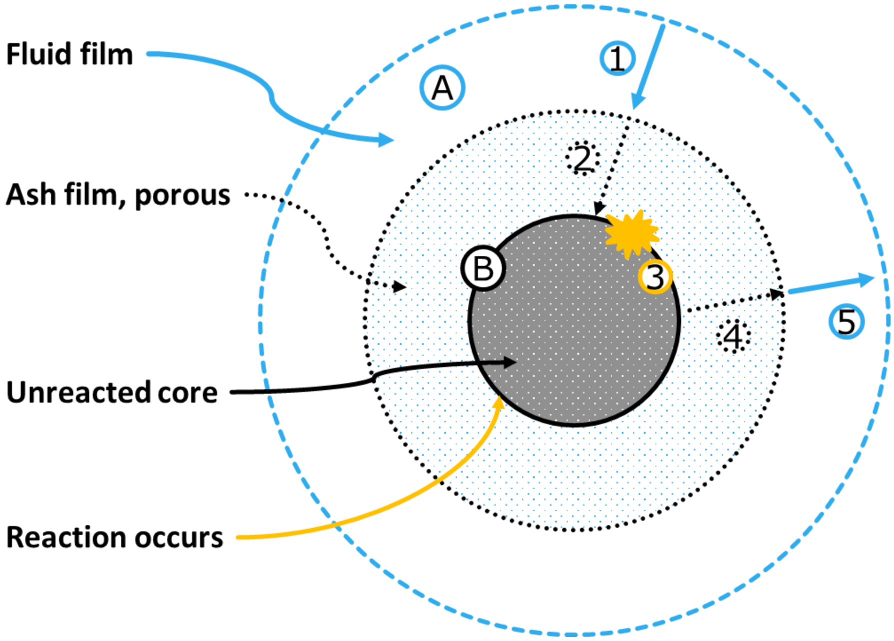

Figure 5 Schematic of shrinking core model.

According to Kruggel-Emden et al. [18], the conversion rate of OC derived by linear shrinking core model can be expressed as

$$\frac{dZ_s}{dt} = bke^{-E/RT}C_g^n \tag{3.58}$$

Here, $Z_s = \left(C_{s,o,0} - C_{s,o}\right)/C_{s,o,0}$, is the conversion degree of oxidized OC in fuel reactor. Here, $C_{s,o,0}$ is the initial molar concentration of oxidized OC. Similarly, $Z_s = \left(C_{s,r,0} - C_{s,r}\right)/C_{s,r,0}$ is the conversion of reduced OC in air reactor. C_g is the concentration of gaseous reactant.

Meanwhile, b is the stoichiometric constant for OC in reduction and oxidization reactions; k is the apparent constant for chemical reaction; E is the activation energy.

Or, according to Kruggel-Emden et al. [18] the conversion rate of OC can be given by spherical SCM, as

$$\frac{dZ_s}{dt} = 3bke^{-E/RT}C_g^n(1 - Z_s)^{2/3} \tag{3.59}$$

With the rate of conversion of OC, the heterogeneous reaction rate can be obtained by

$$R_{he} = \frac{1}{b}C_{oc}\frac{dZ_s}{dt} \tag{3.60}$$

Where, C_{oc} is the molar concentration of OC in reactors.

Zafar et al. [58] determine the kinetic parameters of SCM for both oxidation and reduction reactions using NiO/MgAl2O4 as the OC and CH_4 as the fuel. Meanwhile, the SCM was also applied to model the reaction kinetic between Mn3O4 and CH_4 by Zafar et al. [57].

Besides the SCM model mentioned above, the nucleation and nuclei growth model (NNGM) is also used to model the kinetics of heterogeneous chemical reaction. This model begins with the dissociation of gaseous reactant. Then the metal-oxygen bond breaks, releasing mental atoms or reduced form metal oxides and oxygen ions. The dissociated gaseous reactant and oxygen ions then produce CO_2 and H_2O. Once be released, mental atoms or reduced form metal oxides diffuse away and gather together to form clusters. These clusters will further form metal crystallites or metal oxide crystallites as the reaction proceeds.

According to the mechanism of this model, the initial reaction rate is slow. However, once more crystallites are formed, the dissociation of gaseous reactant is performed effectively by the crystallites, and consequently, the reaction performs with a higher rate.

According to Kelly et al. [75], the conversion rate of OC can be expressed as

$$\frac{dZ_s}{dt} = nke^{-\frac{E}{R}\left(\frac{1}{T}-\frac{1}{T_m}\right)}(1-Z_s)[-ln(1-Z_s)]^{(1-n)/n}\left(1-Z_g\right) \tag{3.61}$$

Here, Z_g is the conversion of gas.

It is worth noting that, take an initial of $Z_s = 0$, with $n \neq 1$, the conversion rate $\frac{dZ_s}{dt} = 0$. The chemical reaction does not occur. According to the mechanism, with zero crystallites presenting in the solid phase, the chemical reaction is very slow, and hence numerically $\frac{dZ_s}{dt} = 0$. Hence, when performing numerical simulation, the initial value of Z_s should be greater than 0.

Based on Kim et al.'s work [15], the reduction reaction of $CaSO_4$ with H_2 is first order with respect to H_2, and K_i is a function of reaction temperature. The conversion of $CaSO_4$ has the expression of

$$\left[-ln\left(1-Z_{CaSO_4}\right)\right]^{1/1.16}=4300P_{H_2}e^{-\frac{151000}{RT}}t \tag{3.62}$$

Where, P_{H_2} is the partial pressure of H_2. The rate of conversion can also be obtained as

$$\frac{dZ_{CaSO_4}}{dt}=4988P_{H_2}e^{-\frac{151000}{RT}}\left[-ln\left(1-Z_{CaSO_4}\right)\right]^{0.138}\left(1-Z_{CaSO_4}\right) \tag{3.63}$$

3.9 Minimum Fluidization Velocity

As an important parameter determines the fluidization pattern within reactors, researchers have proposed various models to predict the minimum fluidization velocity (MFV) for the fluidized bed [76].

According to Pattipati et al. [77], the minimum fluidization velocity can be obtained from

$$Re_{mf}=(33.7^2+0.0408Ar)^{1/2}-33.7 \tag{3.64}$$

Where, Re_{mf} and Ar are Reynolds number with minimum fluidization velocity and the Archemedes number, respectively. And the Archemedes number is

$$Ar=\frac{{d_p}^3\rho\left(\rho_p-\rho\right)g}{\mu^2} \tag{3.65}$$

Here, ρ_p and g are the density of the particles and gravitational acceleration.

$$Re_{mf}=\frac{U_{mf}d_p\rho}{\mu} \tag{3.66}$$

Here, U_{mf} is the minimum fluidization velocity, d_p is the diameter of the solid particles while ρ and μ are the density and viscosity of gas respectively. From the expressions listed above, we can conclude qualitatively that the MFV is mainly determined by the size of solid particles, density of grains and the viscosity of gas phase.

CHAPTER 4

STUDY OF FUEL REACTOR

4.1 Numerical Models

4.1.1 Materials and Geometry

In this study, gaseous hydrogen (H2) and calcium sulfate (CaSO4) are considered as the fuel and oxygen carrier (OC), respectively. The gaseous product is water vapor (H_2O) while the solid product is Calcium sulfide (CaS).

The reduction chemical reaction in the fuel reactor using H_2 as fuel and $CaSO_4$ as oxygen carrier can be written as

$$CaSO_4 + 4H_2 = CaS + 4H_2O \qquad \Delta H = -6.4kJ/mol(CaSO_4) \tag{4.1}$$

Evidentially, this reduction chemical reaction is a slightly exothermic reaction.

Helium is used as the initial gas in this study, though Deng et al. [16] and Harichandan and Shamim [17] initialized the gas phase of the fuel reactor with H_2. The main properties of the materials are shown in Table 3.

Table 3 Properties of materials used in FR study.

Property	H_2	H_2O	He	$CaSO_4$	CaS
Density of (kg/m3)	0.0819	0.554	0.163	2960	2800
Thermal Conductivity (w/m-k)	0.167	0.0261	0.152	0.32	0.0454
Viscosity (kg/m-s)	8.41e-6	1.34e-5	1.99e-5	1.72e-5	1.72e-5
Particle diameter (mm)				0.275	0.275

Figure 6 shows the geometry and mesh for the fuel reactor, which has a width of 0.4m and a height of 1.0m. The fuel reactor consists of 2 regions. The static bed region with a height of 0.4m is filled by OC particles with the initial volume fraction $\alpha_{s,0} = 0.48$. The free bed region above the static bed region has the height of 0.6m. Besides the OC on the static bed region, the fuel reactor is fully filled by gas. The space size for meshing is 10mm for the width and height.

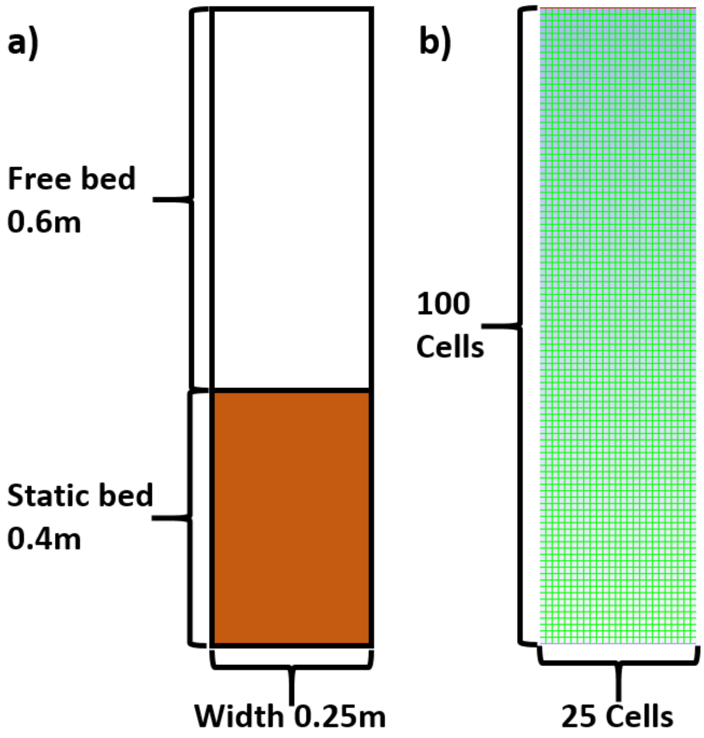

Figure 6 a) Geometry, and b) mesh of fuel reactor.

4.1.2 Numerical Methods

The commercial CFD software code Fluent are used to solve the differential equations and chemical reactions mentioned above using a finite volume method. The phase-coupled SIMPLE scheme is applied for the pressure-velocity coupling. The Second order upwind is used for partial equations' spatial discretization. An absolute criterion of 1e-5 is used to check the convergence for all equations in every time step iteration. The standard dispersed $k - \varepsilon$ turbulent multiphase model is used. The restitution coefficient e_{ss} is set to 0.9. Table 4 lists the main parameters and models used in this study.

Table 4 Numerical methods and models used by FR modeling.

Numerical Method	Model or value	Numerical Method	Model or value

Multiphase model	Eulerian-Eulerian	Drag coefficient	Gidaspow [27]
Turbulent model	Dispersed standard k-e	Granular conductivity	Gidaspow [27]
Granular viscosity	Gidaspow [27]	Solids pressure	Lun et al. [30]
Granular Bulk Viscosity	Lun et al. [30]	Radial Distribution	Lun et al. [30]
Friction viscosity	Schaeffer [32]	Heat transfer coefficient	Gunn [28]
Angle of internal friction	30°	Restitution coefficient	0.9
Packing Limit	0.6		
Pressure-velocity coupling	Phase coupled SIMPLE	Spatial discretization	2nd order upwind

4.1.3 Boundary and Initial Conditions

The velocity-inlet BC is considered as the boundary condition for the bottom surface while pressure outlet BC for the top surface. Both left and right walls are considered at a constant temperature and no-slip condition for both gas and granule phases.

Initial results indicate that both water vapor and H_2 are the dominant gases in the fuel bed, Hence, the average value of the viscosities of water vapor and H_2 are considered as the viscosity of gas phase. Taking calcium sulfate as the oxygen-carrier and diameter of OC particles as $d_p = 0.275mm$, the minimum fluidization velocity can be calculated as

$$U_{mf} = 0.117(m/s) \tag{4.2}$$

In order to utilize the fuel reactor as a bubbling bed, a larger feeding velocity of gas should be used, usually 2~7 times as U_{mf} [16]–[18]. For the base case in this study, a velocity of $3U_{mf} = 0.35m/s$ on the inlet is used for feeding gas.

As mentioned above, both shrinking core model [43], [57], [58] and nucleation and nuclei growth model [15] [75] are used to perform the experimental data analysis for OC. Since the experimental data for $CaSO_4$ reacting with H_2 is analyzed by the nucleation and growth model [15], the heterogeneous chemical reaction rate is determined by Eq.(3.63). However, the SCM of chemical reaction rate (Eq.(3.59)) is also been used to validate the present results with results by Deng et al.[16] and Harichandan and Shamim [17]. From a numerical study point of view, the concentration of reduced form OC should be set to an initial value larger than 0 to activate the chemical reaction. As Deng et al. [16] and Harichandan and Shamim [17] conducted their study using pure $CaSO_4$, the mass fraction of CaS in validation case has a small value of 0.001. However, from a particle point of view, it is hard to oxidized CaS into $CaSO_4$ entirely [18], [78], [79], hence, the molar fraction of CaS in solid phase is set to 0.2 for the base case of this study. The boundary conditions and initial conditions used in the base case is shown in Table 5.

Table 5 Boundary and initial conditions used for FR study base case.

BC	Value	IC	Value
Inlet BC type	Velocity inlet	Initial gas	He
Superficial velocity of feeding gas	0.35m/s	Initial temperature of gas	1123K
Feeding gas temperature	300K	Initial temperature of solid	1123K

Outlet BC type	Pressure outlet	Initial mole fraction of CaS	0.2
Outlet pressure	0 gauge Pa	Initial volume fraction of solid	0.4
Walls	Constant temperature, 1123K		

4.2 Validations and Independence Checking

Figure 7 presents a comparison of the mole fraction of H_2 on the outlet between present work and the results of Harichandan and Shamim [17].

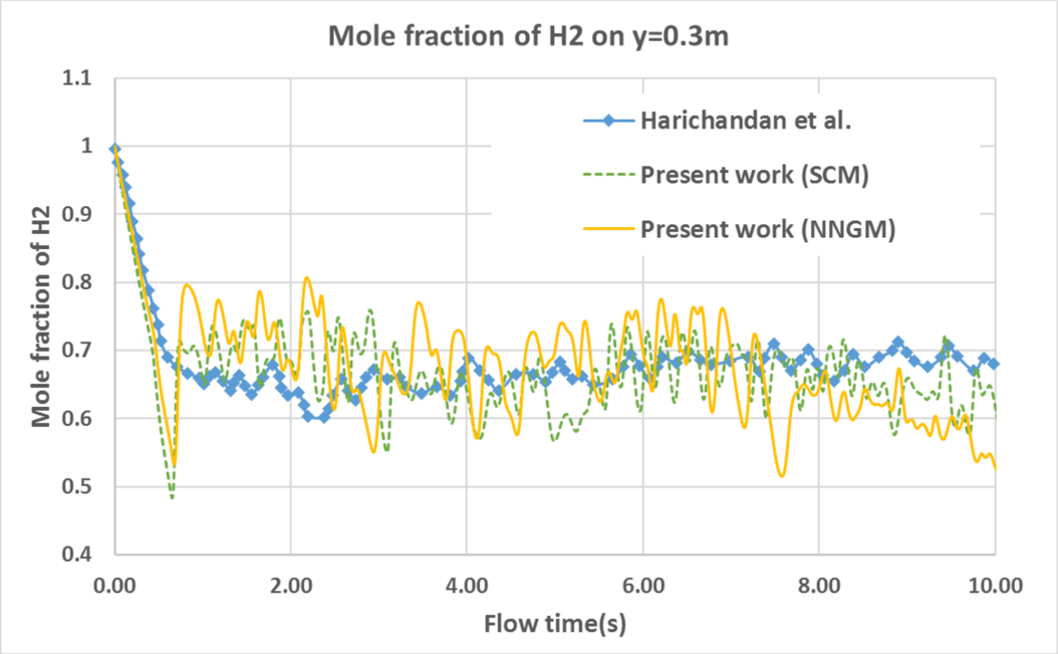

Figure 7 Mole fraction of H_2 on the outlet by recent study and Harichandan and Shamim [17].

Both the shrinking core model and nucleation and nuclei growth model are applied to model the chemical reaction. Figure 7 depicts the comparison between present work using both shrinking core model and nucleation and nuclei growth model and results by Harichandan and Shamim [17]. Relative good agreements have been obtained between published work and present work. However, results with shrinking core model have better fitting with published data.

To check the time independence of this modeling, the time step of 4 values (i.e. 0.2ms, 0.5ms, 0.8ms, 1.0ms) are checked, and the results are shown in Figure 8.

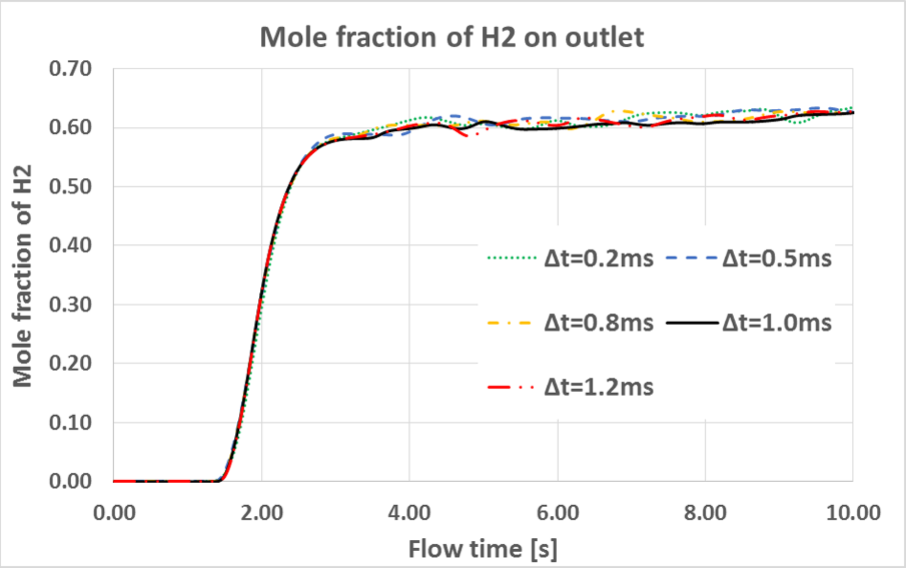

Figure 8 Mole fraction of H_2 on outlet as a function of time with different time steps.

We can see from Figure 8 that the values of simulation time step have negligible effects on the result. From both the accuracy and efficiency point of view, the time step of 1.0mm is selected to run the simulations onwards.

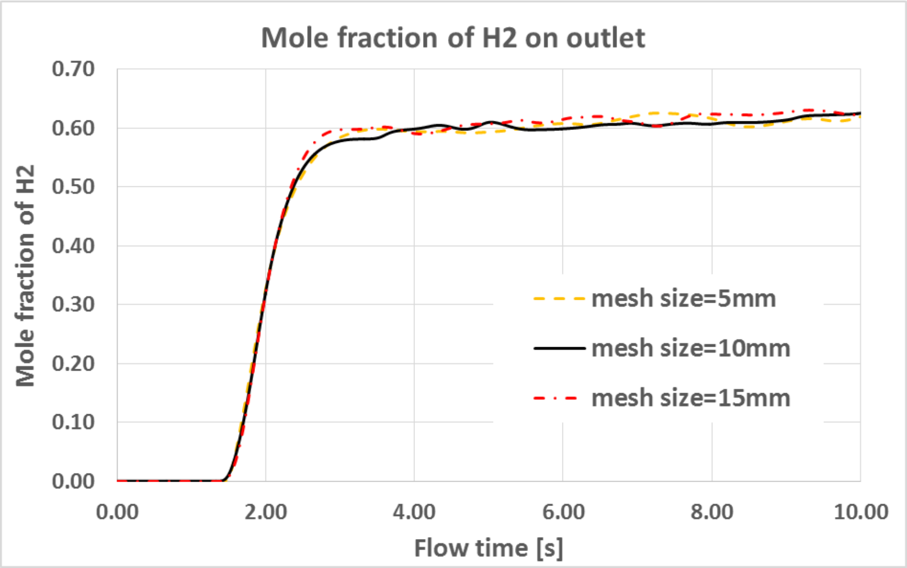

Figure 9 Mole fraction of H_2 on outlet as a function of time with different grid sizes.

Independence checking with grid size also shows that mesh size between 5mm and 15mm have very limited effects on present work. Thun, mesh size equals to 10mm is selected.

4.3 Discussions of Base Case

With the parameters presented above, we can learn the numerical results of the base case. The volume fraction of oxygen carrier particles from time 0.0s to 1.0s is depicted in Figure 10.

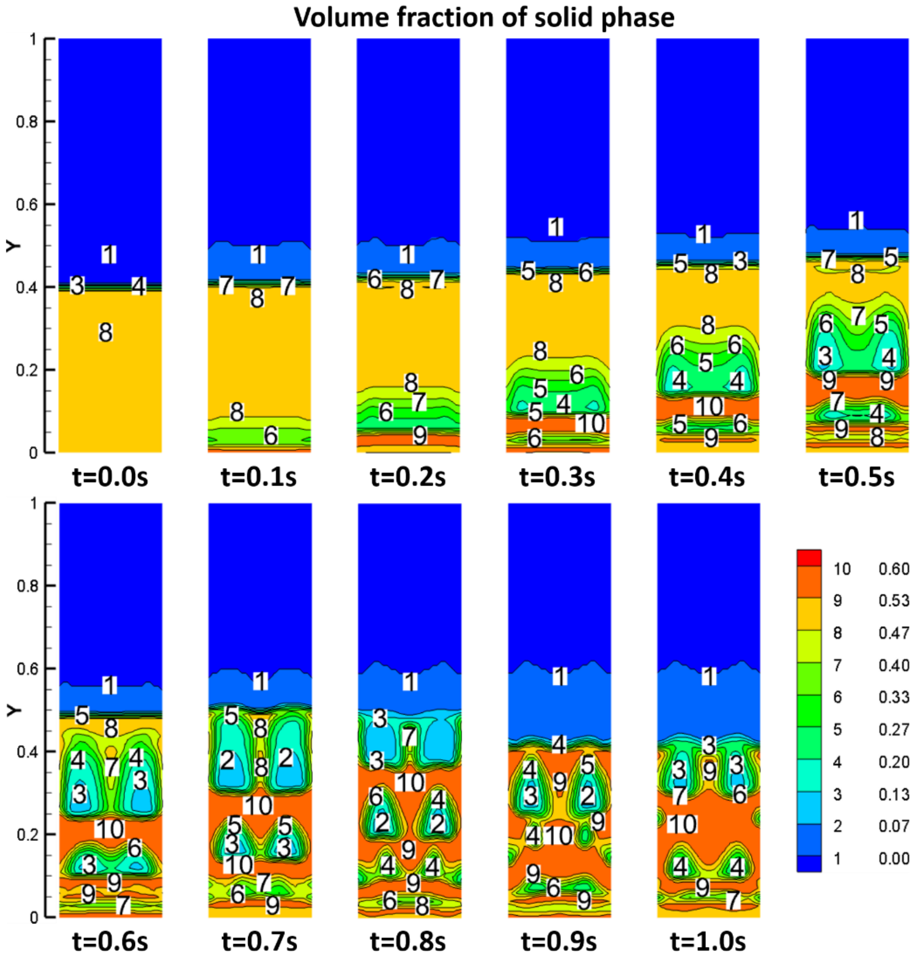

Figure 10 Volume fraction of oxygen carriers between 0.0s and 1.0s.

Since the initial volume fraction of the solid phase (i.e. 0.48) is smaller than the packing limit (i.e. 0.6), the oxygen carrier granules are slightly compressed by the gravity at the beginning of the whole process. After the gas phase is fed from the bottom of the fuel reactor, small bubbles emerge and rise. Then, small bubbles mix with other small bubbles and become bigger ones. Those bigger bubbles keep rising and mix with other small bubbles around and form large bubbles. Solid particles are raised by the rising large bubbles, which will burst when arrived the top of the static bed. After the bursting of the large bubbles, the solid particles collapse and fall back into the static bed. It is important to note that after the first few (usually two) large bubbles burst, the quasi-steady state is obtained.

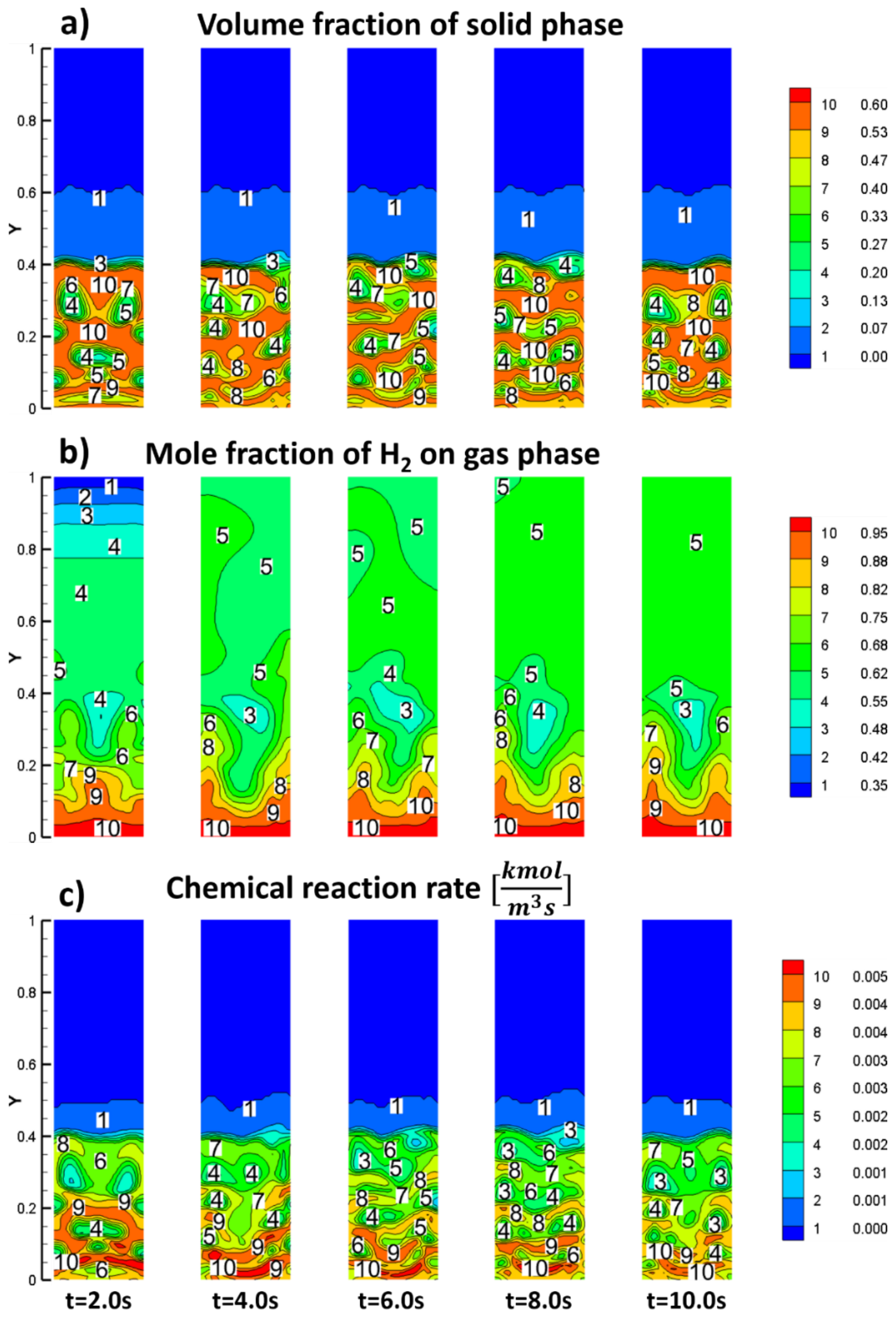

Figure 11 Comparison between contours of a) solid volume fraction, b) mole fraction of H_2, and c) heterogeneous reaction rate at t=2.0s, 4.0s, 6.0s, 8.0s, and 10.0s.

The comparison between volume fraction of solid, mole fraction of H_2, and heterogeneous reaction rate at t=2.0s, 4.0s, 6.0s, 8.0s, and 10.0s is shown in Figure 11. As we can see from

Figure 10 and a) of Figure 11, the distributions of solid particles are almost symmetric along the center line up to 2.0s. However, the fuel reactor becomes chaotic and the distribution of solid particles become asymmetric after t=4.0s.

As H_2 fuel is fed from the bottom of FR and the reacts with $CaSO_4$ as it rises, the highest value of mole fraction of H_2 is observed at the bottom of the FR close to the inlet while the lowest value at the top close to the exit of gases. The distributions of H_2 on the free bed (i.e. the region higher than 0.4m of the reactor) are nearly uniform. Meanwhile, less H_2 is found in the center than the two sides at every specific height. It enlightens us that more fuel “leaks” through the regions beside the two walls than the center zone.

The heterogeneous reaction rate on the bottom area of the reactor is faster than on the higher region. By comparing a) and c) of Figure 11, it is reasonable to conclude that, generally, the heterogeneous chemical reaction rate is higher in the zones on where more particles concentrate.

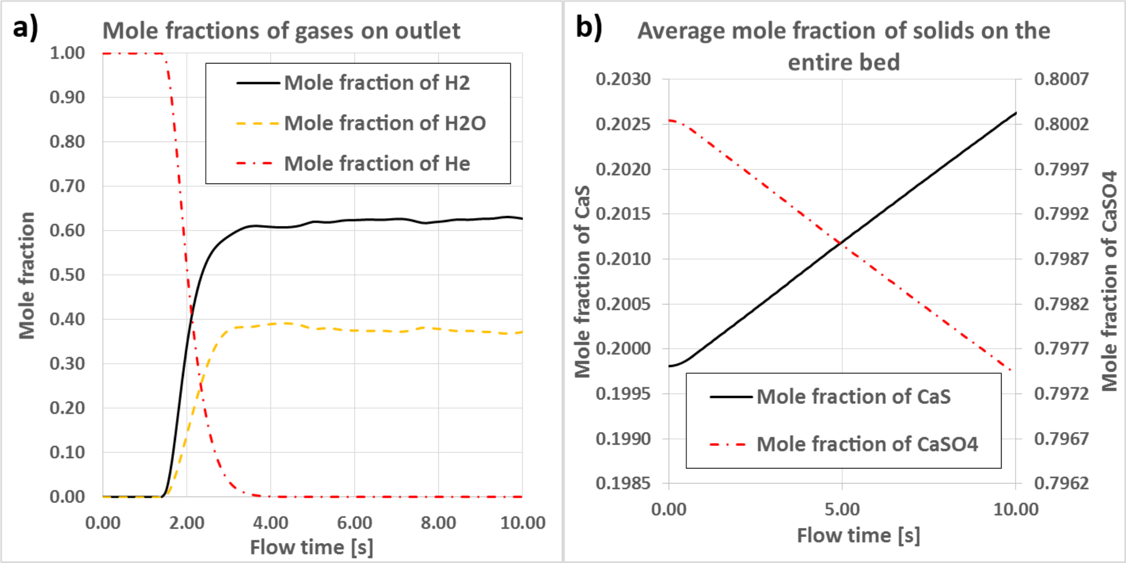

Figure 12 Mole fraction of a) gases on the outlet, and b) solids on entire bed.

Mole fractions of gases on the outlet and mole fraction of solids versus time are illustrated in Figure 12. From t=0.0s to t=1.5s, only helium can be observed on the outlet of FR since the whole bed is initially full filled by helium for the gas phase. He is continually swept by H_2 and H_2O vapor and then eliminated at t=3.5s onwards. However, the mole fraction of H_2 and H_2O vapor, which are pushed by feeding H_2 and generated by chemical reaction, respectively, increase rapidly between t=1.5s and t=3.5s, on the outlet. Then the mole fraction of H_2 and H_2O fluctuate at the values around 0.61 and 0.39, respectively. As mentioned above, the gas-solid multiphase flow within the FR reaches the quasi-steady condition after t=1.0s. However, according to the distribution of gases on the outlet, the FR system does not get quasi-steady until t=4.0s.

The mole fraction of CaS increases while the mole fraction of $CaSO_4$ decreases as the reaction proceeds. However, the changes are nearly negligible because the mole fraction increases by only 1.4% for CaS and decreases by only 0.34% for $CaSO_4$.

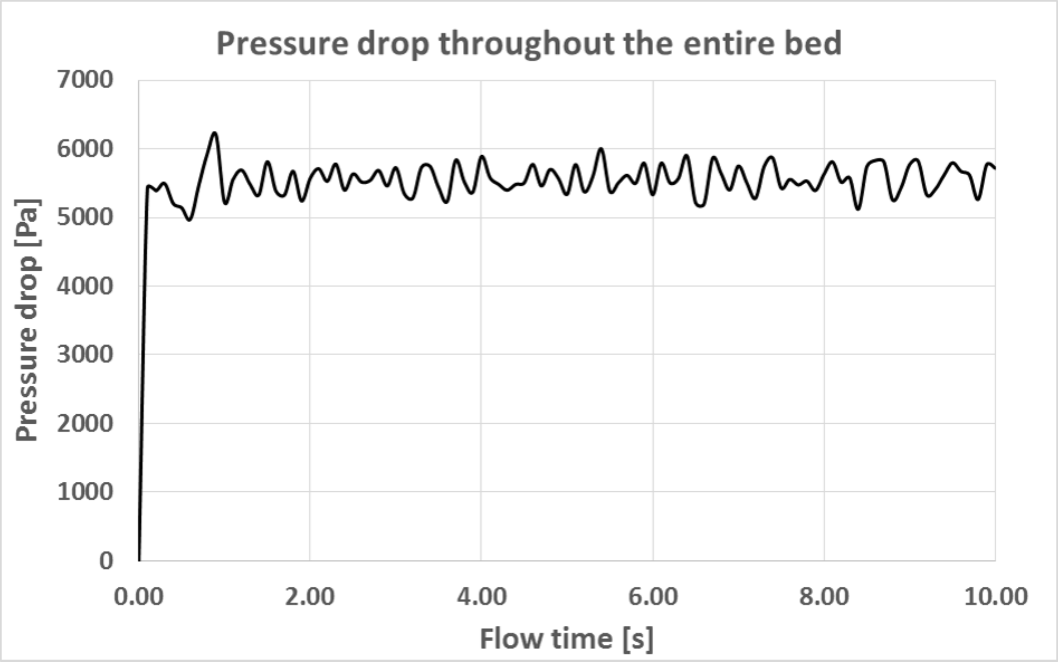

Figure 13 Pressure drop throughout the entire bed as a function of flow time.

Figure 13 demonstrates the pressure drop from the bottom to the top of FR. Differs from the distributions of gases, pressure drop achieves its quasi-steady state almost immediately and fluctuates around a value of 5.6kPa within the range of [-400Pa, +500Pa] as the fuel being fed from the bottom. Meanwhile, the first two waves of the plot are the largest two among all the fluctuation waves. Compared to the operating pressure (1atm), the fluctuation of pressure drop is negligible.

4.4 Effects of Mole Fraction of CaS in Solid Phase

As mentioned above, from the numerical study and practical application points of view, the initial mole fraction of CaS in solid phase is set to 0.2 for base case. The effects of initial mole fraction of $CaSO_4$ (i.e. 0.70, 0.75, 0.80, 0.85, 0.90) on the mole fraction of H_2 on the outlet are studied in this section.

With the largest simulation time t=10s, superficial gas feeding velocity 0.35m/s, the conversion of $CaSO_4$ throughout this simulation can be calculated by

$$dZ_{CaSO_4} = \frac{\dot{m}_{H_2}\left(1-\eta_{H_2,O}\right) * 4 * T}{MW_{H_2} C_{CaSO_4,m,0}} \tag{4.3}$$

Where, $\dot{m}_{H_2}$ is the mass flow rate of feeding hydrogen, $\eta_{H_2,O}$ is the mole fraction of H_2 on the outlet, $T = 10s$ is the largest simulation time, MW_{H_2} is the molar weight of H_2, $C_{CaSO_4,m,0}$ is the initial molar concentration of $CaSO_4$.

Among all the setups mentioned above, the greatest dZ_{CaSO_4} is calculated to be $dZ_{CaSO_4} =$ 0.7%. Hence, it is reasonable to neglect conversion of $CaSO_4$ during the simulation of this study, but focus more on the initial mole fraction of $CaSO_4$.

The effects of mole fraction of $CaSO_4$ on the fuel conversion performance are plotted in Figure 14.

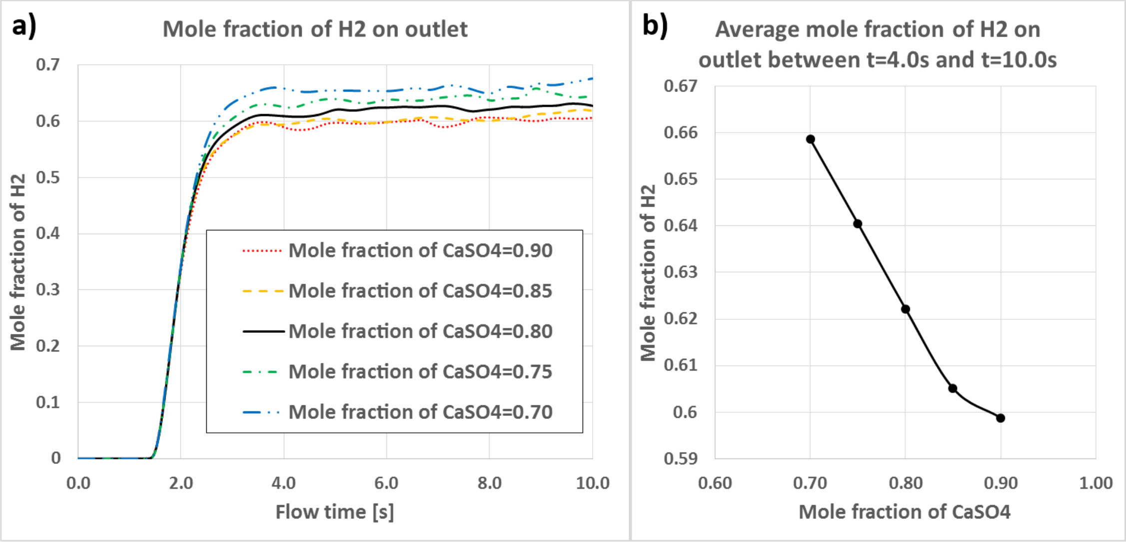

Figure 14 Plots of a) mole fraction of H_2 on outlet vs. time, and b) average mole fraction of H_2 on outlet between t=4.0s and t=10.0s v.s. the mole fraction of $CaSO_4$.

Cases with different values of mole fractions of $CaSO_4$ on the bed perform very like the base case except for the quasi-steady (flow time larger than 4.0s) where values of mole fraction of H_2 on the outlet increase with low values of $CaSO_4$ mole fractions. By plotting the average mole fraction of H_2 on outlet between t=4.0s and t=10.0s as a function of mole fraction of $CaSO_4$ (b) of Figure 14), we can see clearly that the conversion of H_2 increases linearly with a mole fraction of $CaSO_4$ less than 0.85. However, the effects of mole fraction of $CaSO_4$ decay with values larger than 0.85.

4.5 Effects of Operating Temperature

As one of the most important parameters for CLC systems, operating temperature need to be well studied for system design [78]. The effects of operating temperature are discussed in this section.

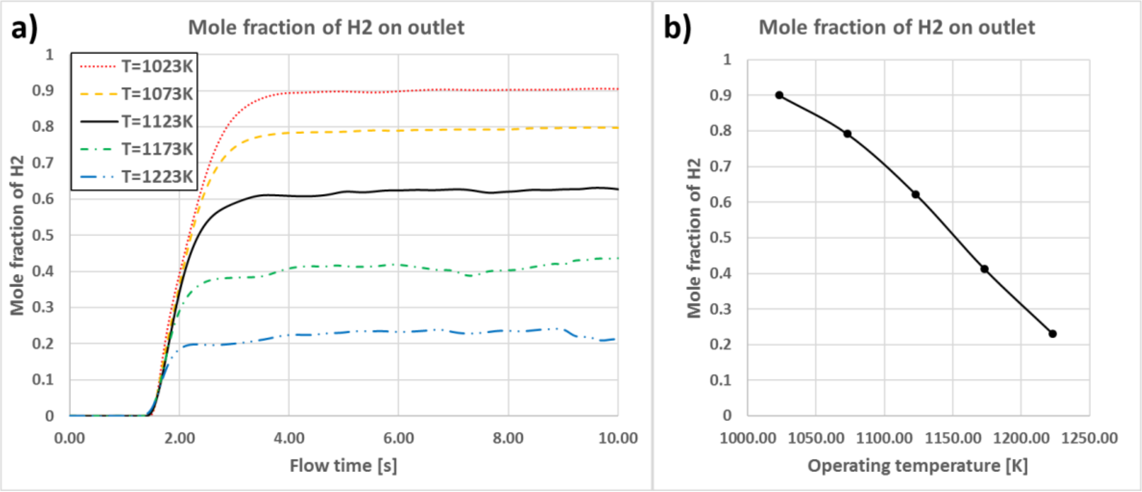

Figure 15 Plots of a) mole fraction of H_2 on outlet vs. flow time, and b) average mole fraction of H_2 on outlet between t=4.0s and t=10.0s v.s. operating temperature.

Since the chemical reaction rate has a positive correlation with the temperature, higher operating temperature results in higher chemical reaction rate, hence lower fuel is detected on the outlet. Moreover, faster chemical reaction rate accelerates the system to obtain the quasi-steady state. As shown in Figure 15 a), the system operating at a temperature of 1223K gains the quasi-steady state at t=2.0s while the one reaches its quasi-steady state at t=4.0 with operating temperature T=1023K. Plotting the average mole fraction of H_2 on the outlet after the quasi-steady state as a function of operating temperature illustrates the effect of operating temperature more clearly. As presented in Figure 15 b), the operating temperature has a significant effect on the chemical reaction. The average mole fraction of H_2 on the outlet after quasi-steady state reduces dramatically and almost linearly from 0.90 to 0.22 as the operating temperature rises from 1023K to 1223K.

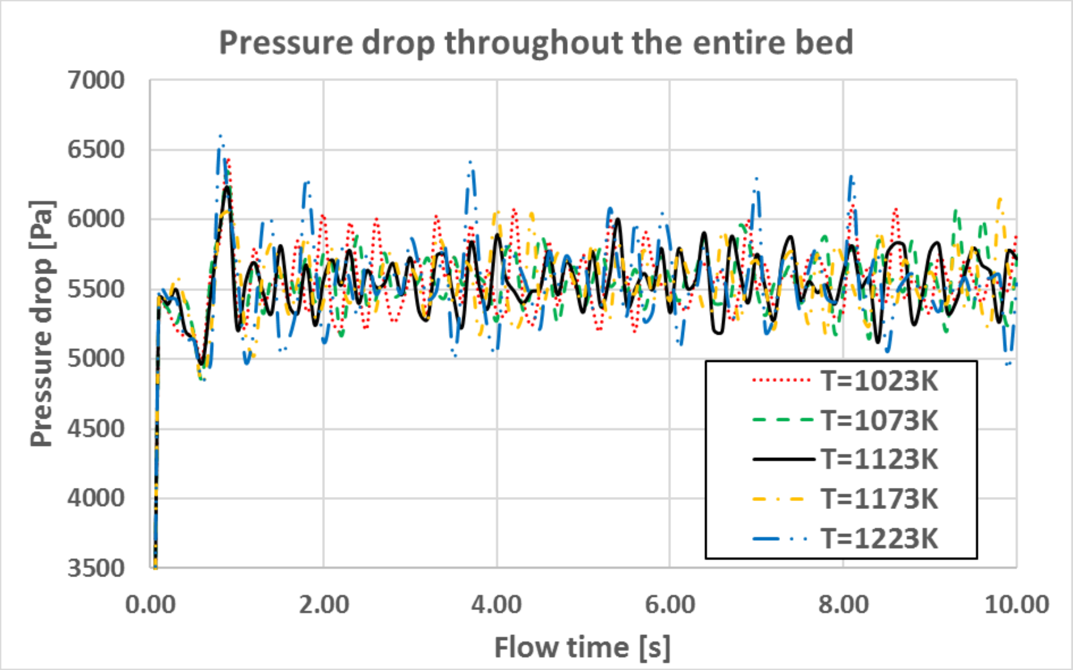

Figure 16 Pressure drop of the bed as a function of flow time with different operating temperatures.

The pressure drop of the bed versus flow time under different operating temperature is shown in Figure 16. This chart indicates the fact that the operating temperature has only tiny effects on the flow, although the fluctuation range of pressure drop under 1223K is slightly larger.

4.6 Effects of Superficial Feeding Velocity of Gas

As mentioned above, the superficial feeding velocity (SFV) of gaseous fuel affects the capacity of the entire system significantly. The effects of SFV in terms of minimum fluidization velocity (MFV) are studied in this section.

Figure 17 indicates the contours of the volume fraction of the solid particles with different values of the SFV of gaseous fuel.

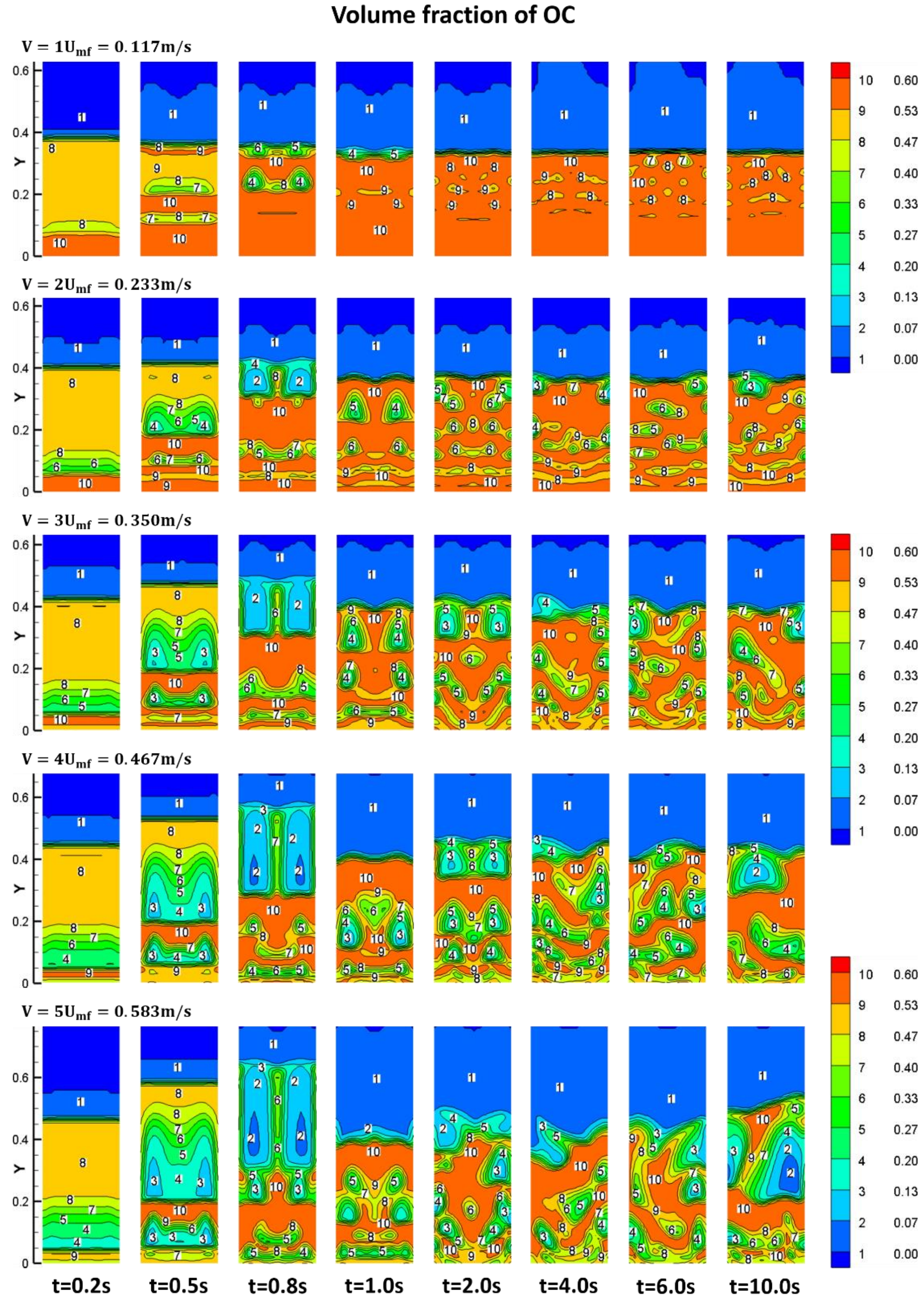

Figure 17 Volume fraction of solid phase with different superficial feeding velocity of gas. Note that only the lower sections of FR contain solid particles are shown.

It is obvious that more OC granules can rise to a higher position with larger gas-phase feeding velocity. Larger bubbles emerge and the distribution of the bubbles becomes less uniform and less symmetric in the bed with larger gas-velocity. With $v \leq 2U_{mf}$, the distribution of bubbles with static bed region is nearly uniform, while the flow conditions are more chaotic and the non-uniformity of bubble distributions are distinct with higher SFV. The pressure drop between bottom and top of fuel reactor with different values of SFV is shown in Figure 18.

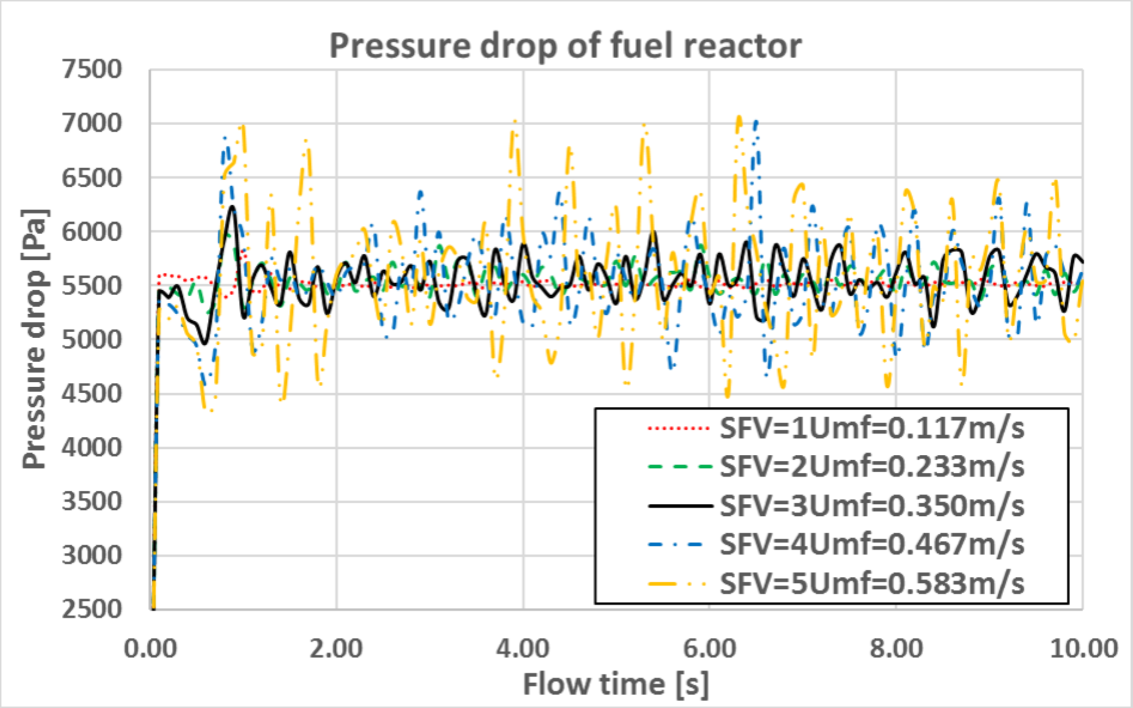

Figure 18 Pressure drop of fuel reactor with different superficial feeding velocity.

According to the numerical results, pressure drops with different SFV fluctuate around 5600Pa with time, hence, the SFV is an irrelevant factor for the average pressure drop. However, the instant values of pressure drop oscillate more significantly with higher SFV. The instant value of pressure drop remains nearly a constant which equals to 5600Pa when the fuel is fed with a SFV of $v = 1U_{mf}$, but waves dramatically in a big range of [-1200Pa, +1400Pa] with a SFV of $v = 5U_{mf}$.

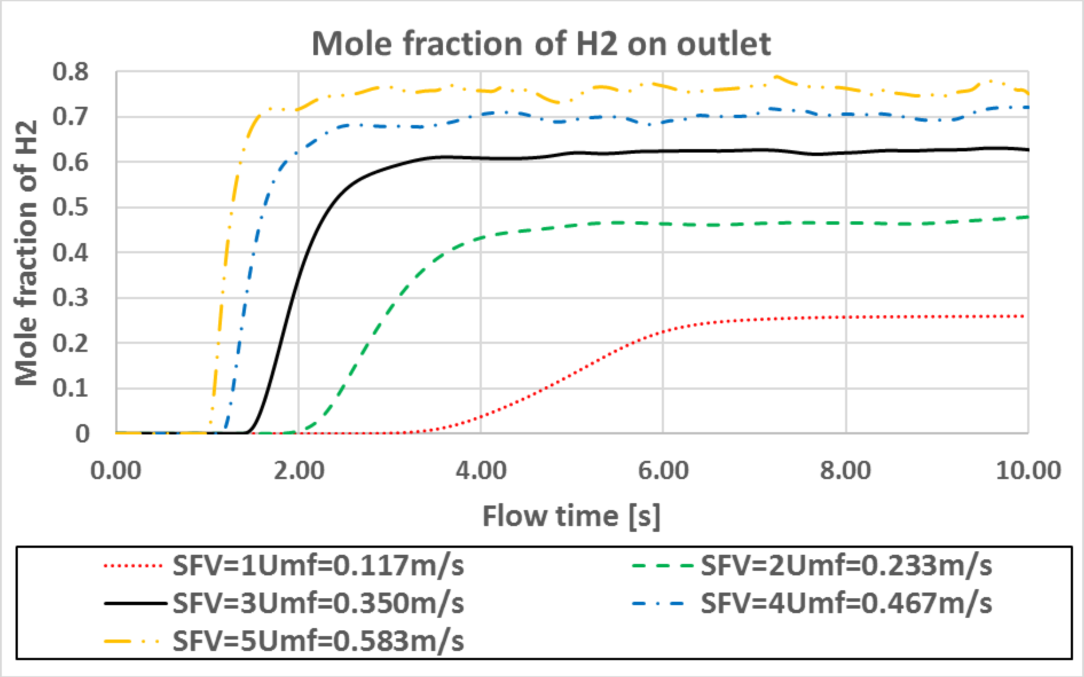

Figure 19 Mole fraction of H_2 on outlet along time with different SFV.

The mole fraction of H_2 on the outlet with different values of SFV is shown in Figure 19. With lower feeding velocity, a longer time is required for FR to obtain its quasi-steady state on mole fractions of gases on the outlet. However, it is also obvious that affected by the more significant fluctuation of pressure drop and more chaotic flow conditions within the FR with higher SFV, the mole fraction of H_2 on the outlet becomes unstable. Meanwhile, the average mole fraction of H_2 on outlet increases with higher SFV, by which more amount of fuel is fed into the FR.

4.7 Effects of Diameter of OC Particles

The minimum fluidization velocity MFV significantly depends on the diameter of OC particles, as mentioned above. Meanwhile, SFV does not only affect the flow condition within FR but also affects the conversion rate of fuel dramatically. The effects of the diameter of OC particles are studied in this section. Diameters $d_P = 0.2mm$, $d_P = 0.25mm$, $d_P = 0.275mm$ (base case), $d_P = 0.3mm$, and $d_P = 0.35mm$ are applied while the SFV remains $v = 0.35m/s$. The minimum fluidization velocities of corresponding diameters and the factors between SFV and MFVs are listed in Table 6 below.

Table 6 Minimum fluidization velocities of different particle diameters.

Diameter of OC particles	MFV	Factors between SFV&MFV
$d_P = 0.2mm$	$U_{mf} = 0.063mm$	$v = 5.6U_{mf}$
$d_P = 0.25mm$	$U_{mf} = 0.098mm$	$v = 3.6U_{mf}$
$d_P = 0.275mm$ (base case)	$U_{mf} = 0.117mm$	$v = 3.0U_{mf}$
$d_P = 0.3mm$	$U_{mf} = 0.139mm$	$v = 2.5U_{mf}$
$d_P = 0.35mm$	$U_{mf} = 0.187mm$	$v = 1.9U_{mf}$

As discussed in the previous section, the factors between SFV and MFV have obvious effects on the flow condition within FR. The contours of the volume fraction of solid at t=10.0s and the mole fraction of H_2 on outlet are shown in Figure 20.

a) Contours of volume fraction of solid at t=10.0s

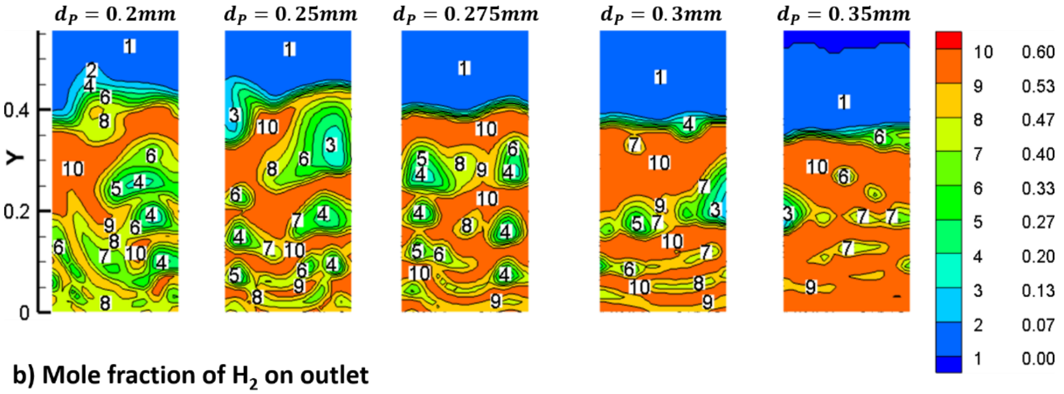

b) Mole fraction of H_2 on outlet

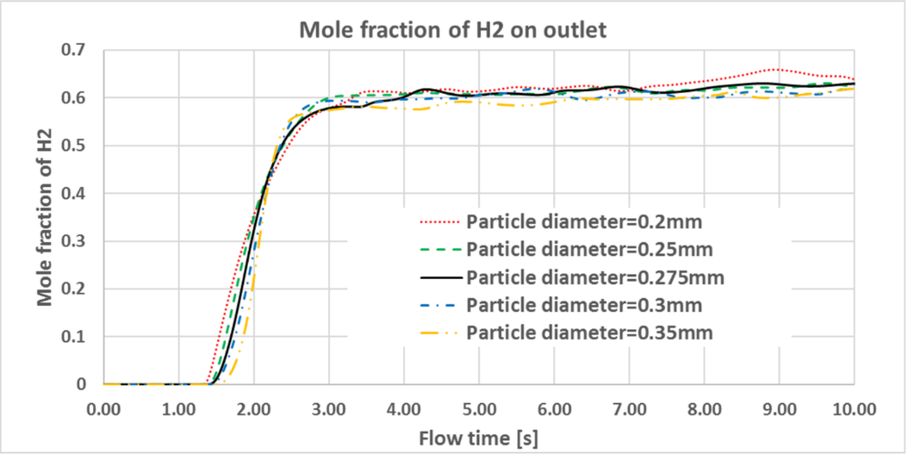

Figure 20 a) Contours of the volume fraction of solid at t=10.0s, and b) mole fraction of H_2 on the outlet.

The Smaller diameter of solid particles results in smaller MFV, hence, with constant SFV (i.e. 3.5m/s), the factor between SFV and MFV is larger (see Table 6). It can be seen that with a larger factor, OC particles can rise to a higher position resulting in larger bubbles and more chaotic flow conditions within FR. The mole fractions of H_2 on the outlet, however, different from the previous section, are almost not influenced by the factors between SFV and MFVs. With the constant SFV on the inlet, the mass flow rate of fuel is fixed. Hence, the conversion rates of fuel are mainly controlled by the chemical reaction kinetics rather than the flow conditions within FR.

4.8 Study of Gas Feeding Distributors

As discussed in the base case above, the mole fractions H_2 in gas phase on the regions with the higher volume fraction of OC are smaller. It is easy to conclude that more OC particles contribute to higher chemical reaction rate and hence higher fuel conversion. The results with different SFV also exhibited that the uniformity of gas bubbles distribution on the FR benefits the fuel conversion rate. Hence, several types of velocity distributors are tested in this section aiming to achieve a better uniform distribution of bubbles on FR and hence enhance the conversion rate of fuel.

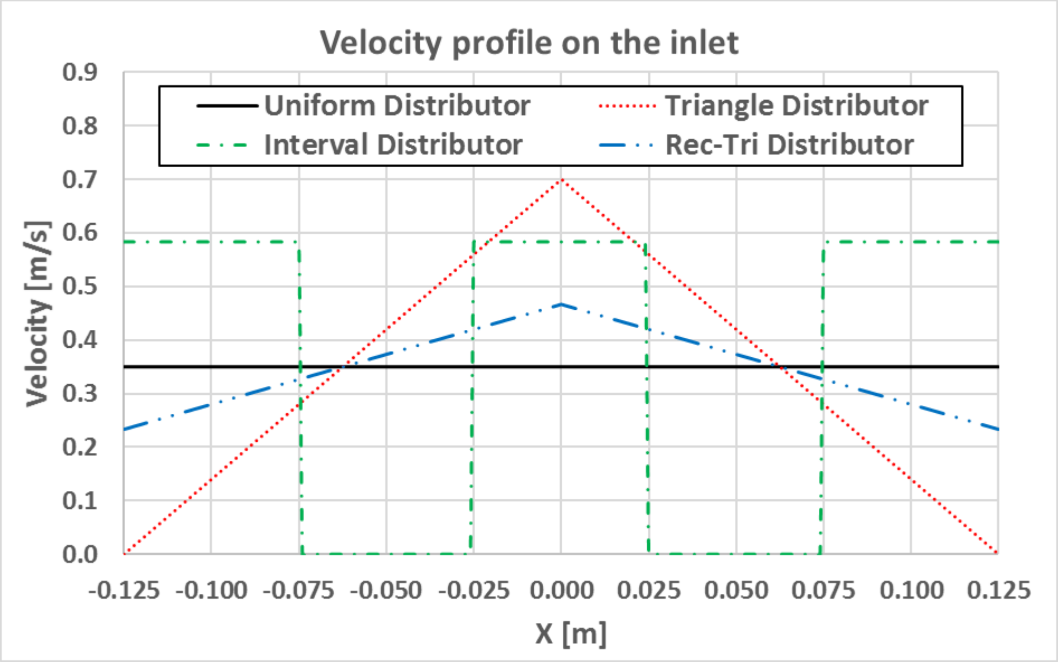

Figure 21 Velocity profile on the inlet using different distributors.

Figure 21 presents the velocity profiles of four different distributors including uniform distributor which has constant velocity and is used in the base case and triangle distributor which has the maximum velocity on the centerline and zero velocity on the edges of inlet. Other distributors are interval distributor which has intervals with zero velocity and rectangle-triangle distributor which has the maximum velocity on the center and nonzero velocity on the edges of inlet. Note that the total mass flow rates of fuel are the same even though the velocity profiles have various shapes.

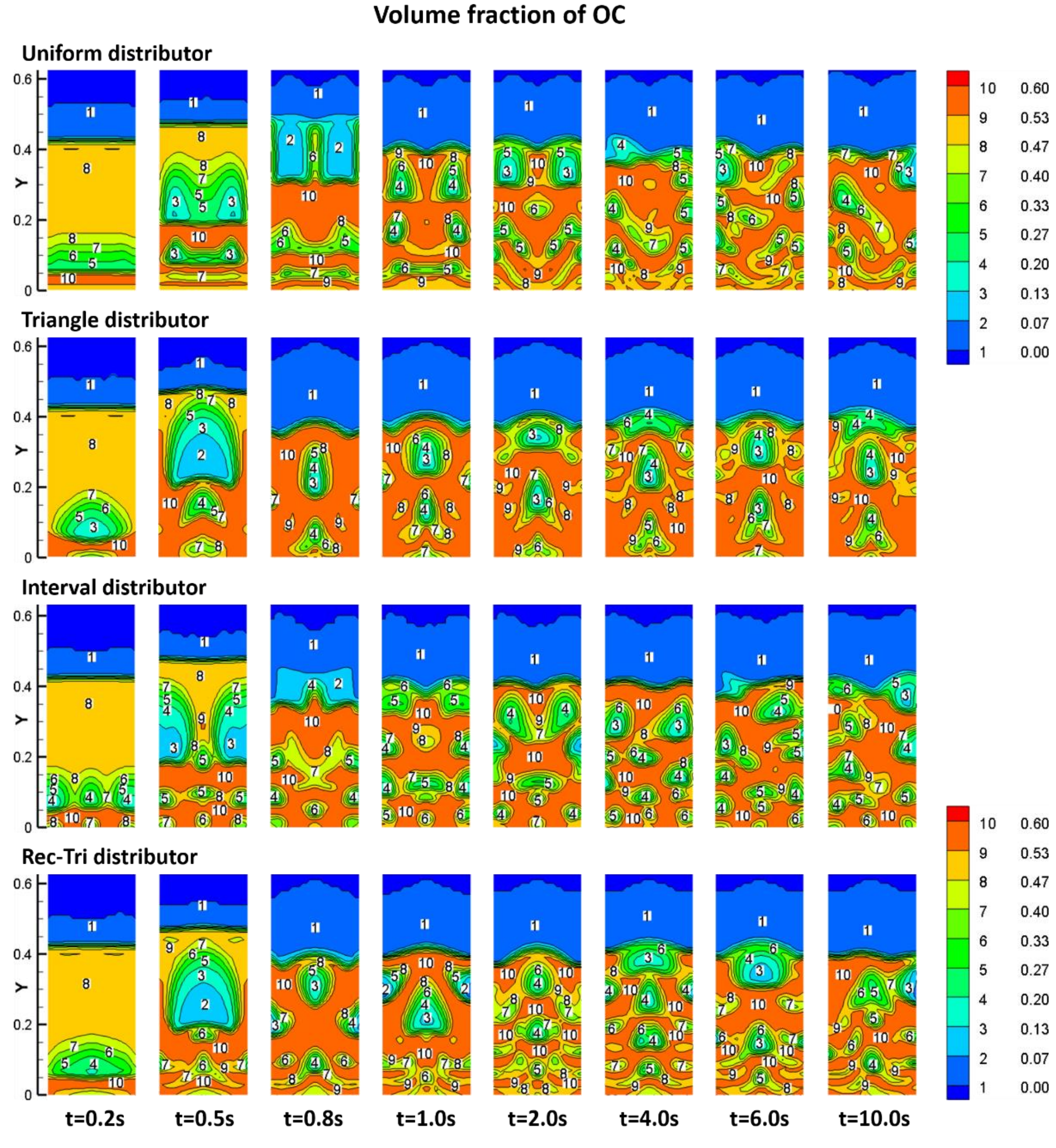

Figure 22 Volume fraction of solid phase with different distributors. Note that only the lower sections of FR contain solid particles are shown.

Figure 22 exhibits the volume fraction of solid phase with different distributors placed on the inlet of FR. Using the triangle distributor, the distribution of bubbles is more symmetric along the center line of FR. It can be seen that large bubbles appear in the middle region of FR while denser solid particles are found in the zone close to walls of the reactor. With the corresponding number of the bubbles showing on the inlet, the interval distributor produces more bubbles close to the walls of the reactor. Comparing to other cases, the sizes of bubbles produced by interval distributor are more uniform. More small bubbles arise near the walls using a rectangle-triangle distributor which has a minimum but nonzero velocity close to the walls and maximum velocity on the center of inlet. Similar to triangle distributor, the bubble distribution on FR with a rectangle-triangle distributor is also nearly symmetric, but more uniform than the triangle distributor.

a) Contours of mole fraction of H_2

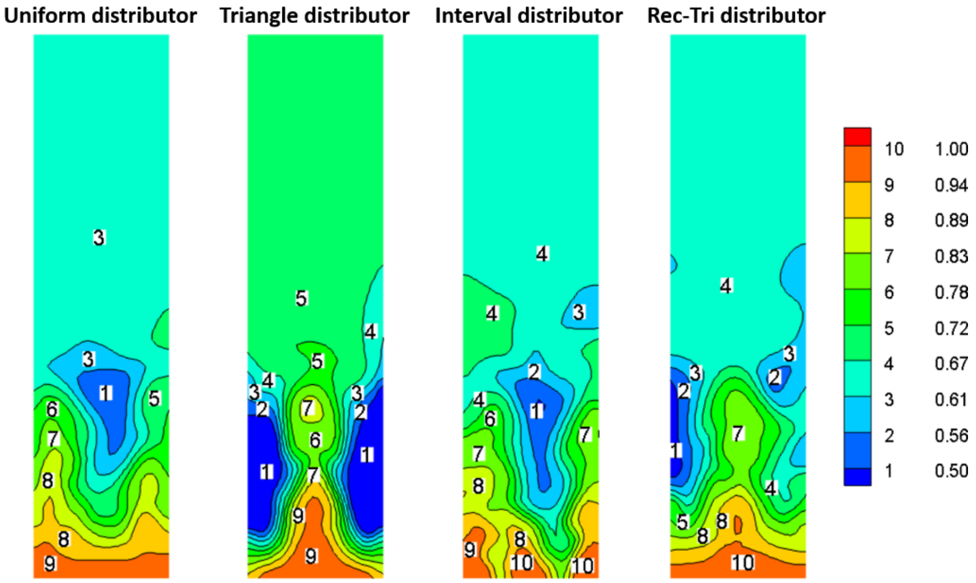

b) Mole fraction of H_2 on outlet

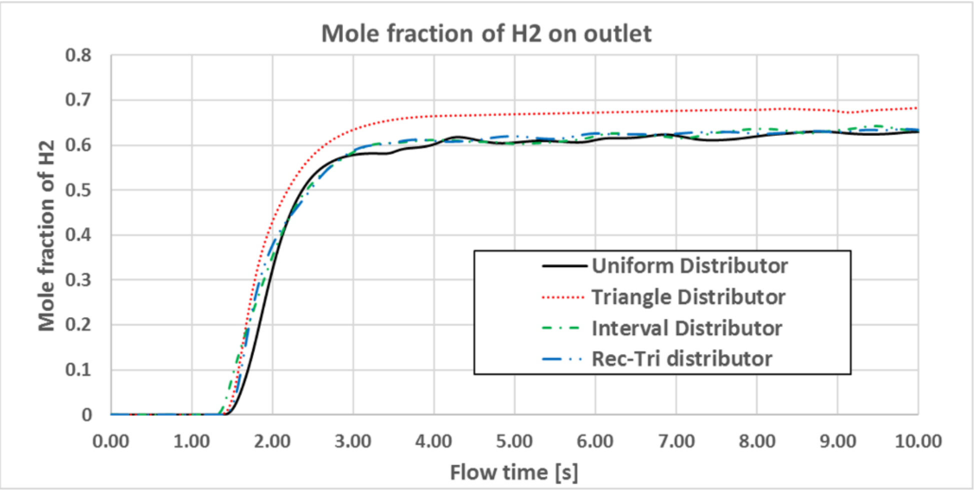

Figure 23 a) Contours of mole fraction of H_2 at t=10.0s, and b)plots of mole fraction of H_2 on the outlet.

Both the contours of mole fraction of H_2 on FR at t=10.0s and the plots of mole fraction of H_2 on outlet as a function of time are shown in Figure 23.

As presented in the base case, with the uniform distributor, more unreacted fuel (i.e. H_2) leaks through the zones near the walls than the center of FR. Similar to uniform distributor, the use of interval distributor results in major leakage of fuel on region close to the walls due to more bubbles and less solid particle appear on these areas. On the contrary, large bubbles arise on the center of FR using triangle and rectangle-triangle distributors which have the maximum velocity on the center. Consequently, better conversion of H_2 to water vapor is observed on areas close to walls but worse on center fields and hence higher mole fraction of residual H_2. The plots of mole fraction of H_2 on outlet indicate that the use of triangle distributor results in worse performance of H_2 conversion while interval and rectangle-triangle distributors have almost the same performance as a uniform distributor. It can be seen that the conversion of fuel is limited by the chemical reaction kinetics between $CaSO_4$ and H_2. It is difficult to enhance the conversion rate of H_2 by using distributors to produce a more uniform distribution of bubbles with the FR.

4.9 Conclusions of the Study of Fuel Reactor

The basic behaviors of a FR of chemical looping combustion are investigated in present work using numerical methods. Effects of mole fraction of CaS, operating temperature, superficial feeding velocity of fuel and the diameter of solid particles were discussed. The results indicate that the superficial feeding velocity of gaseous fuel has significant effects on the flow condition with FR and conversion performance while operating temperature mainly affects the fuel conversion. The study of particle sizes indicates that because of the limited chemical reaction rate between $CaSO_4$ and H_2, the conversion rate of H_2 is almost not influenced by the flow condition within FR. The mole fraction of CaS has the least effects among these three parameters. Meanwhile, several velocity distributors are also studied aiming to produce a more uniform distribution of bubble with FR and hence enhance the performance of conversion of H_2. The rectangle-triangle distributor results in better bubbles distributions, but the gain of higher fuel conversion rate is insignificant due to the low chemical activity of OC used in this study.

CHAPTER 5

STUDY OF RADIATIVE HEAT TRANSFER

5.1 Numerical Models and Validations

The study of radiative heat transfer with FR is conducted in this chapter. The Same geometry and materials are used in this study. The geometry is shown in Figure 6 while the properties of materials are listed in Table 3. However, the radiative properties of both gas and solid phases are still required.

Considering 99% of the black body emission at 1123K, the largest wavelength can be calculated to be $\lambda_{max,99\%} = 22.26\mu m$, then, the minimum size parameter can be evaluated as $\alpha_{R,min} = 28.21 > 20$. Hence, the particles within FR can be treated as large absorbers and scatterers.

Table 7 Radiative properties used in the base case.

Property	Gas phase	Solid phase
Absorption coefficient $[1/m]$	WSGGM	3750
Scattering coefficient $[1/m]$	WSGGM	3750
Scattering phase function	Isotropic	Isotropic

The differential equations and chemical reactions mentioned above are solved by the commercial CFD software code Fluent16.2 using the finite volume method running on a server with 2 processors which are 16 cores 3.1GHz Intel Xeon CPUs. Numerical models used by present study are listed in Table 8.

Table 8 Numerical models used by radiative heat transfer study.

Numerical Method	Model or value	Numerical Method	Model or value
Multiphase model	Eulerian-Eulerian	Drag coefficient	Gidaspow [27]
Turbulent model	Dispersed standard k-e	Granular conductivity	Gidaspow [27]
Radiation model	Discrete Ordinates	Granular viscosity	Gidaspow [27]
Scattering phase function	Isotropic	Granular Bulk Viscosity	Lun et al. [30]
Friction viscosity	Schaeffer [32]	Solids pressure	Lun et al. [30]
Angle of internal friction	30°	Radial Distribution	Lun et al. [30]
Spatial discretization	2nd order upwind	Packing Limit	0.6
Heat transfer coefficient	Gunn [28]	Restitution coefficient	0.9
Pressure-velocity coupling	Phase coupled SIMPLE		

The average value of the viscosities of water vapor and H_2 are considered as the viscosity of gas phase. Taking calcium sulfate as the oxygen-carrier and diameter of OC particles as $d_p = 0.2mm$, the minimum fluidization velocity can be calculated as

$$U_{mf} = 0.055m/s \tag{5.1}$$

For the base case in this study, a velocity of $3U_{mf} = 0.165m/s$ on the inlet is used for feeding gas. The thermal boundary condition on the wall is considered to be radiative-convective. All boundary and initial conditions are listed in Table 9.

Table 9 Boundary and initial conditions for radiative heat transfer study.

BC	Value	IC	Value
Inlet BC type	Velocity inlet	Initial gas	He
Superficial velocity of feeding gas	0.165m/s (3*MFV)	Initial temperature of gas	1123K
Feeding gas temperature	1123K	Initial temperature of solid	1123K
Outlet BC type	Pressure outlet	Initial mole fraction of CaS	0.2
Outlet pressure	0 Pa	Initial volume fraction of solid	0.48
Walls	Mixed, free stream & external radiation temperature 300K, heat transfer coefficient $10w/m^2K$, external & internal emissivity 0.75		

With the boundary conditions and initial conditions presented, then we can test the mathematical models described above. The comparison of mole fraction of H_2 on the outlet between recent work and Harichandan and Shamim[17] is shown in Figure 24, which also depicts the conversion of $CaSO_4$ by recent work and experimental work by Kim et al. [15]. The mole fraction of H_2 on the outlet by recent study has higher fluctuation, comparing to the numerical work by Harichandan and Shamim [17]. The models presented above, however, are still valid. Due to the low reactivity between $CaSO_4$ and H_2, the conversion of $CaSO_4$ increases slowly along time. As we can see, the conversion of $CaSO_4$ by this work has good agreements with experimental work.

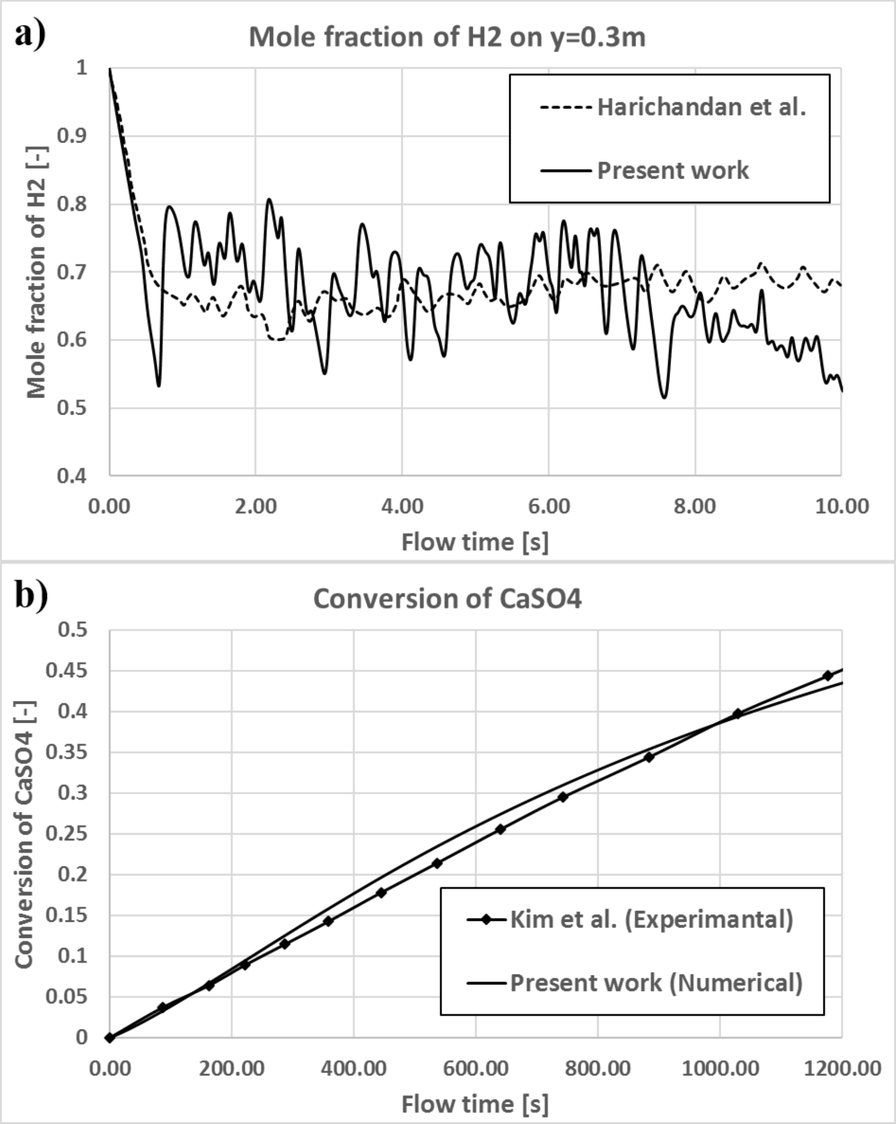

Figure 24 Plots of a) mole fraction of H_2 on the outlet by recent study and Harichandan and Shamim [17], and b) conversion of $CaSO_4$ by recent work and Kim et al. [15].

5.2 Discussions of Base Case

Using the parameters mentioned above, we obtained the numerical results for the base case. The contours of the volume fraction of oxygen carrier particles, absorption coefficient, scattering coefficient, and incident radiation are depicted in Figure 25.

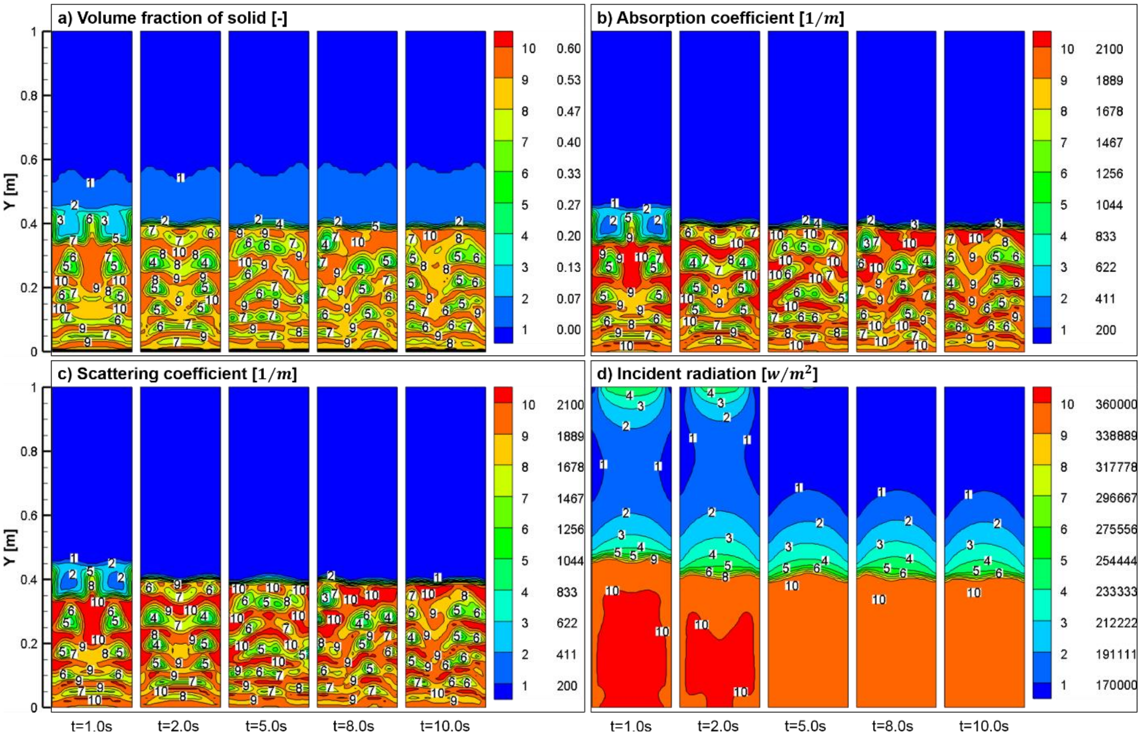

Figure 25 Contours of a) volume fraction of solid, b) absorption coefficient, c) scattering coefficient, and d) incident radiation.

With superficial feeding velocity equaling to 3 times of minimum fluidization velocity, the FR was running under bubbling bed condition. The bubbles in the middle region are small and uniform comparing to bubbles in the zones close to walls. Since the reflectivity of solid particles was taken as 0.5, the absorption coefficient and scattering coefficient of solid phase have the same value. It is very obvious that the contours of the absorption coefficient and scattering coefficient are nearly identical. Meanwhile, the contours of both absorption coefficient and scattering coefficient have the same distribution as the volume fraction of solid phase. This indicates that comparing to the absorption and scattering effects of gases within FR, the absorption and scattering effects of solid phase are more dominant. With the chaotic flow condition, the incident radiation within FR fluctuates widely before t=5.0s. However, the contours of incident radiation become nearly stabilized after t=5.0s. Evidently, the incident radiation on the region of static bed is larger than the free bed after t=5.0s. In order to study the effect of considering radiation with FR, the comparisons of contours of the volume fraction of solid, chemical reaction rate, the temperature of gas, the temperature of solid, mole fraction of H_2, and mole fraction of H_2 on outlet between radiation considered and .radiation neglected are shown in Figure 26.

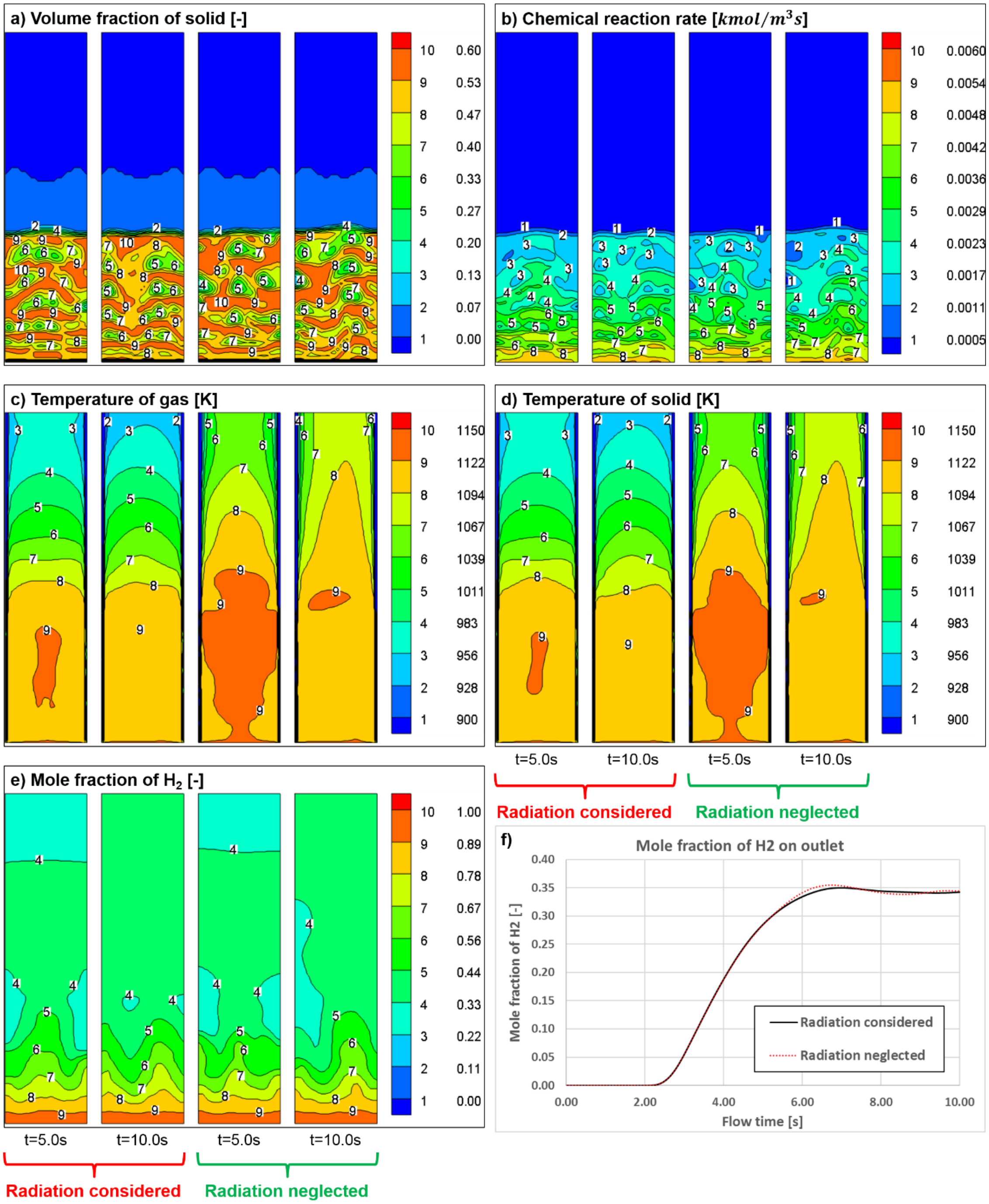

Figure 26 Comparisons of contours of a) volume fraction of solid, b) chemical reaction rate, c) temperature of gas, d) temperature of solid, e) mole fraction of H_2 between radiation considered case and radiation neglected case at t=5.0s and t=10.0s, , and f) mole fraction of H_2 on outlet.

The comparison of the contours of the volume fraction of solid phase between radiation considered case and radiation neglected case shows that the effects of radiation on flow pattern within FR are insignificant. With consideration of radiation, the temperature distribution within FR become less uniform for both solid phase and gas phase on the upper zones where the larger amount of heat loss to the ambient due to the contribution of radiation within FR. However, the temperature in the lower zones with dense solid were not affected by the radiation in this configuration. Hence, the chemical reaction rate within the entire FR is nearly not influenced, and consequently, the distributions of mole fraction of H_2 are almost identical for both considerations. It can be seen from the plots of mole fraction of H_2 on the outlet that both systems got quasi-steady after t=7.0s when mole fractions of H_2 on the outlet reached the highest level and remained nearly constant forwards. However, it is worth noting that the reduction reaction is an exothermic reaction with a small amount of releasing of heat. For the endothermic case, the more uniform distribution of temperature may enhance the performance of gas heating, and hence obtain higher fuel conversion rate.

5.3 Effects of Boundary Conditions

The effects of boundary conditions on reactor walls are discussed in this section. Three types of the BCs are studied, as listed in Table 10.

Table 10 Comparison of boundary conditions on walls.

BC on reactor walls	Value

Constant temperature	1123K
Adiabatic	-
Mixed (base case)	Free stream & external radiation temperature 300K, heat transfer coefficient $10w/m^2K$, external & internal emissivity 0.75

The temperature profiles and the differences between radiation considered and neglected along the vertical center line of FR at 10s under different BCs on walls are plotted in Figure 27 below.

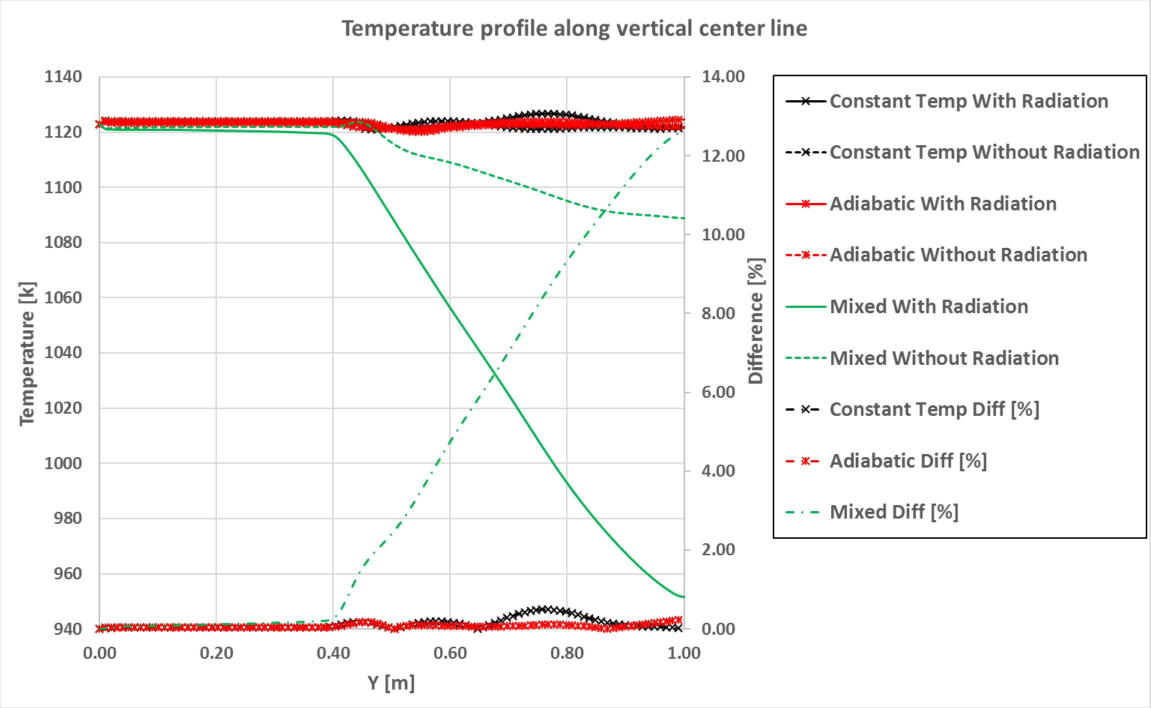

Figure 27 Comparison of temperature profiles and differences between radiation considered and neglected along the vertical center line at 10s with different BCs on walls.

Temperature profiles along the vertical center line of FR under BCs of constant temperature and adiabatic on FR walls have a very insignificant difference. The consideration of radiative heat transfer does not affect the temperature profile under these two BCs along the entire height. With a mixed heat transfer BC on the wall, similar results are observed with the static bed region. On the other hand, temperature with the free bed region is lower under mixed BC, with and without radiation. However, radiative heat transfer contributes to the heat loss on the free bed region. The difference between radiation considered and neglected increases along the height.

The comparisons of mole fraction of H_2 on the outlet under different BCs are depicted in Figure 28.

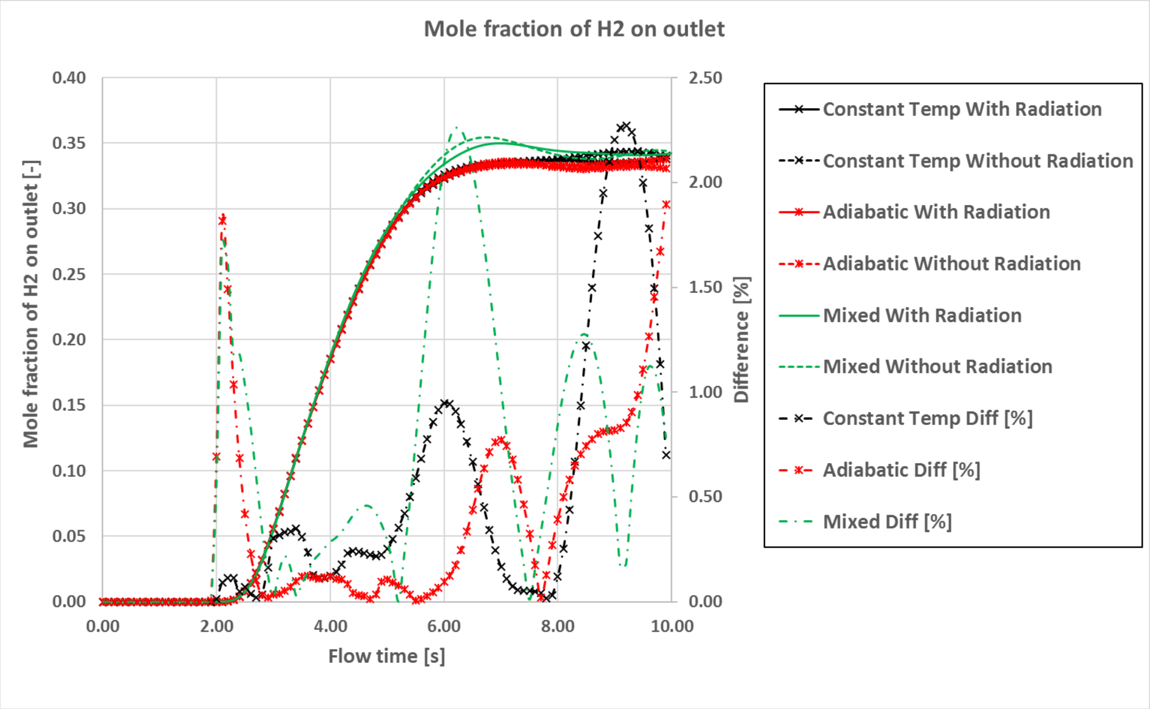

Figure 28 Comparison of mole fraction of H_2 and differences between radiation considered and neglected on the outlet with different BCs on walls.

The mole fractions of H_2 on the outlet with all three types of BCs have nearly the same profile along flow time, except the mole fraction of H_2 under mixed BC within 6.0s-8.0s is slightly higher. The differences of mole fraction of H_2 between radiation considered and neglected, however, are less than 2.5% during the entire simulation flow time.

As illustrated above, with mixed BC on reactor bed, the temperature within the free bed region is lower than other two BCs. However, with the nearly no OC particles filled in free bed region, the chemical reaction is hardly affected, resulting in similar fuel conversion performance.

5.4 Effects of Reflectivity of Solid Particles

As mentioned above, it is the absorption and scattering effects of solid phase that dominate radiation heat transfer within the reactor. The effects of reflectivity of solid particles are studied in this section. With different values of reflectivity of OC particles, the contours of the absorption coefficient, scattering coefficient, and incident radiation at t=10.0s are plotted in Figure 29. As we can see, both absorption coefficient and scattering coefficients depend on the reflectivity of OC particles dramatically. Similar to the discussion of the base case above, because of their essential relations with the reflectivity of solid particles, the distributions of the absorption coefficient and scattering coefficients are identical.

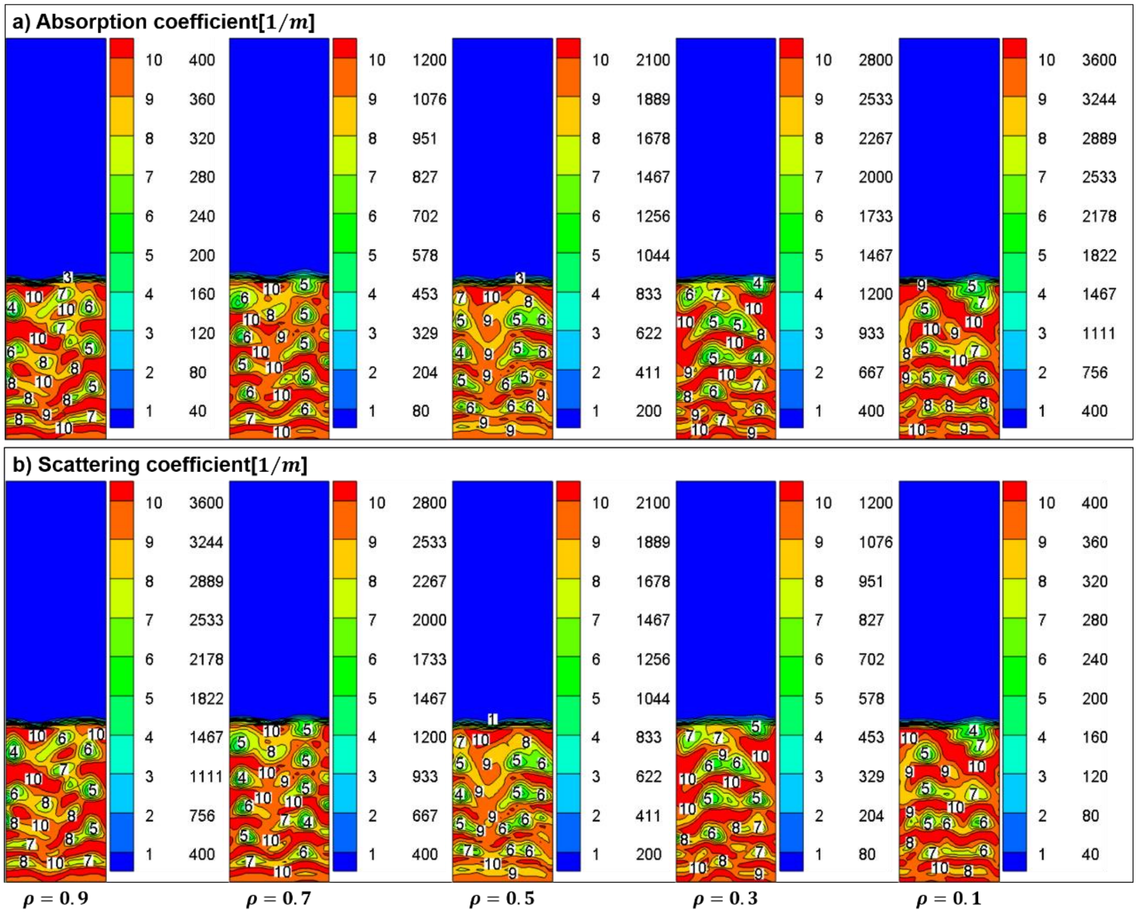

Figure 29 Contours of a) absorption coefficient and b) scattering coefficient at t=10.0s.

In order to investigate the effects of radiation and reflectivity on conversion performance, the comparison of contours of chemical reaction rate and mole fraction of H_2 between cases with different reflectivity and radiation neglected at t=10.0s are shown in Figure 30. Chemical reaction rate on the bottom of FR increases slightly with smaller values of reflectivity which results in higher absorption coefficient. However, the effects of reflectivity on chemical reaction rate in the upper zones of FR are very inconspicuous. This results in nearly no effects on fuel conversion rate, which is depicted in Figure 31 as well.

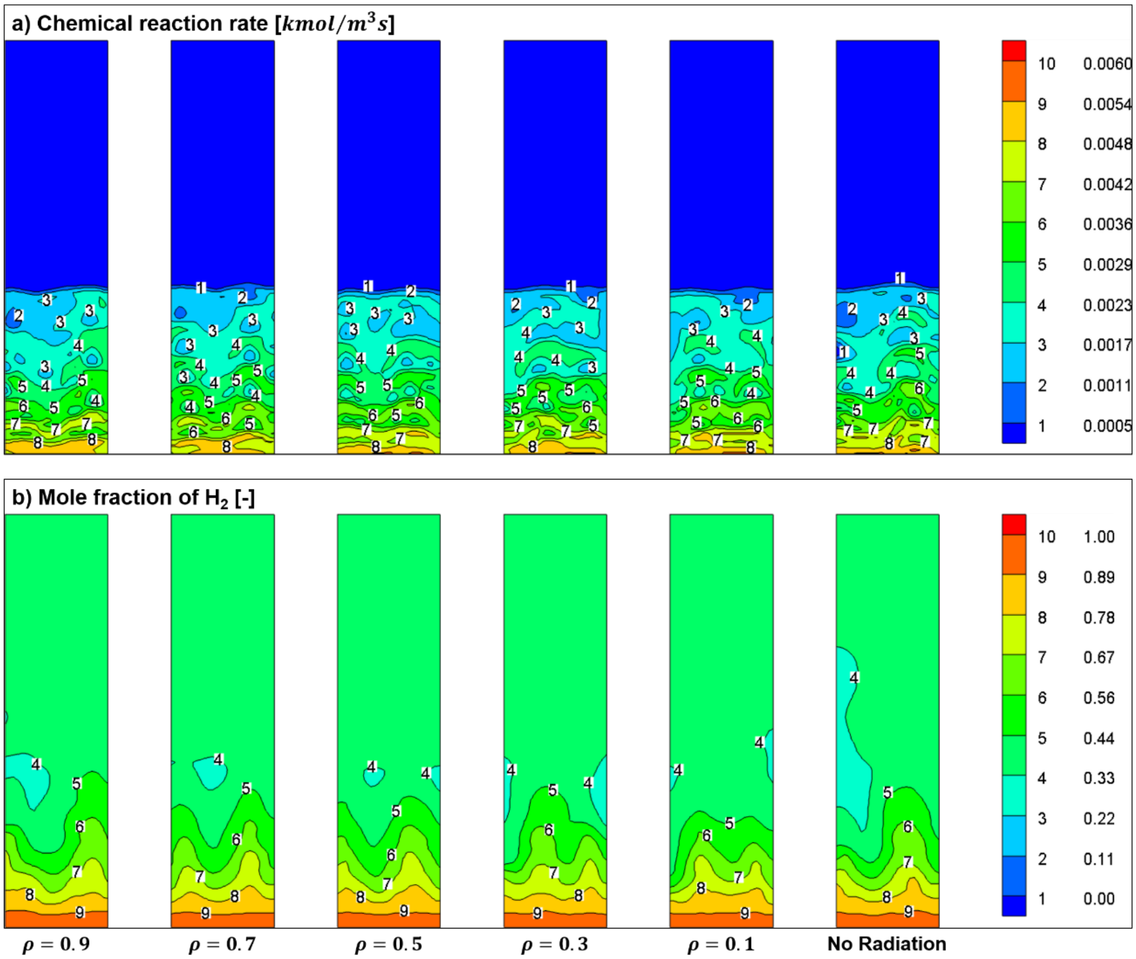

Figure 30 The comparison of contours of a) chemical reaction rate and b) mole fraction of H_2 between cases with different reflectivity and radiation neglected at t=10.0s.

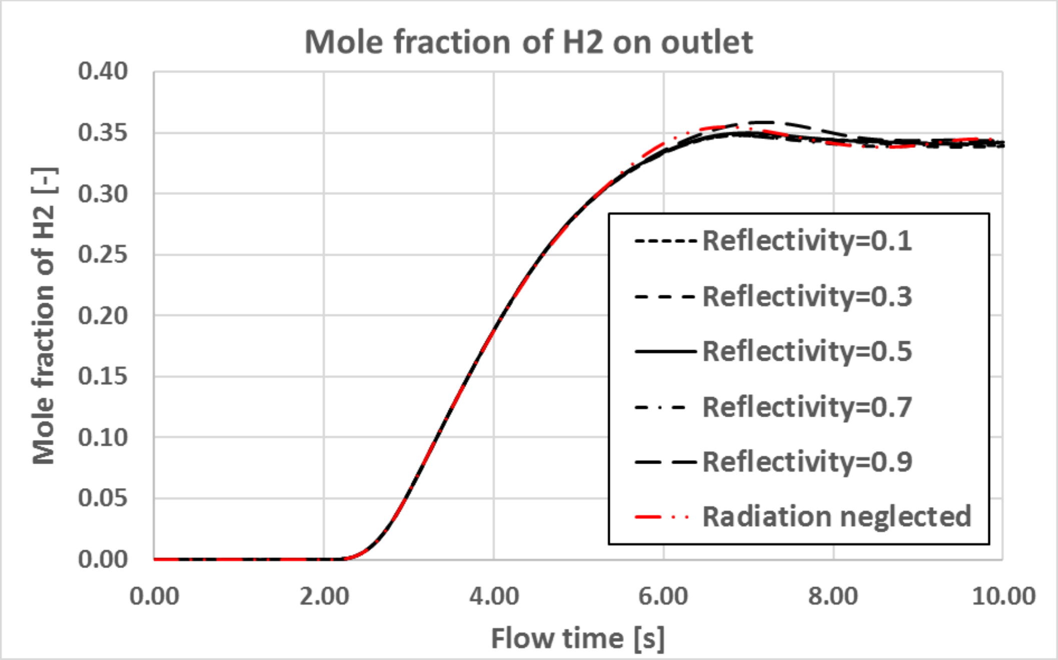

Figure 31 Mole fraction of H_2 outlet with different reflectivities of OC particles.

5.5 Effects of Particle Size

As mentioned above, not only the minimum fluidization velocity but also the absorption and scattering coefficient of solid particles are functions of OC particle size. Taking superficial feeding velocity of gas phase $v = 0.165 m/s$ and reflectivity of solid particles $\rho = 0.5$, the MFV, factors between SFV and MFV, absorption and scattering coefficients are listed in Table 11 below.

Table 11 Minimum fluidization velocity, absorption and scattering coefficient for different particle diameters.

Particles diameters $[mm]$	MFV $[m/s]$	Factors between SFV & MFV	Absorption & scattering coefficient $[1/m]$
$D_P = 0.15$	$U_{mf} = 0.031$	$v = 5.3U_{mf}$	$(\sigma_a)_s = (\sigma_s)_s = 5000$

$D_P = 0.2$	$U_{mf} = 0.055$	$v = 3.0U_{mf}$	$(\sigma_a)_s = (\sigma_s)_s = 3750$
$D_P = 0.25$	$U_{mf} = 0.085$	$v = 1.9U_{mf}$	$(\sigma_a)_s = (\sigma_s)_s = 3000$

Contours of the volume fraction of solid, absorption coefficient, scattering coefficient, and incident radiation with different particle diameters at t=10.0s are depicted in Figure 32.

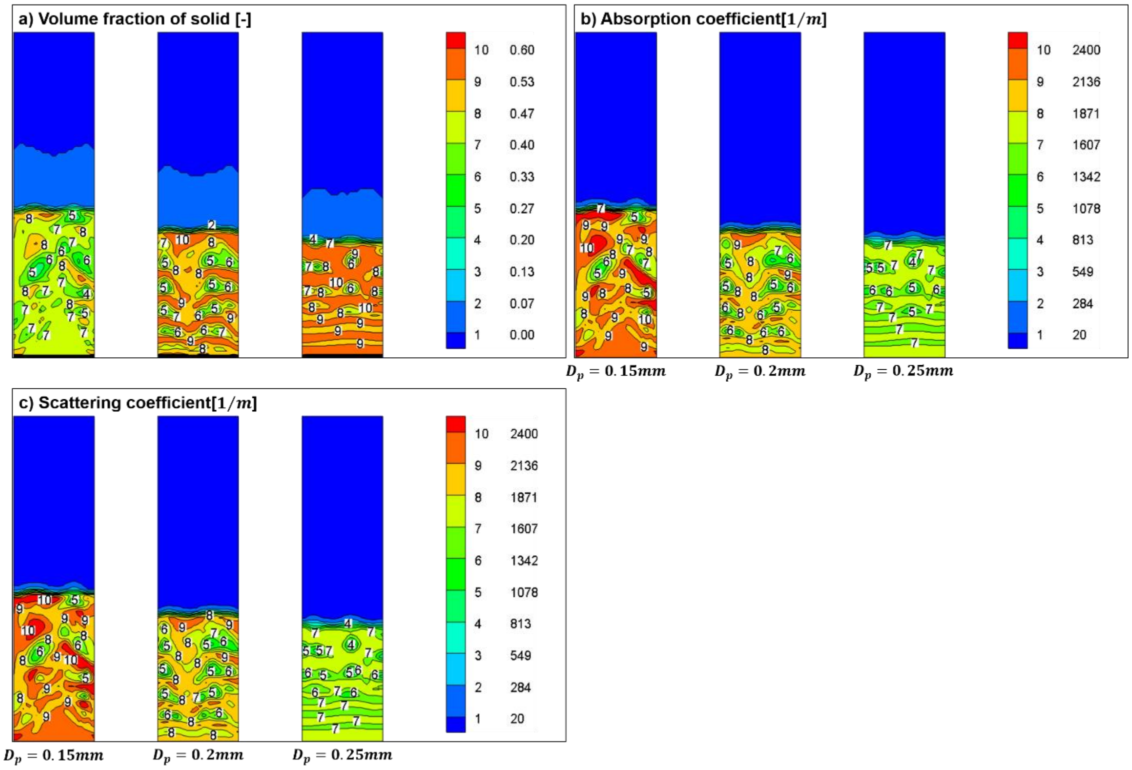

Figure 32 Contours of a) volume fraction of solid, b) absorption coefficient, and c) scattering coefficient with different particle diameters at t=10.0s.

With larger OC particles filled, the static bed region of FR becomes denser as the superficial feeding velocity remaining constant. However, the absorption and scattering coefficients decrease as D_P increases from 0.15mm to 0.25mm because absorption and scattering coefficients are decreasing functions of D_P. The incident radiation on bottom layer of FR increases as the height of static bed decreases while the upper region on static bed almost remains the same.

The effects of particle size on chemical reaction rate and fuel conversion performance are shown in Figure 33 which illustrates the volume fraction of solid, chemical reaction rate, and mole fraction of H_2 between different particle diameters and cases with or without radiation at t=10.0s.

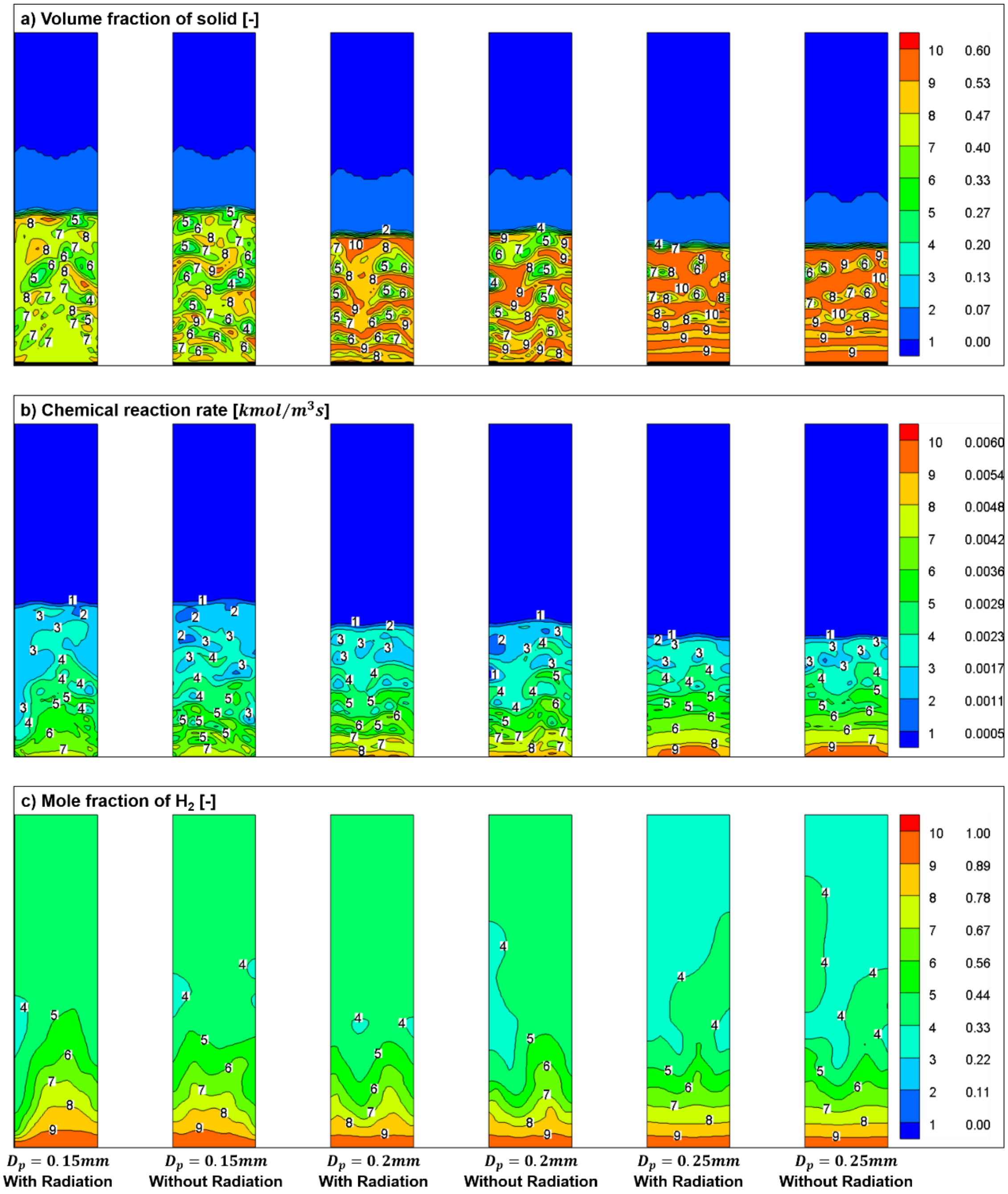

Figure 33 Comparison of contours of a) volume fraction of solid, b) chemical reaction rate, and c) mole fraction of H_2 between different particle diameters and cases with or without radiation at t=10.0s.

The contours of solid volume fraction for cases with radiation considered and neglected have nearly the same distributions, which indicates that the effects of radiation consideration on flow conditions can be neglected even the particle size has a significant impact on flow pattern within FR. Lower static bed height increases the chemical reaction rate at the same height, especially at the bottom of FR because of the enhancement on chemical reaction caused by the denser distribution of OC particles. The mole fraction of H_2, consequently, decreases slightly as D_P increasing, meaning small enhancement on fuel conversion performance.

5.6 Effects of Operating Temperature

As mentioned in the discussion of the base case, the consideration of radiation enhances the heat transfer performance within the reactor, and hence results in a more uniform distribution of temperature. The effects of operating temperature are studied in this section.

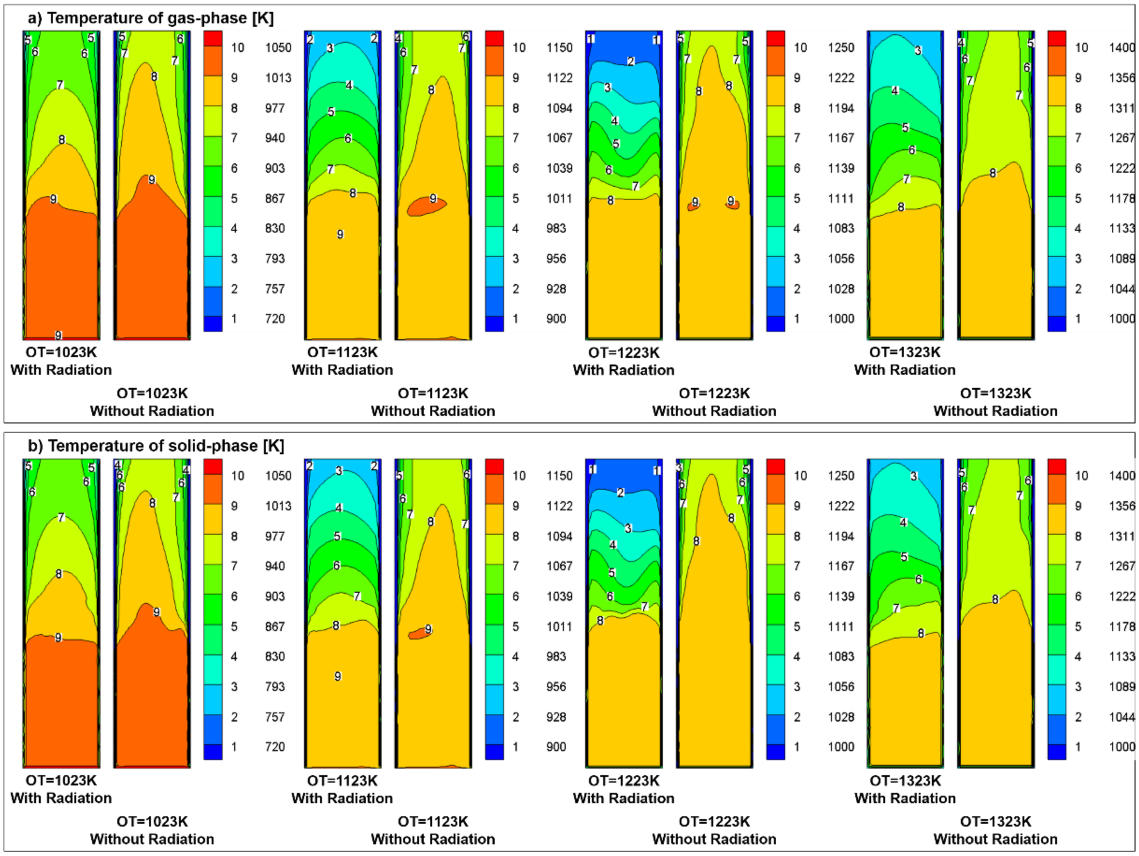

Figure 34 Contours of a) temperature of gas-phase, and b) temperature of solid-phase under different operating temperature with radiation considered and neglected at t=10.0s.

As shown in Figure 34, due to the interphase heat exchange between gas-phase and solid-phase, the temperature distributions of gas-phase and solid-phase are nearly identical for all the cases. Moreover, we can see that due to the enhancement of heat transfer caused by radiation, the temperature gradients in the upper part of FR of cases with radiation considered are larger than cases without radiation consideration. However, this uniformity function on the temperature distribution of radiation decays with higher operating temperature. The reason being is that with a small amount of heat releasing by chemical reaction, the heating effects on both gas and solid phases decays with increasing operating temperature. Hence, the temperature tends to be more uniform as operating temperature goes higher and the effects of radiation on temperature distribution decays.

The mole fraction of H_2 on the outlet of FR under different operating temperature with radiation considered and neglected is shown Figure 35.

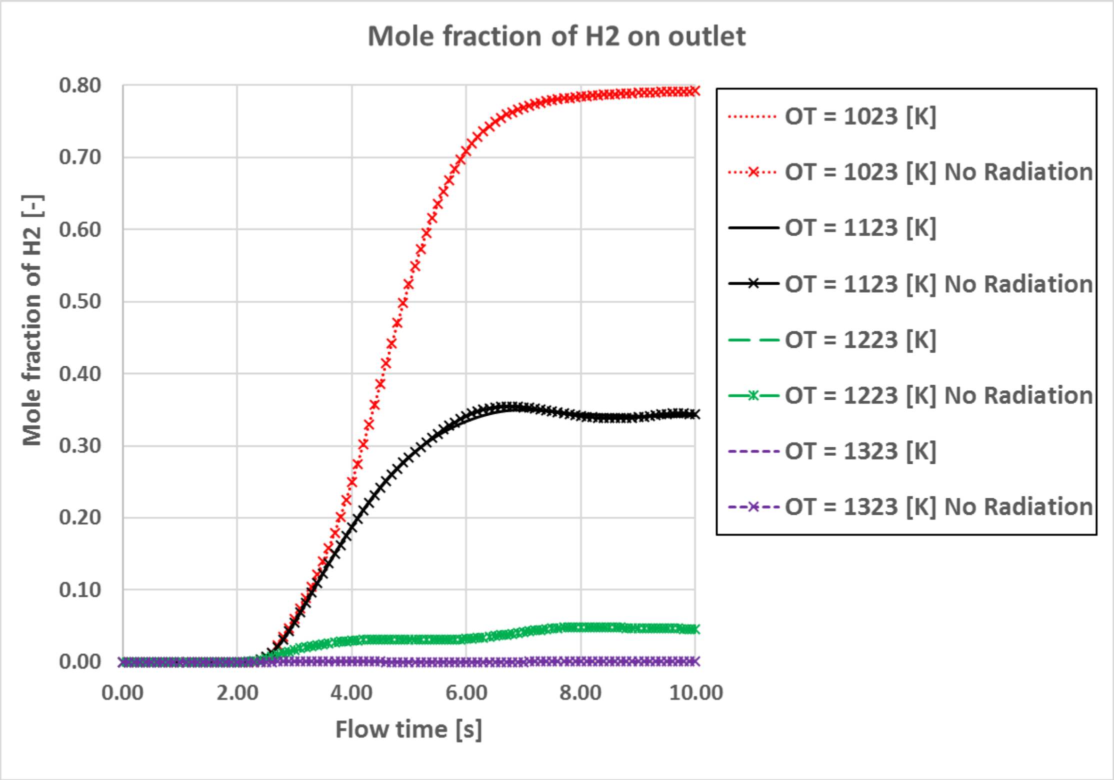

Figure 35 Mole fraction of H_2 on outlet under different operating temperatures with radiation considered and neglected.

Since the chemical reaction rate is an exponential function of temperature, the fuel conversion rate increases dramatically with higher operating temperature. With operating temperature higher than 1323K, the feeding fuel can be fully converted into H_2O vapor. However, the effects of radiation on fuel conversion performance are very insignificant.

5.7 Conclusions of the Study of Radiative Heat Transfer within Fuel Reactor

Present work models the radiative heat transfer within a FR of CLC systems. This model can also be applied in AR as well. The calculation method of the absorption coefficient and scattering coefficient of both gas and solid phases are declared. Comparing to the base case, the effects of boundary conditions, the reflectivity of solid material, particle size, and operating temperature are investigated. With radiative heat transfer within FR, the temperature distribution within reactor becomes more uniform, especially for systems running at a lower temperature. On the other hand, radiation also contributes to heat loss through walls of FR, especially on free bed region, resulting in the larger temperature gradient. On the static bed, the temperature variations are insignificant due to the higher heat capacity of dense solid particles. However, the effects of radiation on temperature profiles are evidential within free bed where solid particles are very sparse. Hence, the effects of radiation on fuel conversion performance are very limited. But we expect better heating performance on systems with endothermic chemical reaction within FR. Meanwhile, the effects of radiation on flow pattern are also insignificant.

CHAPTER 6

STUDY OF AIR REACTOR

6.1 Numerical Models and Validations

Oxidation chemical reactions between reduced form OC and oxygen are always exothermic, while reduction chemical reactions within FR may be exothermic or endothermic depending on the materials of OC. NiO is chosen as the OC for AR study in this chapter. The oxidation chemical reaction within AR can be expressed as

$$2Ni + O_2 = 2NiO \qquad \Delta H = -240kJ/mol(NiO) \tag{6.1}$$

It is a highly exothermic oxidation reaction.

The main properties of materials used in the present study are listed in Table 12.

Table 12 Properties of materials used in AR study.

Property	N_2	O_2	Ni	NiO
Density (kg/m3)	1.138	1.2999	3200	3200
Thermal Conductivity (w/m-K)	0.0242	0.0246	91.74	6.2
Viscosity (kg/m-s)	1.663e-5	1.919e-5	1.09e-5	1.09e-5
Particle diameter (mm)			0.2	0.2

The geometry of AR which has a 0.08m diameter cylinder on the bottom and a 0.04m diameter cylinder on the top is shown in Figure 36. The grid size is taken as 5mm at both horizontal and vertical directions.

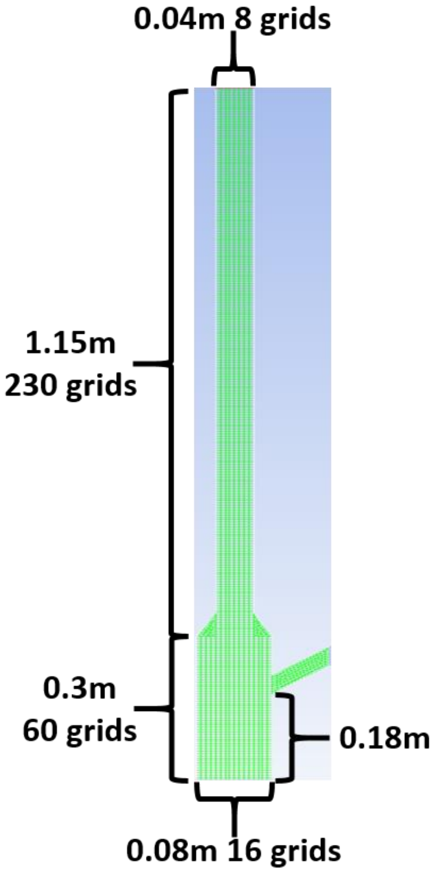

Figure 36 Geometry and mesh of air reactor. Note that the height has been scaled for better exhibition.

Taking the diameter of solid particles as 0.2mm, the density of OC as 3200kg/m^3, the viscosity of gas phase as 2.0e-5 kg/m-s, the density of gas as 1.22kg/m^3, the minimum fluidization velocity can be estimated as $U_{mf} = 0.0377m/s$ by applying Eq.(3.64)-Eq.(3.66).

The numerical scheme used in present study are listed in Table 13.

Table 13 Numerical scheme applied in AR study.

Numerical Method	Model or value	Numerical Method	Model or value
Multiphase model	Eulerian-Eulerian	Drag coefficient	Gidaspow [27]
Turbulent model	Dispersed standard k-e	Granular conductivity	Gidaspow [27]
Granular viscosity	Gidaspow [27]	Solids pressure	Lun et al. [30]
Granular Bulk Viscosity	Lun et al. [30]	Radial Distribution	Lun et al. [30]
Friction viscosity	Schaeffer [32]	Heat transfer coefficient	Gunn [28]
Angle of internal friction	30°	Restitution coefficient	0.9
Packing Limit	0.6	Friction Packing Limit	0.5
Pressure-velocity coupling	Phase coupled SIMPLE	Spatial discretization	2^{nd} order upwind
Time step	0.5ms	Transient formulation	2^{nd} order implicit

Air inlet on the bottom and OC inlet in the side are considered as velocity inlet BC while depleted air outlet on the top is considered as pressure outlet. All walls of AR are taken as adiabatic. Major BCs applied for base case study are listed in Table 14.

Table 14 Boundary condition for AR base case study.

BC	Value	IC	Value
Superficial feeding velocity of air	$20 * U_{mf} = 0.755 m/s$, 300K	Initial gas	N_2

Feeding mass flow rate of OC	$6.144 kg/s$, 300K, NiO 30mole%	Initial temperature	1173K
Pressure on outlet	$0 Pa$	Initial mole fraction of NiO	0.3
Walls	Adiabatic	Initial volume fraction of solid	0.48
		Initial inventory of OC	$33.8 kg$

Unreacted shrinking core model (USCM) is used to determine the chemical reaction rate between oxygen and Ni within AR. According to Zafar et al. [58], chemical reaction rate between O_2 and Ni can be evaluated by

$$\frac{dZ_s}{dt} = \frac{3b}{\rho_m r_g} k_0 e^{-E/RT} C_g^n (1 - Z_s)^{2/3} \tag{6.2}$$

Here, Z_s is the conversion degree of Ni. $b = 2$, $\rho_m = 47712$, $r_g = 0.19e - 6$, $k_0 = 5.43e - 3$, $E = 40$, $n = 1$.

The validation results of models used in present work against experimental work presented by Zafar et al. [58] are shown in Figure 37. Good agreements are gained between these two works.

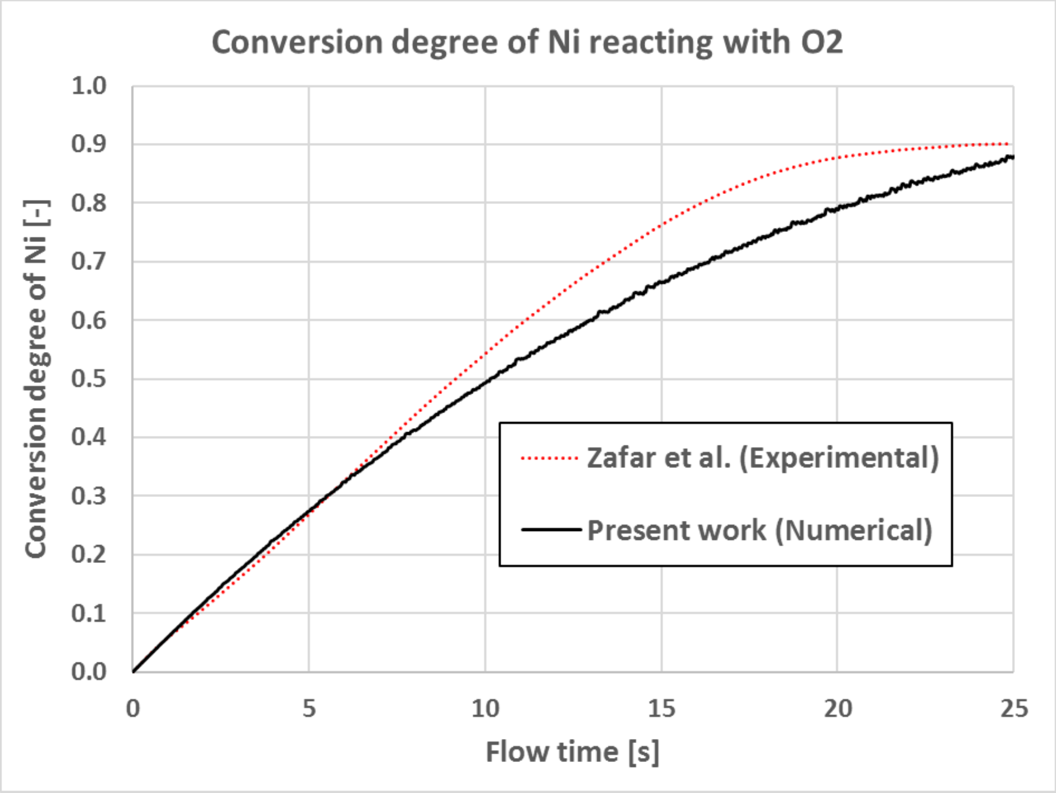

Figure 37 Validations of chemical reaction kinetics between present work and published experimental work.

6.2 Discussions of base case

Using the configurations listed above, we can conduct the base case study of an AR. Meanwhile, as mentioned above, temperature gradients are much higher in sparse regions than in dense regions. It is important to clarify the effects of radiative heat transfer within air reactor. The reflectivity of OC particles is set to 0.7 by this study.

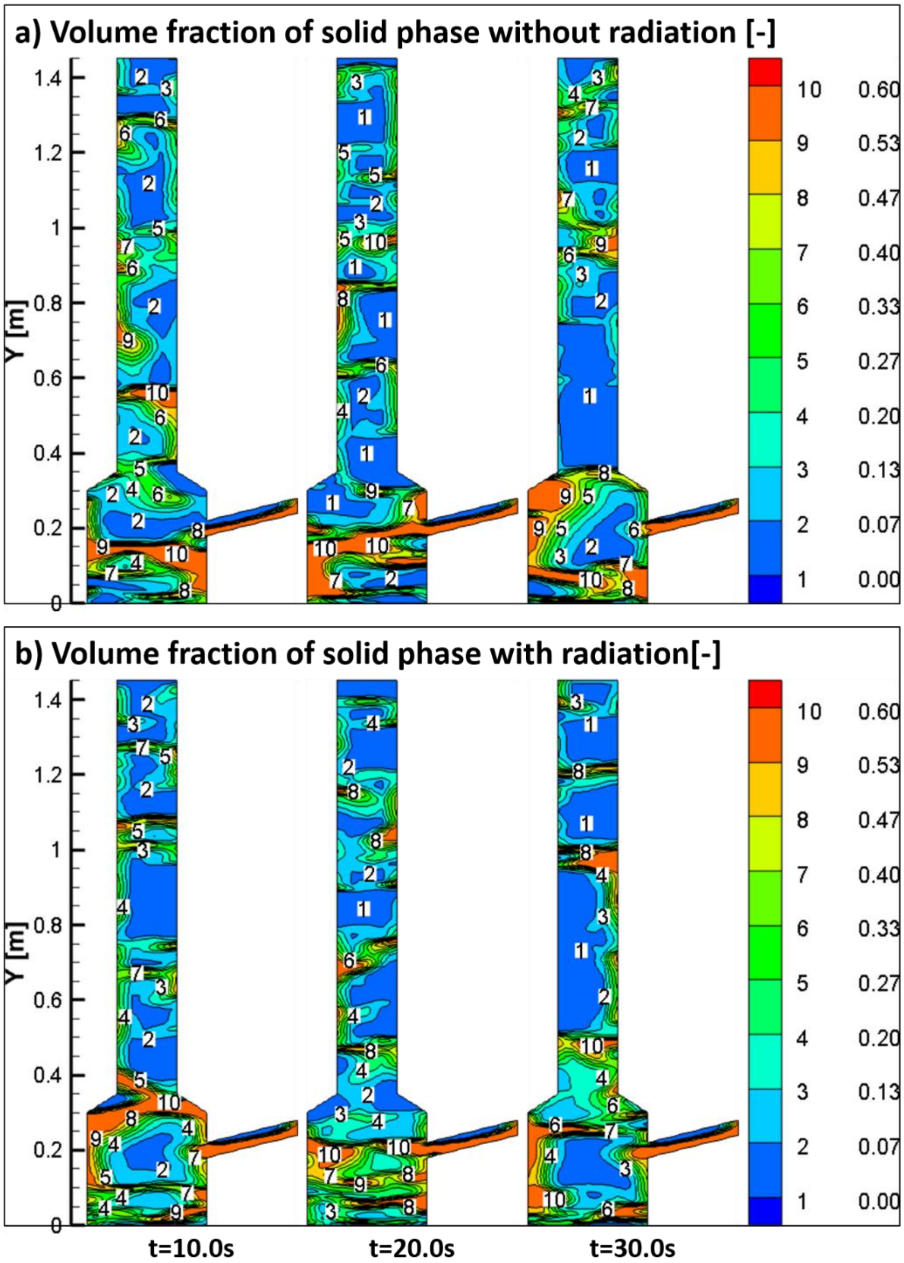

Figure 38 Contours of a) Volume fraction of solid phase without radiation, and b) Volume fraction of solid phase with radiation.

The volume fraction of solid particles without and with radiation are shown in Figure 38. Different from the FR which operates as bubbling bed, the AR operates as a fast bed from the top of which the solid particles are blown out with high-speed gas fed in from the bottom. The distribution of solid particles is very chaotic even from the very early time.

Unlike the FR, gas phase is the dominant phase within AR. Meanwhile, solid particles tend to attach to walls as they are risen by air. However, like FR, solid particles in the lower section of AR are denser comparing to solid particles in the upper section. But the difference in these two sections is not as significant as it is in FR. The difference of distributions of solid particles with radiation neglected and considered is very insignificant.

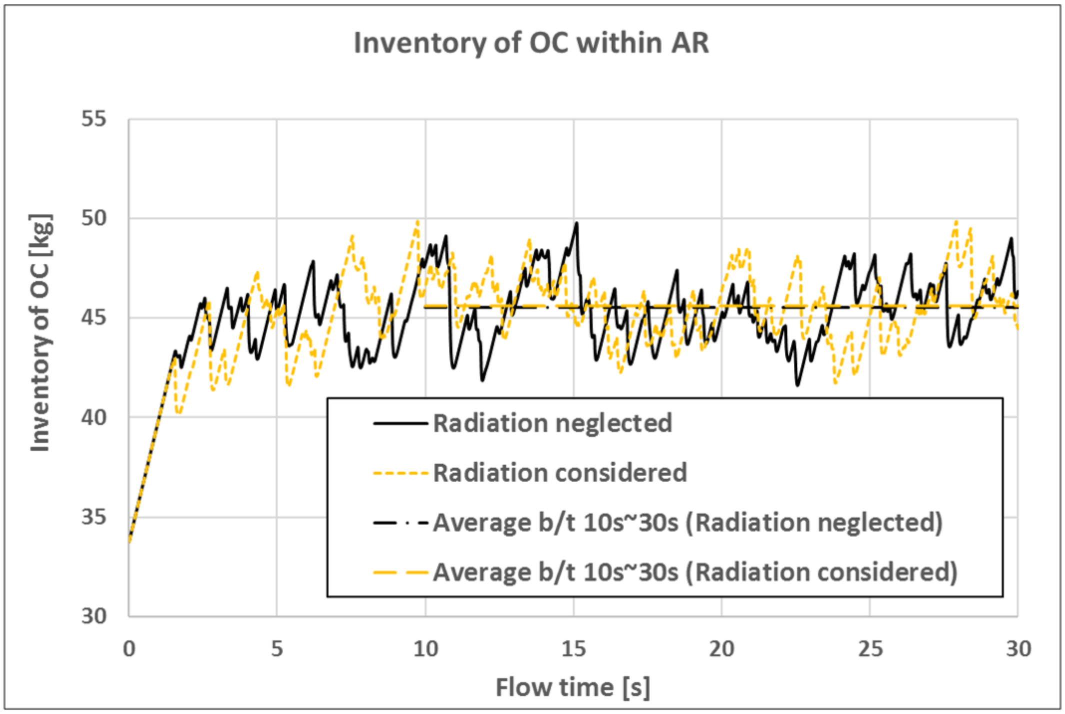

Figure 39 Plots of OC inventory within AR with radiation neglected and radiation considered.

The plot of OC inventory within AR indicates the total mass of OC (including Ni and NiO) in AR. OC particles accumulate from the initial value as reduced OC are transported into AR continuously from FR but no OC particles are blown out at the early stage of simulation. However, after about 3 seconds, inventory of OC fluctuates around a constant value, which can be estimated to be 45.5kg by averaging the inventory from 10s to 30s. Radiative heat transfer has very insignificant effects on OC inventory within AR.

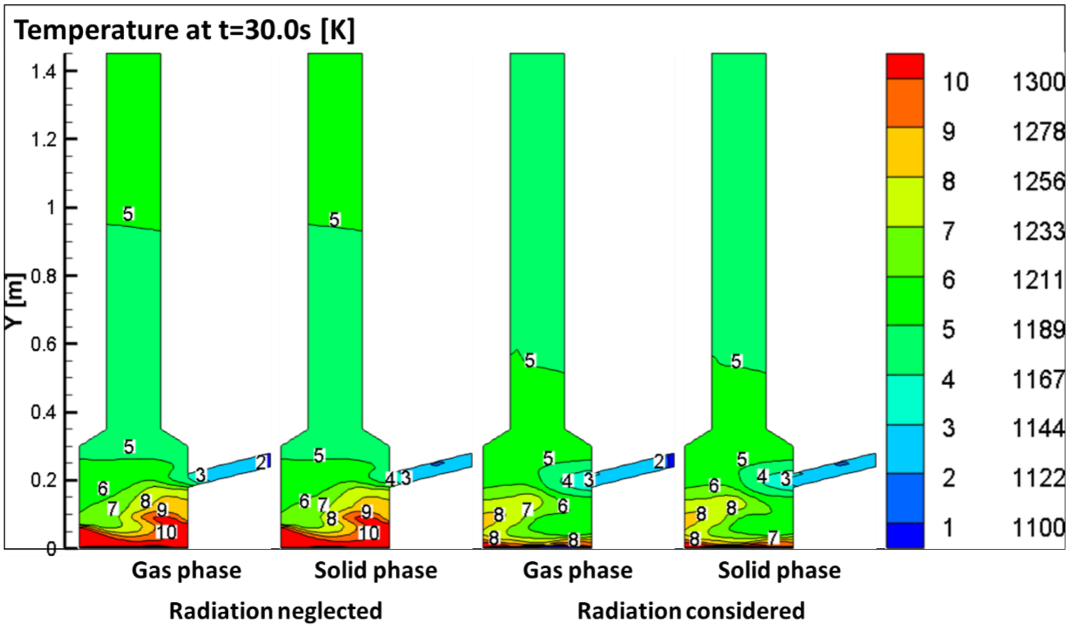

Figure 40 Contours of the temperature of gas and solid phases without and with radiation.

Contours of temperature indicate that temperature between gas phase and solid phase can be neglected. Meanwhile, temperature difference on the upper region of air reactor is very limited with or without radiation considered. However, the temperature on regions close to air inlet is lower when radiation is considered. The temperature on solid inlet regions is not affected by radiation significantly.

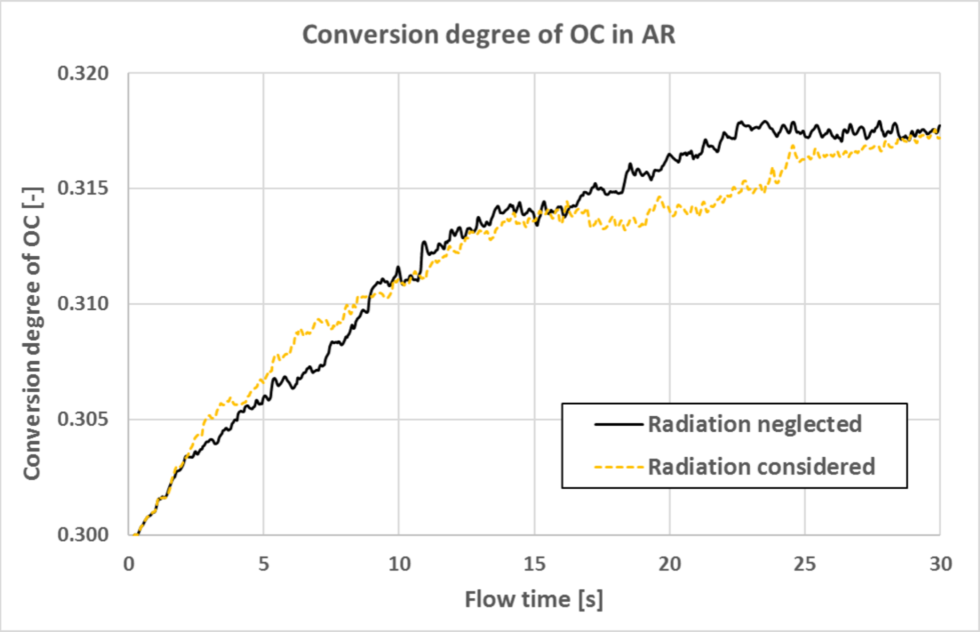

Figure 41 Conversion degree of OC within AR with radiation considered and radiation neglected.

The mass-weighted average conversion degree of Ni within AR is shown in Figure 41. Since the initial conversion degree of Ni within AR and mole fraction of NiO on OC inlet are taken as 30mole%, the total conversion degree of OC rises from 0.3 consistently to 0.318 as simulation continues, even though the inventory of OC fluctuates, as shown above. However, conversion degree reaches its peak of 0.138 at about 23s and maintains this value to the end of the simulation. Comparing to the inlet mass flow rate of OC (6.144kg/s), the amount of gas feeding from the bottom (0.071kg/s) is very small. Hence, only 1.8mole% of Ni is oxidized even though 100% of O_2 is reacted during this process. With proper design and better control on the mass flow rate of air and OC on the inlets, a sufficient Ni can be oxidized into NiO. With radiation considered, conversion degree difference of OC between 16s and 25s is obvious. However, radiative heat transfer has very insignificant effects on OC conversion degree after the steady stage.

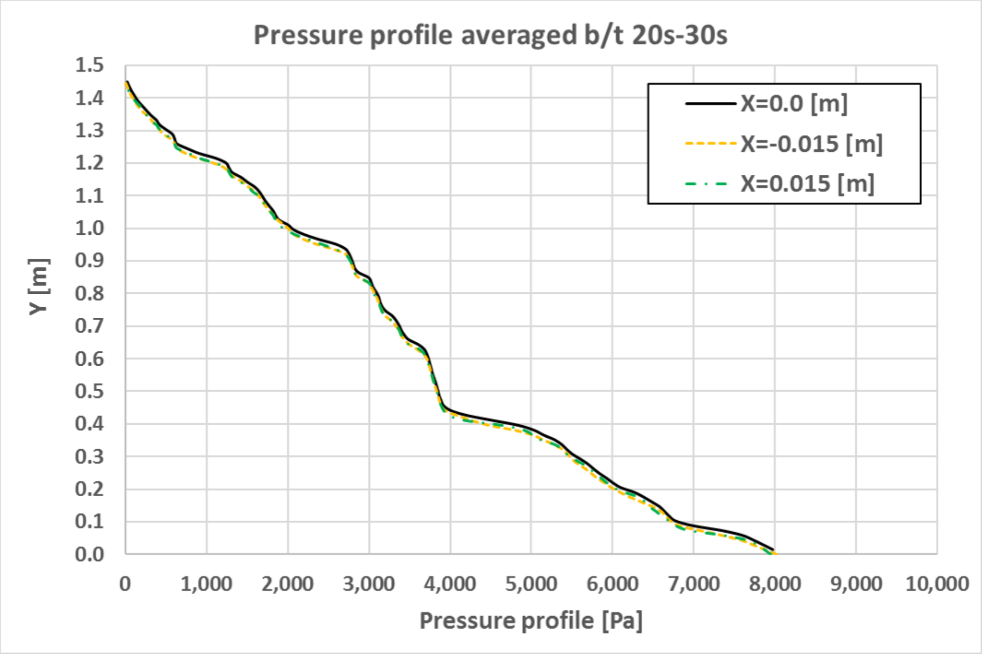

Figure 42 Pressure profiles along 3 vertical lines averaged b/t 20s-30s.

Pressure profiles along 3 vertical lines are plotted in Figure 42. Pressure profiles on vertical lines closer to walls are nearly identical to pressure profile along the center line. Pressure drops from 8000Pa at the bottom of AR to 5000Pa at Y=0.39m. This is the wider cylinder on the lower section of AR where contains relatively denser solid particles. Then the pressure drops significantly from 5000Pa to 4000Pa at the section between Y=0.39m and Y=0.43m where is above the contract section. Then the decline of pressure slows down at higher region of AR.

6.3 Effects of Initial Inventory

For the base case, the inventory (i.e. total mass) of OC particles is set to 33.8kg. As discussed above, inventory of OC vibrates around 45.5kg after 3s in the base case study.

The effects of initial OC inventory (I.I. of OC) on instant and averaged inventory are plotted in Figure 43.

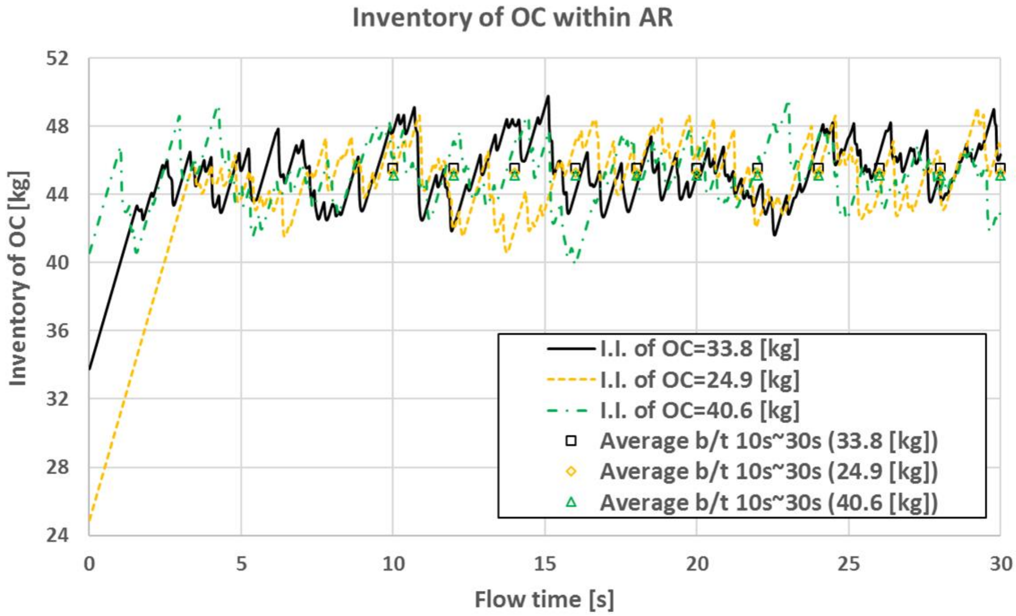

Figure 43 Plots of instant and averaged OC inventory with different OC initial inventory.

With higher initial OC inventory, AR has shorter OC accumulating process. With I.I. of OC equals to 24.9kg, instant inventory of OC has its first drop at 3.5s, while the first drop occurs at 2.0s and 1.0s with I.I. of OC equals to 33.8kg and 40.6kg, respectively. Meanwhile, the inventory oscillation magnitudes are enlarged at an early stage of simulation by higher I.I. of OC. However, the differences of oscillation magnitude of instant inventory with various I.I. of OC beyond 5s are insignificant. Besides, the averaged inventory b/t 10s and 30s are almost identical, 45.45kg, 45.26kg and 45.11kg for I.I. of OC equals to 33.8kg, 24.9kg, and 40.6kg, respectively.

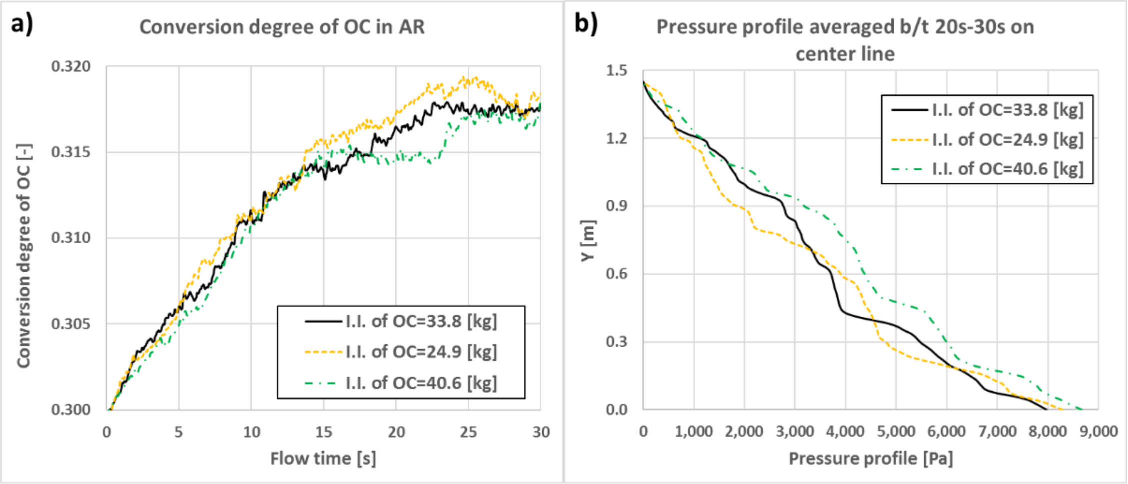

Figure 44 Plots of a) conversion degree of OC in AR, and b) averaged pressure profile on the center line with different I.I. of OC.

Conversion degree of Ni in AR and averaged pressure profile on the center line with different initial inventories of OC are plotted in Figure 44. Similar trend lines are fond in the plot of conversion degree of OC for 3 cases. The peak value of conversion degree, however, is slightly higher for smaller I.I. of OC. But all 3 lines stabilize at nearly the same value at the end of the simulation. Meanwhile, the impacts of OC initial inventory on pressure profile along the center line are not obvious.

Even though the effects of OC initial inventory on flow pattern and conversion performance are very limited, results still give important enlightenment. The inventory of OC within AR is stabilized by the system itself if the superficial feeding velocity is fixed.

6.4 Effects of Particle Size

As mentioned above, minimum fluidization velocity is a function of particle size. Flow pattern and conversion performance of Ni are tested in this section with different particle size and fixed superficial feeding velocity of air.

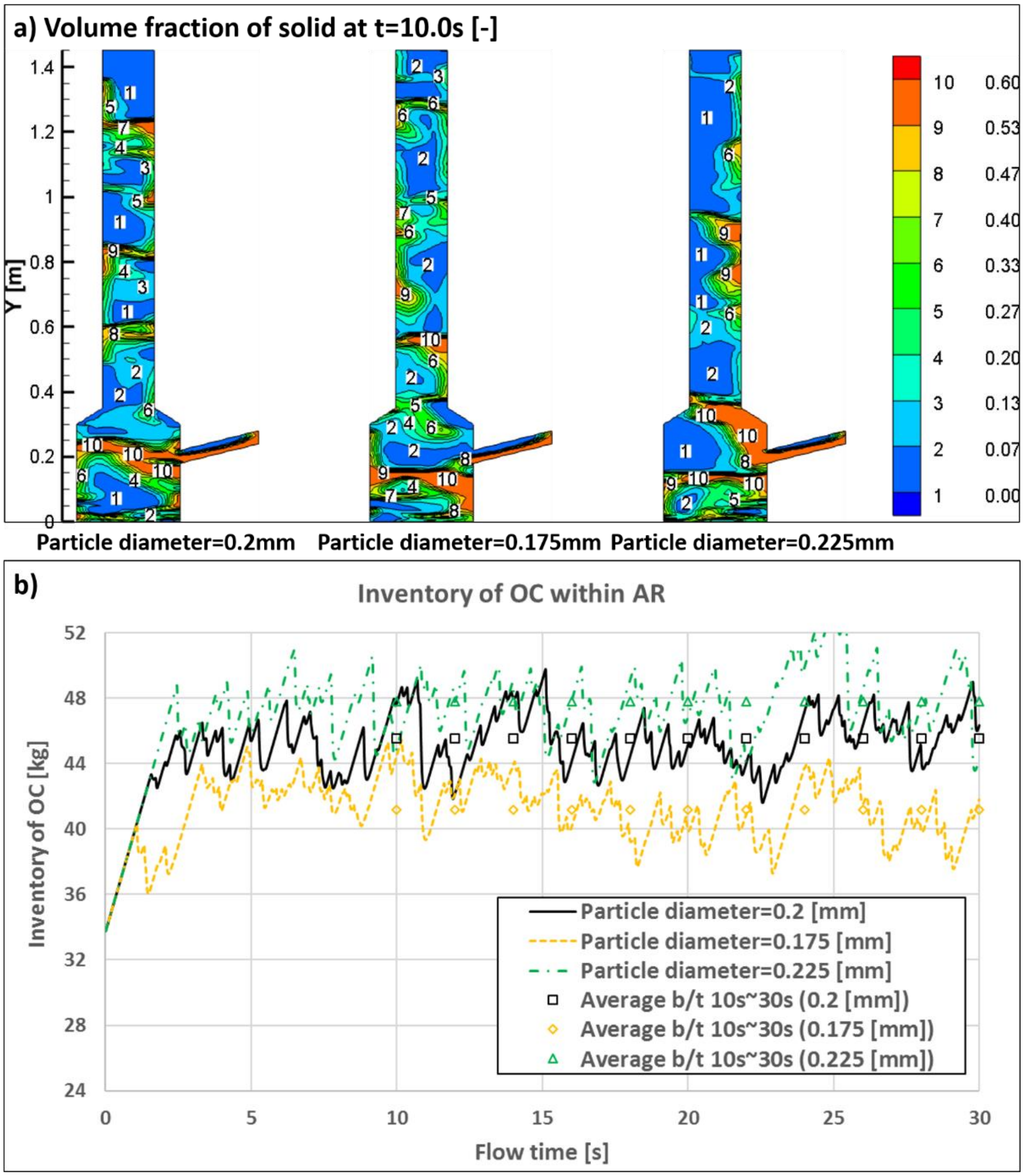

Figure 45 a) Contours of the volume fraction of solid phase at t=10.0s, and b) plot of inventory of OC within AR. Note that contours are scaled in Y direction for better exhibition.

Figure 45 depicts contours of the volume fraction of solid phase and inventory of OC with AR. Larger particle diameters result in larger MFV and hence smaller factors between SFV and MFV when SFV of air is fixed. Consequently, more solid particles accumulate in the lower section of AR since it is harder to blow solid particles out. However, the incensement of solid particles on the upper section is not obvious. The Same conclusions can be obtained by plotting the instant and averaged inventory of OC as a function of flow time. The averaged inventory of OC increases with particle diameter. The instant inventory with larger particle size, however, can be less than one with a smaller particle size within a short period.

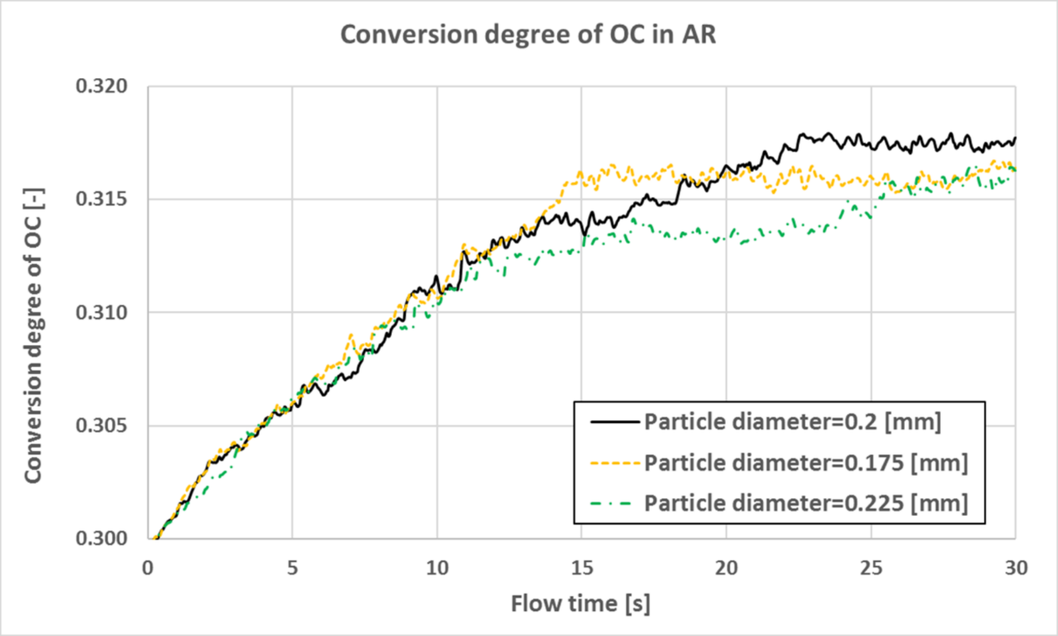

Figure 46 Conversion degree of OC in AR as a function of time with different particle diameters.

The conversion performances of AR with different particle diameters are also tested, as shown in Figure 46. From the beginning of simulation to 12s, the conversion degree of NiO with different particle diameters are almost identical. Conversion degree increases almost linearly with flow time. The conversion degree of NiO with a particle diameter of 0.175mm reaches its peak at 15s and maintains as nearly a constant of 0.317. The conversion degree of NiO with a diameter of 0.2mm reaches its peak at 23s, as discussed above. On the other hand, conversion degree of NiO with a diameter of 0.225mm does not gain its peak even at the end of the simulation. As discussed above, larger particle diameter results in larger accumulation of OC within AR, and hence longer period to gain the peak conversion degree.

6.5 Effects of Superficial Feeding Velocity of Air

As discussed above, the factors between SFV and MFV and be changed by modifying the diameter of solid particles and keeping the SFV fixed. It is also clear that these factors can also be modified by changing the SFV while keeping particle size fixed.

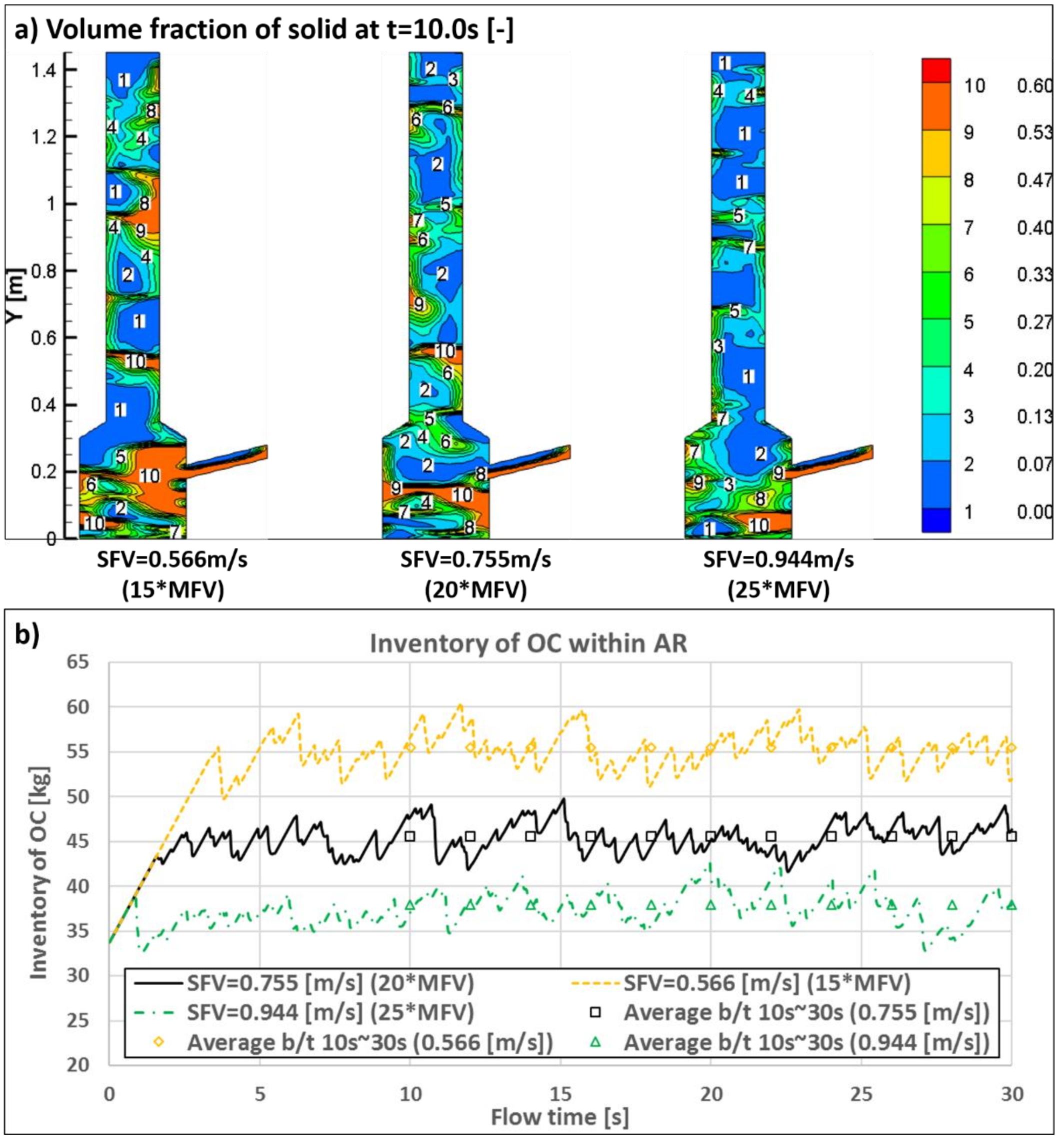

Figure 47 a) Contours of the volume fraction of solid phase at t=10.0s, and b) plots of inventory of OC within AR with different superficial feeding velocity.

Figure 47 illustrates the contours of the volume fraction of solid phase and plots of inventory of OC within AR with different SFV. With larger SFV of air on the bottom, the accumulation of solid particles decreases not only on the lower section but also the upper section of AR, and hence sparser distribution of OC particles. However, solid particles on the lower section remain higher density comparing to density on upper section for every case. Meanwhile, the accumulation period becomes shorter with larger SFV at an early stage of simulation. The accumulation periods are 3.6s, 2.0s, and 0.9s for the cases with SFV equal to 15*MFV, 20*MFV, and 25*MFV, respectively. After the accumulation period, inventory of OC fluctuates around a constant value throughout the entire simulation. These constants can be obtained by averaging the inventory within AR between 10s and 30s.

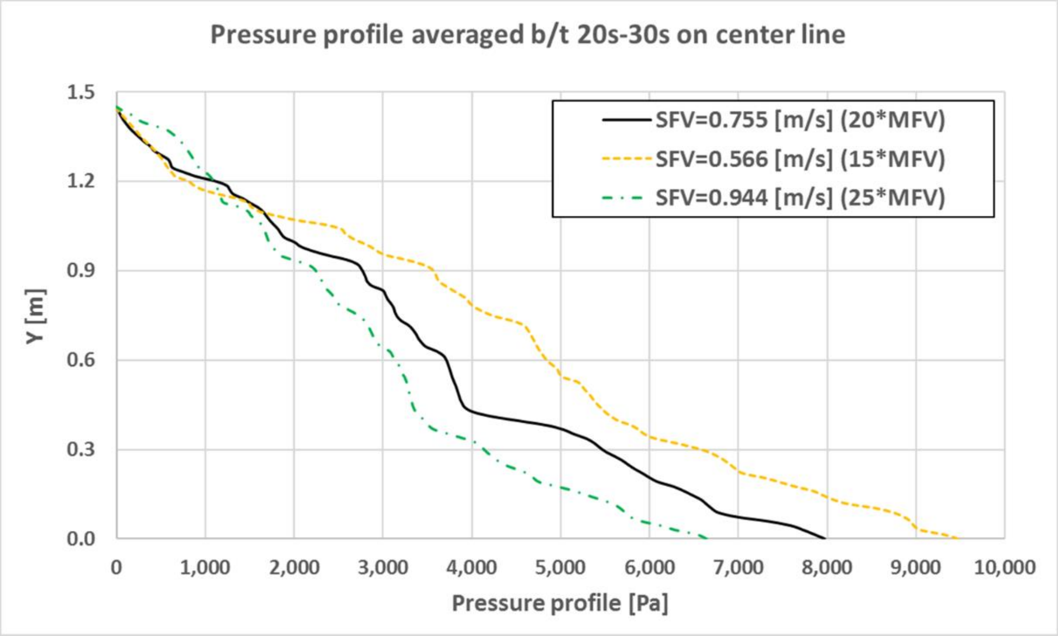

Figure 48 Plots of time-averaged pressure profile on the center line with different SFV.

Similar to the base case, the pressure drop on lower section are larger than pressure drop in the upper section for all cases. Depleted air exits AR at a pressure of 0Pa for all cases. However, pressures on the inlet of AR various widely. Due to a smaller amount of OC particles remain within AR when SFV becomes larger, the pressure on the inlet is correspondingly lower.

Table 15 Products of SFV and pressure on the inlet.

SFV of air [m/s]	Pressure on inlet [Pa]	Product [w/m^2]

0.755 (20*MFV)	7970.9	6018.0
0.566 (15*MFV)	9469.5	5359.7
0.944 (25*MFV)	6640.3	6268.4

Table 15 lists the different SFV of air, pressure on the inlet and their products, which are the feeding power (kinetic energy) needed to feed the air on the bottom. In practical applications, this energy needed to be produced by compressors. Even though higher SFV results in lower pressure on the inlet, the required feeding power is higher. However, the increase of feeding power from SFV equals 15*MFV to SFV equals 20*MFV is much larger than from 20*MFV to 25*MFV.

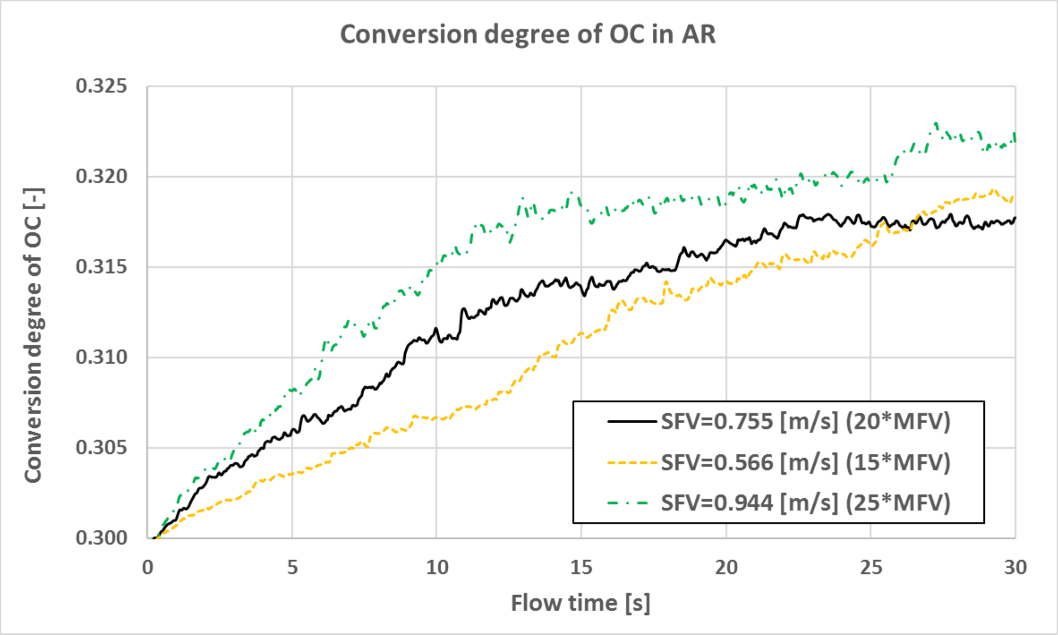

Figure 49 Conversion degree of OC within AR with different SFV.

Figure 49 plots the conversion degree of OC within AR in the case with different SFV of air. A small amount of OC remains within AR and more amount of air is fed when SFV is increased. Hence, conversion degree increases faster with larger SFV at an early stage.

6.6 Conclusions of AR Study

As an important part of CLC system, AR determines the circulating rate of OC particles and hence affects the functionality and performance of the entire system. Present study establishes the mathematical models for hydrodynamics, heat transfer and chemical reactions within AR. By conducting numerical simulations, effects of the initial inventory of OC, particle size and superficial feeding velocity are discussed. An initial inventory of OC has nearly no effects on conversion performance and limited effects on flow pattern at an early stage only. The particle size, however, has significant effects on flow pattern. When the flow rate of feeding air is fixed, a larger amount of solid particles accumulate with larger size particles, and hence earlier the conversion degree gets stabilized in a lower value. Besides particle size, superficial feeding velocity of air on inlet affects the flow pattern in a similar way as particle size does. Higher SFV reduces the accumulation of OC within AR. However, at the same time, higher SFV increases the flow rate of feeding air into AR and hence results in a faster increase and higher value of conversion degree of OC. The

CHAPTER 7

CONCLUSIONS AND RECOMMENDATIONS

7.1 Conclusions

Considered to be at its tipping point, global warming and climate change have been given massive attention by our society. As a promising technology for carbon capture, chemical looping combustion is an attractive mean to reduce carbon emission in many industrial fields like power plant, cement plant et al. By using an intermedium to transport elemental oxygen from air reactor to fuel reactor, CLC systems are expected to separate conventional combustion process into oxidation and reduction processes. Since the products exiting from FR are only CO_2 and water vapor, CO_2 can be gathered by condensing water vapor into liquid form, and hence high energy consuming gas separation processes can be avoided.

Main results achieved by the present work are the followings:

a) The mathematical modeling of both gas and solid phases are given by present work. Solid phase is modeled as a continuous medium, instead of discrete particles. However, two phases are linked by the volume fraction of each phase and momentum exchange model. To consider the effects collision between solid particles, the partial differential equation of granular temperature is solved. Moreover, the effects of the gradient of solid particles are solved by the partial differential equation of granular pressure. Besides the conductive-convective heat transfer, radiative heat transfer is also considered in present work. The radiative properties of solid particles are functions of its size and reflectivity. As a critical factor that determines the conversion performance of OC in both FR and AR, the kinetics of chemical reactions between two phases is usually modeled by unreacted shrinking core model.

b) Numerical results conducted on both FR and AR indicate that the coefficients between SFV of gas phase and MFV have essential effects on flow pattern within reactors. Meanwhile, MFV is a function of particle size, the density of both phases and the viscosity of gas phase. As a bubbling fluidized bed, the coefficient between SFV and MFV is usually around 3~7 in FR. The AR, as a fast-fluidized bed, usually operates at a coefficient greater than 10. The study of FR shows that SFV and particle size have significant effects on flow pattern. However, conversion performance is nearly not affected by particle size. Due to the low reactivity between H_2 and $CaSO_4$, higher SFV has very limited effects on conversion performance as well, even though more H_2 is fed into FR with higher SFV.

c) The usage of distributors on fuel inlet gives different types of velocity distribution on the inlet. The rectangle-triangle distributor results in better bubbles distributions, but the gain of higher fuel conversion rate is insignificant due to the low chemical activity of OC used in this study.

d) The effects of radiative heat transfer are also investigated by the present research. Numerical results indicate that radiative heat transfer has insignificant effects on flow pattern. On the other hand, radiative heat transfer has obvious effects on temperature distribution within free bed region where solid particles are sparse. However, within static bed region where solid particles are dense and hence heat capacity is high, the effects of radiative heat transfer on temperature distribution are very limited. Consequently, conversion performance is nearly not affected.

e) As an important component of CLC system, air reactor is also studied. With fixed SFV of air on the inlet, the flow rate of OC has slight effects on flow pattern and oxidation performance of OC. The test of the initial inventory of OC shows that AR can stabilize the total mass of OC within itself after the system gets stabilized. Particle size and SFV of air affect the coefficients between SFV and MFV and hence affects the flow pattern significantly.

f) Results presented in this work are helpful with CLC system design. As mentioned above, solid inventory is an important parameter for full conversion of fuel in FR. Numerical results in AR indicate that solid inventory within AR is mainly determined by SFV of air. Initial solid inventory is an insignificant factor of final inventory after the early stage. Numerical results within AR indicate that higher feeding power is needed with higher SFV, even though the pressure of air on inlet decreases with higher SFV. With the same mass feeding rate on the inlet of FR, gas distributors change bubble distributions to form more uniform distributions.

7.2 Recommendations

Though both fuel reactor and air reactor are studied in the present study, many research can be conducted as future work of this study.

a) Studies of a system connecting all components (including AR, FR, cyclone and loop seals) will be more comprehensive.

b) 3D simulations of CLC system will be more accurate even though enormous calculation power is required.

c) More studies of the effects of radiative heat transfer on AR are also required due to the sparser distribution of OC with AR.

d) Moreover, experimental works are needed to provide laboratory results.

References

[1] T. R. Anderson, E. Hawkins, and P. D. Jones, "CO2, the greenhouse effect and global warming: From the pioneering work of Arrhenius and Callendar to today's Earth System Models," *Endeavour*, vol. 40, no. 3, pp. 178–187, 2016.

[2] R. K. Pachauri, L. Meyer, J.-P. Van Ypersele, S. Brinkman, L. Van Kesteren, N. Leprince-Ringuet, and F. Van Boxmeer, *Climate Change 2014 Synthesis Report The Core Writing Team Core Writing Team Technical Support Unit for the Synthesis Report*. 2014.

[3] R. E. Zeebe, J. C. Zachos, K. Caldeira, and T. Tyrrell, "Carbon Emissions and Acidification," *Science (80-.).*, vol. 321, no. 2008, pp. 51–52, 2008.

[4] F. J. Millero, "Thermodynamics of the carbon dioxide system in the oceans," *Science (80-.).*, vol. 59, no. 4, pp. 661–677, 1995.

[5] Raven, John, K. Caldeira, H. Elderfield, O. Hoegh-Guldberg, P. Liss, U. Riebesell, J. Shepherd, C. Turley, and a. Watson, "Ocean acidification due to increasing atmospheric carbon dioxide," *R. Soc.*, no. June, pp. 1–68, 2005.

[6] R. a Feely, C. L. Sabine, K. Lee, W. Berelson, J. Kleypas, V. J. Fabry, F. J. Millero, and Anonymous, "Impact of anthropogenic CO (sub 2) on the CaCO (sub 3) system in the oceans," *Science (80-.).*, vol. 305, no. 5682, pp. 362–366, 2004.

[7] R. F. Service, "Rising Acidity Brings an Ocean of Trouble," *Science (80-.).*, vol. 337, no. 6091, pp. 146–148, 2012.

[8] G. Heutel, J. Moreno-Cruz, and S. Shayegh, “Climate tipping points and solar geoengineering,” *J. Econ. Behav. Organ.*, vol. 132, pp. 19–45, 2015.

[9] W. G. I. of the I. P. on C. Change, *IPCC,2005: Special Report on CARBON DIOXIDE CAPTURE AND STORAGE*. 2005.

[10] H. Fang, L. Haibin, and Z. Zengli, “Advancements in development of chemical-looping combustion: A review,” *Int. J. Chem. Eng.*, vol. 2009, no. ii, 2009.

[11] H. J. RICHTER and K. F. KNOCHE, “Reversibility of combustion processes,” *ACS Symp. Ser.*, no. 235, pp. 71–85, 1983.

[12] M. M. Hossain and H. I. de Lasa, “Chemical-looping combustion (CLC) for inherent CO2 separations-a review,” *Chem. Eng. Sci.*, vol. 63, no. 18, pp. 4433–4451, 2008.

[13] A. Adánez, J., García-Labiano, F., de Diego, L.F., Plata, A., Celaya, J., Gayán, P., Abad, “Optimizing the fuel reactor for chemical-looping combustion,” in *Proceedings of the 17th International Conference on Fluidized Bed Combustion*, 2003, pp. 173–182.

[14] J. Jung and I. K. Gamwo, “Multiphase CFD-based models for chemical looping combustion process: Fuel reactor modeling,” *Powder Technol.*, vol. 183, no. 3, pp. 401–409, 2008.

[15] B. Kim and H. Sohn, “cyclic reaction system involving CaS and CaSO4 for converting sulfur dioxide to elemental sulfur without generating secondary pollutants. 3. Kinetics of the hydrogen,” *Ind. Eng. Chem. Res.*, pp. 3092–3096,

2002.

[16] Z. Deng, R. Xiao, B. Jin, and Q. Song, “Numerical simulation of chemical looping combustion process with CaSO4 oxygen carrier,” *Int. J. Greenh. Gas Control*, vol. 3, no. 4, pp. 368–375, 2009.

[17] A. B. Harichandan and T. Shamim, “CFD analysis of bubble hydrodynamics in a fuel reactor for a hydrogen-fueled chemical looping combustion system,” *Energy Convers. Manag.*, vol. 86, pp. 1010–1022, 2014.

[18] H. Kruggel-Emden, S. Rickelt, F. Stepanek, and a. Munjiza, “Development and testing of an interconnected multiphase CFD-model for chemical looping combustion,” *Chem. Eng. Sci.*, vol. 65, no. 16, pp. 4732–4745, 2010.

[19] N. Zhang, B. Lu, W. Wang, and J. Li, “Virtual experimentation through 3D full-loop simulation of a circulating fluidized bed,” *Particuology*, vol. 6, no. 6, pp. 529–539, 2008.

[20] S. Wang, H. Lu, F. Zhao, and G. Liu, “CFD studies of dual circulating fluidized bed reactors for chemical looping combustion processes,” *Chem. Eng. J.*, vol. 236, pp. 121–130, 2014.

[21] Z. Peng, E. Doroodchi, Y. a. Alghamdi, K. Shah, C. Luo, and B. Moghtaderi, “CFD-DEM simulation of solid circulation rate in the cold flow model of chemical looping systems,” *Chem. Eng. Res. Des.*, vol. 95, pp. 262–280, 2015.

[22] J. M. Parker, “CFD model for the simulation of chemical looping combustion,” *Powder Technol.*, vol. 265, pp. 47–53, 2014.

[23] N. Yang, W. Wang, W. Ge, and J. Li, “CFD simulation of concurrent-up gas-solid flow in circulating fluidized beds with structure-dependent drag coefficient,” *Chem. Eng. J.*, vol. 96, no. 1–3, pp. 71–80, 2003.

[24] Y. Guan, J. Chang, K. Zhang, B. Wang, and Q. Sun, “Three-dimensional CFD simulation of hydrodynamics in an interconnected fluidized bed for chemical looping combustion,” *Powder Technol.*, vol. 268, pp. 316–328, 2014.

[25] M. Syamlal and T. J. O’Brien, “Simulation of granular layer inversion in liquid fluidized beds,” *Int. J. Multiph. Flow*, vol. 14, no. 4, pp. 473–481, 1988.

[26] J. Ding and D. Gidaspow, “A bubbling fluidization model using kinetic theory of granular flow,” *AIChE J.*, vol. 36, no. 4, pp. 523–538, 1990.

[27] T. Mendiara, L. F. de Diego, F. García-Labiano, P. Gayán, a. Abad, and J. Adánez, “Behaviour of a bauxite waste material as oxygen carrier in a 500Wth CLC unit with coal,” *Int. J. Greenh. Gas Control*, vol. 17, pp. 170–182, 2013.

[28] C. Linderholm and M. Schmitz, “Chemical-looping combustion of solid fuels in a 100 kW dual circulating fluidized bed system using iron ore as oxygen carrier,” *J. Environ. Chem. Eng.*, vol. 4, no. 1, pp. 1029–1039, 2016.

[29] S. Rajendran, M. Wong, D. Stokie, and S. Bhattacharya, “Performance of a Victorian brown coal and iron ore during chemical looping combustion in a 10 kWth alternating fluidized bed,” *Fuel*, vol. 183, pp. 245–252, 2016.

[30] J. Yang, L. Ma, J. Tang, H. Liu, B. Zhu, Y. Lian, and X. Cui, “Chemical thermodynamics analysis for in-situ gasification chemical looping combustion of

lignite with phosphogypsum for syngas," *Appl. Therm. Eng.*, vol. 112, pp. 516–522, 2017.

[31] G. Huijun, S. Laihong, F. Fei, and J. Shouxi, "Experiments on biomass gasification using chemical looping with nickel-based oxygen carrier in a 25 kWth reactor," *Appl. Therm. Eng.*, vol. 85, pp. 52–60, 2015.

[32] M. H. Bordbar, K. Myöhänen, and T. Hyppänen, "Coupling of a radiative heat transfer model and a three-dimensional combustion model for a circulating fluidized bed furnace," *Appl. Therm. Eng.*, vol. 76, pp. 344–356, 2015.

[33] R. I. Singh, A. Brink, and M. Hupa, "CFD modeling to study fluidized bed combustion and gasification," *Appl. Therm. Eng.*, vol. 52, no. 2, pp. 585–614, 2013.

[34] Y. Nakano, S. Iwamoto, T. Maeda, M. Ishida, and T. Akehata, "Characteristics of Reduction and Oxidation Cyclic Process by Use of alpha Fe2O3 Medium," *Tetsu-to-Hagane(J. Iron Steel Inst. Jpn.)*, vol. 72, no. 10, pp. 1521–1528, 1986.

[35] K. S. Go, S. R. Son, and S. D. Kim, "Reaction kinetics of reduction and oxidation of metal oxides for hydrogen production," *Int. J. Hydrogen Energy*, vol. 33, no. 21, pp. 5986–5995, 2008.

[36] K. S. Go, S. R. Son, S. D. Kim, K. S. Kang, and C. S. Park, "Hydrogen production from two-step steam methane reforming in a fluidized bed reactor," *Int. J. Hydrogen Energy*, vol. 34, no. 3, pp. 1301–1309, 2009.

[37] K. S. Kang, C. H. Kim, K. K. Bae, W. C. Cho, S. U. Jeong, Y. J. Lee, and C. S.

Park, “Reduction and oxidation properties of Fe_2O_3/ZrO_2 oxygen carrier for hydrogen production,” *Chem. Eng. Res. Des.*, vol. 92, no. 11, pp. 2584–2597, 2014.

[38] M. Ishida and Hongguang Jin, “A novel combustor based on chemical-looping reactions and its reaction kinetics,” *Journal of Chemical Engineering of Japan*, vol. 27, no. 3. pp. 296–301, 1994.

[39] P. Erri and A. Varma, “Diffusional effects in nickel oxide reduction kinetics,” *Ind. Eng. Chem. Res.*, vol. 48, no. 1, pp. 4–6, 2008.

[40] Z. Zhou, L. Han, and G. M. Bollas, “Kinetics of NiO reduction by H_2 and Ni oxidation at conditions relevant to chemical-looping combustion and reforming,” *Int. J. Hydrogen Energy*, vol. 39, no. 16, pp. 8535–8556, 2014.

[41] B. Jiang, B. Dou, Y. Song, C. Zhang, B. Du, H. Chen, C. Wang, and Y. Xu, “Hydrogen production from chemical looping steam reforming of glycerol by Ni-based oxygen carrier in a fixed-bed reactor,” *Chem. Eng. J.*, vol. 280, pp. 459–467, 2015.

[42] S. Roux, A. Bensakhria, and G. Antonini, “Study and improvement of the regeneration of metallic oxides used as oxygen carriers for a new combustion process,” *Int. J. Chem. React. Eng.*, vol. 4, no. February, pp. 1–14, 2006.

[43] Q. Zafar, T. Mattisson, and B. Gevert, “Redox investigation of some oxides of transition-state metals Ni, Cu, Fe, and supported on SiO_2 and $MgAl_2O_4$,” *Energy and Fuels*, vol. 20, no. 1, pp. 34–44, 2006.

[44] A. Rubel, K. Liu, J. Neathery, and D. Taulbee, “Oxygen carriers for chemical looping combustion of solid fuels,” *Fuel*, vol. 88, no. 5, pp. 876–884, 2009.

[45] L. F. De Diego, F. García-Labiano, J. Adánez, P. Gayán, A. Abad, B. M. Corbella, and J. M. Palacios, “Development of Cu-based oxygen carriers for chemical-looping combustion,” *Fuel*, vol. 83, no. 13, pp. 1749–1757, 2004.

[46] H. Tian, K. Chaudhari, T. Simonyi, J. Poston, T. Liu, T. Sanders, G. Veser, and R. Siriwardane, “Chemical-looping combustion of coal-derived synthesis gas over copper oxide oxygen carriers,” *Energy & Fuels*, vol. 22, no. 6, pp. 3744–3755, 2008.

[47] R. Siriwardane, H. Tian, G. Richards, T. Simonyi, and J. Poston, “Chemical-Looping Combustion of Coal with Metal Oxide Oxygen Carriers,” *Energy Fuels*, vol. 23, no. 8, pp. 3885–3892, 2009.

[48] T. Mattisson, A. Järdnäs, and A. Lyngfelt, “Reactivity of some metal oxides supported on alumina with alternating methane and oxygen - Application for chemical-looping combustion,” *Energy and Fuels*, vol. 17, no. 3, pp. 643–651, 2003.

[49] J. Adanez, F. García-Labiano, L. F. de Diego, P. Gayán, J. Celaya, and A. Abad, “Characterization of oxygen carriers for chemical-looping combustion,” *Greenh. Gas Control Technol.*, pp. 105–113, 2005.

[50] X. Niu, L. Shen, S. Jiang, H. Gu, and J. Xiao, “Combustion performance of sewage sludge in chemical looping combustion with bimetallic Cu-Fe oxygen

carrier," *Chem. Eng. J.*, vol. 294, pp. 185–192, 2016.

[51] S. Zhang, R. Xiao, J. Liu, and S. Bhattacharya, "Performance of Fe2O3/CaSO4 composite oxygen carrier on inhibition of sulfur release in calcium-based chemical looping combustion," *Int. J. Greenh. Gas Control*, vol. 17, pp. 1–12, 2013.

[52] Y. Larring, M. Pishahang, M. F. Sunding, and K. Tsakalakis, "Fe-Mn based minerals with remarkable redox characteristics for chemical looping combustion," *Fuel*, vol. 159, pp. 169–178, 2015.

[53] V. Frick, M. Rydén, and H. Leion, "Investigation of Cu-Fe and Mn-Ni oxides as oxygen carriers for chemical-looping combustion," *Fuel Process. Technol.*, vol. 150, pp. 30–40, 2015.

[54] P. Perreault, S. Rifflart, E. Nguyen, and G.-S. Patience, "Pyrolusite: An alternative oxygen carrier for chemical looping combustion," *Fuel*, vol. 185, pp. 630–638, 2016.

[55] M. Su, J. Ma, X. Tian, and H. Zhao, "Reduction kinetics of hematite as oxygen carrier in chemical looping combustion," *Fuel Process. Technol.*, 2016.

[56] M. M. Hossain and H. I. de Lasa, "Reduction and oxidation kinetics of Co-Ni/Al2O3 oxygen carrier involved in a chemical-looping combustion cycles," *Chem. Eng. Sci.*, vol. 65, no. 1, pp. 98–106, 2010.

[57] Q. Zafar, A. Abad, T. Mattisson, B. Gevert, and M. Strand, "Reduction and oxidation kinetics of Mn3O4/Mg-ZrO2 oxygen carrier particles for chemical-looping combustion," *Chem. Eng. Sci.*, vol. 62, no. 23, pp. 6556–6567, 2007.

[58] Q. Zafar, A. Abad, T. Mattisson, and B. Gevert, “Reaction kinetics of freeze-granulated NiO/MgAl2O4 oxygen carrier particles for chemical-looping combustion,” *Energy & Fuels*, vol. 21, no. x, pp. 610–618, 2007.

[59] M. A. L. de Bertodano, “Turbulent bubbly two-phase flow in a triangular duct,” 1992.

[60] M. Syamlal and T. J. O’Brien, “Computer simulation of bubbles in a fluidized bed,” in *AIChE Symp. Ser*, 1989, vol. 85, no. 1, pp. 22–31.

[61] C. Wen and Y. H. Yu, “Mechanics of fluidization,” in *Chem. Eng. Prog. Symp. Ser.*, 2014, vol. 62, no. 62, p. 100.

[62] D. Gidaspow, R. Bezburuah, and J. Ding, “Hydrodynamics of circulating fluidized beds: kinetic theory approach,” 1991.

[63] D. J. Gunn, “Transfer of heat or mass to particles in fixed and fluidised beds,” *Int. J. Heat Mass Transf.*, vol. 21, no. 4, pp. 467–476, 1978.

[64] M. Kaviany, *Principles of Heat Transfer in Porous Media*. Springer New York, 1991.

[65] R. Siegel and J. R. Howell, *Thermal radiation heat transfer*. Hemisphere Pub. Corp., 1981.

[66] H. C. Hottel and A. F. Sarofim, *Radiative Transfer*. McGraw-Hill, 1967.

[67] T. F. Smith, Z. F. Shen, and J. N. Friedman, “Evaluation of Coefficients for the Weighted Sum of Gray Gases Model,” *J. Heat Transfer*, vol. 104, no. 4, pp. 602–

608, Nov. 1982.

[68] A. Coppalle and P. Vervisch, “The total emissivities of high-temperature flames,” *Combust. Flame*, vol. 49, no. 1–3, pp. 101–108, 1983.

[69] M. K. Denison and B. W. Webb, “A Spectral Line-Based Weighted-Sum-of-Gray-Gases Model for Arbitrary RTE Solvers,” *J. Heat Transfer*, vol. 115, no. 4, pp. 1004–1012, Nov. 1993.

[70] D. K. Edwards and R. Matavosian, “Scaling Rules for Total Absorptivity and Emissivity of Gases,” *J. Heat Transfer*, vol. 106, no. 4, pp. 684–689, Nov. 1984.

[71] D. J. Patil, M. van Sint Annaland, and J. A. M. Kuipers, “Critical comparison of hydrodynamic models for gas--solid fluidized beds—Part I: bubbling gas--solid fluidized beds operated with a jet,” *Chem. Eng. Sci.*, vol. 60, no. 1, pp. 57–72, 2005.

[72] C. K. K. Lun, S. B. Savage, D. J. Jeffrey, and N. Chepurniy, “Kinetic theories for granular flow: inelastic particles in Couette flow and slightly inelastic particles in a general flowfield,” *J. Fluid Mech.*, vol. 140, pp. 223–256, 1984.

[73] S. Ogawa, A. Umemura, and N. Oshima, “On the equations of fully fluidized granular materials,” *Zeitschrift f{ü}r Angew. Math. und Phys. ZAMP*, vol. 31, no. 4, pp. 483–493, 1980.

[74] D. G. Schaeffer, “Instability in the evolution equations describing incompressible granular flow,” *J. Differ. Equ.*, vol. 66, no. 1, pp. 19–50, 1987.

[75] K. E. Sedor, M. M. Hossain, and H. I. De Lasa, “Reduction kinetics of a

fluidizable nickel-alumina oxygen carrier for chemical-looping combustion," *Can. J. Chem. Eng.*, vol. 86, no. 3, pp. 323–334, 2008.

[76] S. K. Gupta, V. K. Agarwal, S. N. Singh, V. Seshadri, D. Mills, J. Singh, and C. Prakash, "Prediction of minimum fluidization velocity for fine tailings materials," *Powder Technol.*, vol. 196, pp. 263–271, 2009.

[77] C. Y. W. R. R. Pattipati, "Minimum Fluidization Velocity at High Temperatures," *Ind. Eng. Chem. Process Des. Dev.*, vol. 20, pp. 705–707, 1981.

[78] Z. Zhao, C. O. Iloeje, T. Chen, and A. F. Ghoniem, "Design of a rotary reactor for chemical-looping combustion. Part 1: Fundamentals and design methodology," *Fuel*, vol. 121, pp. 327–343, 2014.

[79] Z. Zhao and A. F. Ghoniem, "Design of a rotary reactor for chemical-looping combustion. Part 2: Comparison of copper-, nickel-, and iron-based oxygen carriers," *Fuel*, vol. 121, pp. 344–360, 2014.

Vitae

Name : Haixia Li

Nationality : Chinese

Date of Birth : 9/20/1991

Email : leehaixia@outlook.com

Address : No. 69, Houliao Village, Xinliao Town, Xuwen County,
Guangdong Province, China

Academic Background : Bachelor: School of Energy and Power Engineering,
Huazhong University of Science & Technology

Master of Science: Mechanical Engineering Department,
King Fahd University of Petroleum & Minerals